VECTOR CORRELATIONS AND THEIR APPLICATIONS IN PHOTODISSOCIATION DYNAMICS STUDY

A Dissertation

by

WEI WEI

Submitted to the Office of Graduate and Professional Studies of
Texas A&M University
in partial fulfillment of the requirements for the degree of

DOCTOR OF PHILOSOPHY

Chair of Committee,	Simon W. North
Committee Members,	Timothy R. Hughbanks
	Christian B. Hilty
	Alexei V. Sokolov
Head of Department,	Simon W. North

December 2017

Major Subject: Chemistry

ABSTRACT

The velocity map ion imaging technique is a powerful tool for studying photodissociation. Determination of correlated product internal and translational energy distribution, as well as vector correlations, can elucidate fundamental dynamics of the photo-induced reactions. Vector correlations, which describe the relative orientations of the transition dipole moment of the parent molecule **μ**, recoil velocity vector **v**, and angular momentum vector of photofragment rotation ***j*** are sensitive probes of the stereodynamics of photodissociation reactions. The focus of this dissertation is the development and application of a method for extracting vector correlation, from experimental angular distribution of sliced or reconstructed non-sliced images generated by 2+1 REMPI. Two general approaches for applying the new equations; direct inversion and forward convolution, are presented. The new method is tested with images of OCS photodissociation at 230 nm and NO_2 photodissociation at 355 nm and the results are compared to previous publications.

The ultraviolet photodissociation of carbonyl sulfide (OCS) is an important system, not only because of its role in atmospheric chemistry, but also because of its significance as a benchmark system of photodissociation via multi-excited states. We are particularly interested in the wavelength dependence of the dynamics. The OCS photodissociation dynamics of the dominant $S(^1D_2)$ channel near 214 nm have been studied, as an application of our new method mentioned above. We report a vibrational branching ratio of 0.79/0.21 for CO v=0/v=1, indicating substantially higher vibrational excitation than that observed at longer wavelengths. The CO rotational distribution is bimodal for both v=0 and v=1, although the bimodality is less pronounced than at longer

wavelengths. The measurements of vector correlations indicate that excitations to both the $2^1A'$ (A) and $1^1A''$ (B) states are important in the lower-*j* part of the rotational distribution, while only $2^1A'$ state contributes to the upper part. The discovery is consistent with the previous work at longer wavelengths. The computational chemistry results from Dr. George McBane support the experimental results, and also suggest that the highest-j peak arises from molecules that begin on the $2^1A'$ state but make non-adiabatic transitions to the $1^1A'$ (X) state during the dissociation.

DEDICATION

This work is dedicated to my parents Junying Wei and Hua Wu, and my advisor, Dr. Simon W. North

ACKNOWLEDGEMENTS

“Why do you like to study photodissociation dynamics?”

This is a common question asked by my parents and friends who have majored in biology, engineering, social sciences, humanity, and sometimes even chemistry. Depending on the audience, I may answer “photodissociation dynamics helps us improve our current model for atmospheric/environmental science” or “it can help us understand combustion processes better”. But, perhaps, what I really need to try explaining to them is that I enjoy the process of solving the myth and prefer a world that is understandable with a theory of everything.

Two hundred years ago, science was still a rich men’s hobby, which was funded by researchers themselves. Now science is funded by the states and expected to yield great applications for society. Scientists are commonly asked questions regarding the “vision” or possible applications of their research. In reality, scientific research is “self-motivated” and the goal is to understand the world around us. Such motivation for understanding the nature of the world can even be traced back to pre-science era Greek philosophers like Thales of Miletus.

There are many people I would like to thank. First, I would like to thank my parents. I was born in the historical period of great unrest and social transition in China. Out of so many possible living paths, you gave me my life, gave me decent living quality, high quality education, and most importantly, rich emotional support. Your emotional supports make me feel safe, creative and give me hope. You helped me keep moving forward on my research and growth over the past six years. Father, thank you for your

hard work for the family. Thank you for sharing your lifetime philosophy with me. Mother, thank you for your support of the family. I could not imagine our family without you. You also played a critical educator role in my young age. There are so many other things I would like to thank you both for, all of which I cannot list here.

Dr. North, I really appreciate your advising. In ancient Chinese culture, teacher/advisor has a special meaning: they teach knowledge and philosophy; they also demonstrate by words and by behaviors to the young scholars what qualities a good scholar should have. You are definitely a great advisor both in American culture and in Chinese culture. You demonstrated a number of standards for my future life, through our talks in the laboratory, in group meeting and in coffee places. Your enthusiasm for both science and teaching gave me great impressions. Thank you for the precious opportunity of assembling the Gen III VMI apparatus. You impressed on me of the importance of experiments in fundamental chemistry, which has had a prolonged influence in my research philosophy. You also changed my idealistic expectation for some of my projects. Without your guidance, I would have never felt satisfied about my 2+1 Equations and published them. In the future I will also try to learn your working efficiency.

Michael, thank you for being a role model as a young scientist. Thank you for sharing all your knowledge with me. I could not have derived the 2+1 Equations in this work without your help starting from scratch. I wish we could have spent more time working together. But I am so glad to see students in Fort Lewis College having Professor Grubb.

Michelle, congratulations on your new position. Thank you for mentoring your naïve junior student Wei. I enjoyed all our discussions in lab, about science and about non-science topics. I wish I could have worked with you better at the beginning.

Colin and Carolyn, I really enjoy working with you in the group. Now I hand the great Gen III VMI apparatus to both of you. Both of you are brilliant and hard working. I am confident that you will start a new era for the dynamics project of the North group. Special thanks to Colin for working with me and helping me through most of my experimental period. And thank you Carolyn for helping me proofread this work.

I would also like to thank everyone else in the North group. It is my great pleasure working with you all. I enjoy the five years of graduate school with Nic as a great lab mate, and enjoyed our exciting trip to Georgia Tech, together with Wade. Rodrigo, your one-long-day help on the Scanmate laser saved the rest of my graduate school life. I enjoyed all the fun talk about scientific and non-scientific topics with Josh, Wilmarie, Feng (General) and Zach.

I would like to thank my committee members, Dr. Hughbanks, Dr. Hilty and Dr. Sokolov. I have received a rich amount of suggestions and guidance from them. I am very lucky to have taken Dr. Hughbanks' group theory course. I have spent a great time working under Dr. Hilty's supervision as a teaching assistant for physical chemistry laboratory. Dr. Sokolov provided me a lot of suggestions from the view of a physicist, which is quite unique and valuable for me. I would like to thank all of them for their guidance in the past years in Texas A&M University. I would also like to thank Dr. Lucchese for useful insight about angular distribution and spherical harmonics.

I would like to thank the whole academic community of reaction dynamics. I believe the community has preserved the classical image of scientists who try to

understand nature, collaborate with each other and share details with each other without reservations. I would like to thank Dr. McBane for helping us interpret the OCS dynamics with his computational work. I would also like to thank Dr. Hall for a rich amount of inspiring discussions regarding vector correlations. It was also my great pleasure to visit your lab in BNL. I would like to thank Dr. Kable and Dr. Quinn for sharing all the useful experimental details about acetaldehyde. I remember one of your emails had a full four pages of content, single spaced. I acknowledge Dr. Yuxiang Mo and Dr. Toshinori Suzuki for providing experimental data as well as helpful insights. I would also like to thank Dr. Rakitzis, Dr. Bartz and Dr. Cline for helpful discussions about vector correlation extraction methods. The parts we used to assemble the Gen III VMI apparatus were provided by Dr. Houston. Thank you so much for the help.

During the six years in Texas A&M University, I received numerous kinds of help from the university and from the Department of Chemistry. Will, you are magical. I really appreciate your nice work. Thank you for teaching me all about machining. I own you 20 bucks and a bingo. Tim, thank you for helping us with all of the issues with our electronic equipment. Sandy, I would really like to thank you for helping me with all of the milestones of my graduate school career. Monica, you are always the best. Thank you for all your help on all the paper work. I would also like to thank Julie and all of the other members of the department for your help.

I appreciate having a lot of great friends in graduate school. I would especially like to thank Liang, Dan, Yu-Chuan, Ying, Ya, Suiwen, Xu, Feiyu and Yin. Your mental support helped me get through difficult periods of my graduate school career. I would also like to thank my cousin Hang for helping me with some geometrical treatment in the research.

CONTRIBUTORS AND FUNDING SOURCES

This work was supervised by a dissertation committee consisting of Professor Simon North, Timothy Hughbanks, and Christian Hilty of the Department of Chemistry, and Professor Alexei Sokolov of the Department of Physics and Astronomy.

The computational chemistry results for Chapter V were provided by Professor George McBane of the Department of Chemistry, Grand Valley State University. The NO_2 images in Chapter IV were previously published in 1999 and provided by Professor Yuxiang Mo of the Department of Physics, Tsinghua University and Professor Toshinori Suzuki of the Department of Chemistry, Kyoto University. The OCS experimental data and analysis in Chapter IV and Chapter V were conducted in collaboration with Colin Wallace of the Department of Chemistry and were published in 2016 and 2017. The derivation of the 2+1 REMPI Equations in Chapter III was an extension of the work of Dr. Michael Grubb of Fort Lewis College, who also contributed to the derivation. He also provided the image accumulation programs mentioned in Chapter II.

All other work conducted for the dissertation was completed by the student under the advisement of Dr. Simon North of the Department of Chemistry.

This work was made possible in part by Robert A. Welch Foundation under Grant Number A-1405.

TABLE OF CONTENTS

Page

LIST OF FIGURES

Page

LIST OF TABLES

Page

CHAPTER I

BACKGROUND AND INTRODUCTION*

The field of gas phase reaction dynamics study can generally be divided into two categories: unimolecular reaction dynamics and bimolecular reaction dynamics. Photodissociation dynamics is a unique subject under the unimolecular reaction dynamics. Photodissociation can be viewed as unimolecular reactions in which the reactants initial states are prepared by the photons and evolve on one or several potential energy surfaces. In order to understand photodissociation dynamics, we need to understand not only the unimolecular dynamics on a single potential energy surface (ground or excited surface), but also the photo-matter interactions occurring before the involvement of unimolecular reactions. [1]

When a molecule absorbs a photon which has a sufficient amount of energy, the molecule is excited to a higher energy electronic state. Depending on the nature of the excited state, the excited molecule will behave differently. If the excited state is repulsive, the molecule will evolve on this surface and dissociate. If the excited state is a bound state, several processes can happen next. The molecule can emit a photon and relax to either another excited or the ground state. Alternatively, several non-radiative decay processes can occur. For example, the molecule can undergo a non-adiabatic transition to a dissociative state and dissociate on that state's potential energy surface. Finally, the excited molecule can undergo internal conversion to the ground

---

* Part of this chapter is reprinted from "D. W. Chandler and P. L. Houston, The Journal of Chemical Physics 87 (2), 1445 (1987)", with the permission of AIP Publishing.

electronic state, resulting in the redistribution of the excess of energy among the vibrational modes which could also lead to dissociation.[2-6]

There are still numerous challenges in understanding the photodissociation dynamics. For example, the excited electronic state potential energy surfaces are usually less well-determined compared to the ground state surfaces. Besides, it is also difficult to locate the non-adiabatic coupling between excited state potential energy surfaces, which makes the interpretation of experimental results of multi-state photodissociation still difficult. Experimental photodissociation studies are needed to be able to increase our knowledge of the characteristics of the excited state potential energy surfaces and the unimolecular reaction dynamics evolving on these excited states, which are otherwise difficult to access.

Another benefit of photodissociation dynamics study is that the photodissociation can be viewed as a “half-collision” reaction. The process of molecules being prepared in a certain reactive state and evolving toward dissociation is the inverse process of a reactive collision. If we view the photo-prepared unimolecular reaction as an inverted bimolecular collision reaction, then the special benefit of studying such “bimolecular reactions” is that specific factors of the “collision” process, like the internal state selection and the total angular momentum, can be well controlled. Such conditions are usually difficult to control in experiments studying bimolecular reactions, like crossed molecular beam experiments.[7]

There are two general philosophies for the experimental study of photodissociation dynamics. Modern experimental technologies, like femtosecond lasers, allow us to directly probe the transition state of the reaction.[8] But a large amount of experimental study is still following the traditional philosophy: explicitly observe the

characteristics of the product from the photodissociation process and infer the dynamics. These characteristics include scalar properties like energy partitioning between kinetic energy and internal energy. They also include vector correlations, the relative orientations of the transition dipole moment of the parent molecule **μ**, the recoil velocity vector of photofragments **v**, and fragment rotational angular momentum vector ***j***. Different reaction dynamics will lead to different product energy partitioning and vector correlations. This methodology is similar to the investigation of a crime scene: detectives investigate the observable clues after the crime and try to recover what has happened.

The Development of Experimental Techniques and Their Impacts

The vast development of experimental technology is one of the primary driving forces behind advancement in the field of molecular dynamics. Just one hundred years ago, the study of how chemical reactions happen would mean studying the macroscopic behaviors of solutions/ gas/ solid samples using traditional bench chemistry methods. Studies of reactions on the molecular level were possible only using either spectroscopic methods or theoretical calculations (pens at that time). During this one hundred year period, with the rapid development of instrumental techniques and the inspirations from other disciplines like particle physics and surface chemistry, scientists were able to experimentally measure scalar and vector properties of photofragments, not only at the molecular and atomic level, but also at the internal energy state level. Among all of these advancements in experimental methods, the internal state distribution measurements, the photofragment translational spectroscopy methods and

the correlated measurements are the three keys to the experimental photodissociation dynamics study.

In the late 1970's, the development of tunable dye laser technology made a large number of new spectroscopy methods possible, like laser induced fluorescence (LIF) ,[9, 10] resonance enhanced multi-photon ionization (REMPI)[11] and coherent anti-Stokes Raman spectroscopy (CARS)[12]. With these methods, scientists are able to measure internal energy state population distributions of the photofragment. This was the first giant step toward a full map of the energy partitioning during the photodissociation.

The first several photofragment translational energy spectroscopy measurements were reported around the same period of time.[13, 14] These types of experiments measure photofragment product speed distributions. In the experiment, the molecular beam is dissociated by a pulsed laser and the photofragments are detected by the electron impact ionization detector. The arrival time of the atomic fragments are measured by the quadrupole mass selector and can be converted to speeds. Although such method is sensitive and can successfully provide speed distributions of the photofragments, it does not have fragment internal state selections.

The next breakthrough was the correlated measurement, the measurement of the speed of the products in coincidence with their internal energy. Such coincident measurement is necessary because a full picture of energy partitioning among the products not only includes the internal state distributions of both fragments, but also includes the correlation between the internal energy of the fragments. Take a simplified example of flipping a quarter and a nickel. If the two coins are ordinary, the probability of having heads for both coins is 0.25. An alternate scenario consists of two coins that

are specially designed so that whenever one of them lands on a head/tail, the other one will also land on a head/tail respectively. In such a case, the possibility of having heads for both coins is 0.5. In order to determine whether they are special coins, we measure the possibility of getting head and tails. If we only flip one coin at a time, we will get possibility of 0.5 for both coins and will not be able to determine whether the coins are special or normal. Only by making correlated measurements (flip both coins simultaneously and record the results) can we determine the truth.[15] When measuring the fragment speed distribution in coincidence with the internal state distribution, energy conservation will be able to provide information about internal state distributions in coincidence with the co-fragment internal state distributions.

In the early stages, such correlated measurements were experimentally achieved by a combination of the two methods above: the speed measurement methods like Doppler technique[16] / time-of-flight (TOF) spectrometer[17], and the internal state distribution measurement methods like LIF/ REMPI. One example is measuring the Doppler profile broadening of the LIF of probing the ground state H atoms formed from the photodissociation of HI at 266 nm.[16] The combined measurements can make quantum state selections and measure the speed distribution of the selected fragment. These correlated measurements are quite successful, despite the limits of resolution. The limits are primarily in the speed detection: it is a one-dimensional speed detection. The more speed components that exist, the harder it is to achieve small error bars for each component.

Inspired by the electron stimulated desorption ion angular distributions (ESDIAD) experiments in surface science[18], Houston and Chandler combined TOF spectrometry and the micro-channel plate based two-dimensional detection technique

and developed the imaging technique in 1987.[19] Figure 1.1 shows their first image. With proper reconstruction algorithms developed over time,[20-27] three dimensional information can be recovered from the two-dimensional projection images.

In the past 30 years, the imaging technique has become widely accepted and applied. A number of improvements have also been introduced. The most important improvement is the velocity mapping technique.[28] By utilizing a set of Einzel lenses, ions with the same velocity will be focused onto the same detector spot. The resulting velocity map ion images (VMI) have better speed resolution. Meanwhile, rapid development of CCD cameras has made image accumulation and processing significantly easier. The speed resolution is further increased by image processing algorithms by Chang *et al*.[29]

There are a number of advantages of the velocity map ion image technique. This technique has reasonable speed resolution. It can make correlated measurements of fragment speed and internal state distributions. The analysis of the correlated measurements is also straight forward. But the most important advantage of the VMI technique is the ability to measure photofragment angular distributions and vector correlations. Although previous techniques like Doppler spectroscopy and TOF can also measure vector correlations, the VMI technique is capable of measuring speed-dependent vector correlations in a much easier way, which will be discussed later.

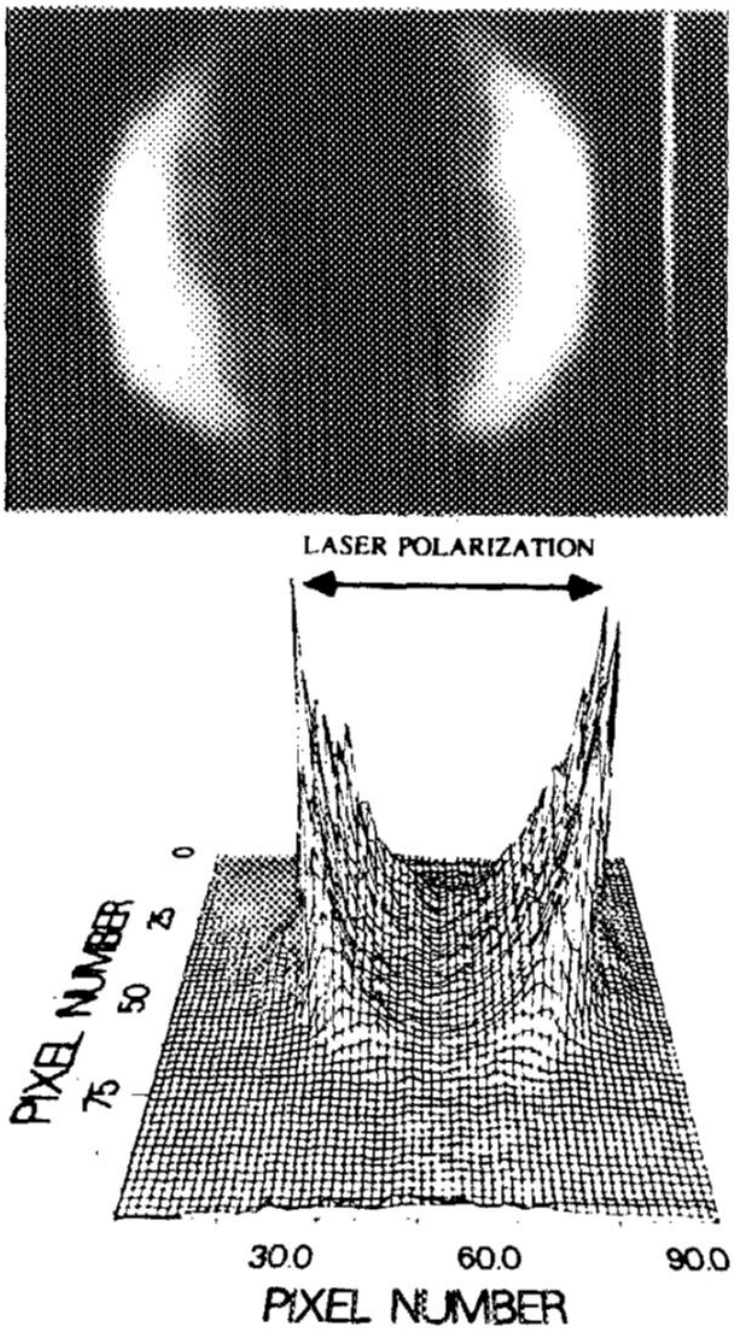

Figure 1.1: The first ion image. CH_3 ion image from photodissociation of CH_3I at 266 nm. Figure reproduced from Chandler and Houston, JCP 87, 1445 (1987).[19]

The Vector Properties

Besides scalar properties, researchers are also interested in the photofragment anisotropic product distributions, which arise from vector properties. Vector correlations, which describe the relative orientations of the transition dipole moment of the parent molecule **μ**, recoil velocity vector **v**, and angular momentum vector of photofragment rotation ***j*** are sensitive probes of the stereodynamics of photodissociation reactions. The most widely discussed vector correlation as discussed above, is the **μ-v** correlation. When a molecular beam is intercepted by the laser, the molecules which have their transition dipole moments **μ** parallel to the photons' electric field are most likely to be excited, and when excitation leads to dissociation, the recoil velocity **v** of the photofragments will be along the broken bond (axial recoil).

The photofragment angular distribution was theoretically described by Zare and Herschbach.[30, 31] The photofragment density for a diatomic molecule is characterized by the spatial anisotropy parameter β according to the Equation:

$$I(\theta) \propto 1 + \beta P_2(\cos\theta_v) \tag{1.1}$$

where P_2 is the second Legendre polynomial and θ_v is the angle between the outgoing fragment velocity and the polarization vector of the photodissociating light. The β is defined as $\langle P_2(\cos\theta)\rangle$ where θ is the angle between the transition dipole moment of the parent molecule **μ** and the recoil velocity vector **v** of the photofragment. For a linear diatomic molecule in the axial recoil limit, β is +2 for a purely parallel transition and -1 for a purely perpendicular transition.

The direction of the transition dipole moment with respect to the molecule is dependent on symmetry of the initial and final states. If the symmetry of the initial and final states is conserved, the transition dipole moment will be parallel to the primary

symmetry axis of the parent molecule. If the symmetry of the initial and final states is different, the transition dipole moment will be perpendicular to the primary symmetry axis of the parent molecule. These mean that if such spatial orientation can be preserved, the product recoil will be anisotropic, and the distribution will indicate the nature of the parent molecule excited state symmetry. Such information can provide helpful feedback for computational chemists.

Sometimes the measured **μ-v** correlations deviate from the symmetry predicted by computational chemistry; this may indicate that a surface crossing is taking place.[32] The **μ-v** correlations make large contributions to the observed anisotropy of the photofragment angular distribution. However, the angular distribution can also be affected by other correlations if the fragments have rotational angular momentum alignment. In other cases, if the rotation of the parent molecule during the dissociation process is significant, the anisotropy of the fragment angular distribution will be decreased. Other factors can also affect the anisotropy, which will be discussed later.

Experimentally, **μ-v** correlations were first observed by Solomon.[33] Later in the 1970's, **μ-v** correlations were also observed from photofragment translational energy spectroscopy experiments.[13, 14] Since then, **μ-v** correlations have become as widely measured as scalar properties in photodissociation dynamics studies. Almost all the experimental methods that can make correlated measurements are able to measure product angular distributions.

The relative orientation of the photofragment rotational angular momentum ***j*** can also provide useful information. **μ-*j*** correlations can tell us about the direction of photofragment rotations with respect to the parent molecule transition dipole moment, which can be important supplements to the **μ-v** correlations. The laboratory frame

direction of the angular momentum can be probed by the direction sensitive interactions between the electric vector of the probe laser and the transition dipole moment of the photofragment $\boldsymbol{\mu}_{\mathbf{frag}}$. The relative direction of $\boldsymbol{\mu}_{\mathbf{frag}}$ with respect to ***j*** depends on the detection rotational transition branch. Classically, for each resonant photon, the $\boldsymbol{\mu}_{\mathbf{frag}}$ of a $\Delta j=0$ transition is perpendicular to the fragment rotational plane and parallel to ***j***, and the $\boldsymbol{\mu}_{\mathbf{frag}}$ of a $\Delta j=\pm 1$ transition is in the fragment rotational plane and perpendicular to ***j***.[34] A more detailed description beyond the classical picture can be found in the literature.[30, 35, 36]

Since correlations can exist between **μ-v** and **μ-*j***, it can be naturally inferred that correlations between **v-*j*** exist. In fact the **v-*j*** correlation also plays a significant role in interpretation of photodissociation dynamics. [37-40] The **v-*j*** correlation originates from the forces and torques acting during the product formation process, and provides a direct and intuitive image of the photofragments motion as they leave each other. Their correlations can range from **v** parallel to ***j***, like the OH fragments leaving each other with "helicoptering" motion in H_2O_2 photodissociation,[41] to **v** perpendicular to ***j***, like the NO fragment leaving the dissociated NO_3 with "cartwheeling" motion [42, 43]. The **v-*j*** correlation is retained even in slow dissociation processes when no memory of the lab-frame alignment of the parent molecule transition dipole moment is preserved. An example of correlations of **μ**, **v** and ***j*** is shown in Figure 1.2.

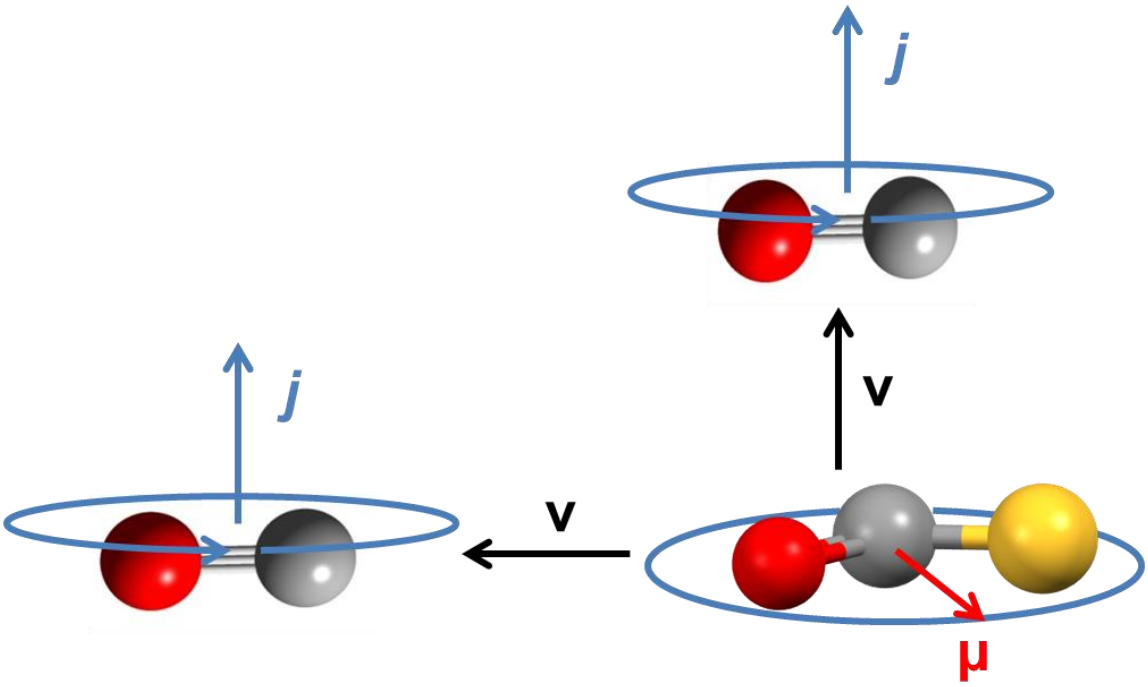

Figure 1.2: Schematic diagram of vector correlations. The OCS molecule is bent in the excited state, with μ in the plane. The CO fragment can either be ejected with "helicoptering" or "cartwheeling" motions.

The **v-*j*** correlations can not only arise from dynamical effects of photodissociation, they can also be observed in statistical unimolecular reactions due to conservation of angular momentum which results in **v-*j*** correlations.[44, 45] If the rotational angular momentum of one fragment cannot be balanced by that of the co-fragment, the outstanding angular momentum has to be balanced by the relative orbiting of one fragment with respect to the co-fragment.

One should be cautious when interpreting the vector correlation information from experimentally observed anisotropy parameters as they can be affected by several factors.[46-50] If the time period between the parent molecule photo-excitation and

dissociation is comparable or longer to the parent molecular rotation time period, significant decrease of anisotropy parameters can occur. Non-coherent simultaneous parallel and perpendicular excitation transitions to excited states which lead to the same photofragment can result in a reduction of the observed anisotropy parameters. Even for a fast dissociation, parent vibrational motion can change the image anisotropy parameters in certain situations. Near the dissociation threshold, the axial recoil approximation no longer holds and photofragment recoil can deviate from the axis of the broken bond. It has been reported that in the case of direct photodissociation of triatomic molecules, if the available energy is primarily partitioned in the diatomic molecule rotational energy so $E_{trans} << E_{rot}$, the observed image anisotropy can deviate from the limiting cases significantly.[51, 52]

Vector Correlation Information from Experiments

Experimentally, information about vector correlations can be extracted from measurements of anisotropic signal distributions in the laboratory frame. Examples of commonly used experimental methods are Doppler spectroscopy,[39, 53-55] ion time-of-flight,[56, 57] and ion imaging experiments.[3, 35, 58, 59] A significant advantage of measuring vector correlations with ion imaging, especially the DC-sliced imaging technique, is the straight forward measurement of “speed dependent vector correlations”. When there is more than one product channel involved in a photodissociation processes, it is not uncommon to observe different dynamics in each channel. Therefore, it is important to be able to measure the individual product angular distribution of each speed component. The fragment images will be able to show all of the channels with their corresponding speed components. Each speed component can show its own angular

distributions. In this way, we can make correlated measurements of vector correlations of each channel, instead of measuring the averaged vector correlations of all the product channels. An example can be found on the study of stereodynamics of NO_3 photodissociation.[43]

In ion imaging, the photon absorption probabilities of parent molecules are $\cos^2(\theta)$ dependent, where θ is the angle between the transition dipole moment $\boldsymbol{\mu}_{\mathbf{par}}$ and electric field vector of dissociation laser for single photon dissociation, resulting in an angular dependent distribution of photofragment ensemble. Photofragments are detected using Resonance Enhanced Multi-Photon Ionization (REMPI) and the detection probabilities of photofragments of the same quantum states are also dependent on the angle between the rotational angular momentum vector ***j*** and electric field vector of probe laser. The probed photofragment ion ensemble can be more than $\cos^2(\theta)$ dependent because of the correlations with ***j***.[1]

The resulting anisotropy of the collected ion image will be a product of the angular distribution of photofragments (dependent on the relative photodissociation laser polarization) along with their angular sensitivity to detection (dependent primarily on the probe laser polarization). In cases where multiple vectors are correlated, several combinations of different photodissociation and probe laser polarizations (parallel or perpendicular to image plane) are needed to provide enough information to determine the correlations of all the vectors. By changing the probed REMPI branch with both lasers' polarizations fixed in a parallel geometry in the imaging plane, it is also possible to determine the vector correlations. [1, 60]

In the past several decades, numerous different formalisms have been used to describe photofragment vector correlations.[34-36, 59, 61] Rakitzis and coworkers developed

an alternative approach using polarization parameters $a_q^{(k)}(p)$, later $a_q^{(k)}(s)$, which are widely used in the field of stereodynamics and take coherent rotational alignment effects into consideration.[35, 36] However, previous publications have shown that in the high-*j* semi-classical limit, the contribution of coherence effects to the angular momentum polarization of photofragment is 1/*j* dependent, and coherence terms have been reported in a limited number of experiments.[62, 63]

The semi-classical bipolar moment formalism of Dixon offers a description with straightforward physical interpretations.[34] The bipolar moments $\beta_Q^K(k_1k_2)$ are the expansion coefficients for bipolar harmonics which describe the spatial probability distributions of **v** and ***j*** with respect to lab-frame aligned **μ** vector during the photodissociation process. The bipolar harmonics is given as:

$$B_{KQ}(k_1k_2;\theta_t\phi_t\theta_r\phi_r) = \sum_{q_1}\sum_{q_2}(-1)^{K-Q}[K]^{1/2}\begin{pmatrix} k_1 & K & k_2 \\ q_1 & -Q & q_2 \end{pmatrix} \times C_{k_1q_1}(\omega_t)C_{k_2q_2}(\omega_r) \quad (1.1)$$

K, k_1 and k_2 are the rank of the spherical harmonics, Q, q1 and q2 are the 2K+1 component of the formula, respectively. K, Q describe the photon interaction with the system, and the two sets of lower case k,q describe the two other vectors, **v** and ***j*** of the system. For systems with one photon dissociation using linearly polarized laser, K=0,2 and Q=0. k_1, k_2 values can be higher than 2 and is determined by number of probe photons. θ and ϕ describe the polar angle and azimuth angle of a vector, with subscription t indicating **v** and subscription t indicating ***j*** vector. ω is the dihedral angle and in our case usually applied as ω_{tr} meaning the dihedral angle between **v** and ***j***.

Imaging experiments with one photon dissociation followed by 2+1 REMPI detection will be sensitive to nine relevant bipolar moments.[34, 64] Conveniently, the

$\beta_0^2(20)$ (**μ_{par}-v**), $\beta_0^0(22)$ (**v-*j***), and $\beta_0^2(02)$ (**μ_{par}-*j***) low order bipolar moments can be interpreted semi-classically as the expectation values of the second Legendre polynomial: $\langle P_2(cos\theta)\rangle$ where θ is the angle between two relevant vectors, respectively. For example, $\beta_0^0(22)$, where θ is the angle between the **v** and ***j*** vectors, gives limiting values ranging from -0.5 if the vectors are perpendicular, to 1 if the vectors are parallel. The $\beta_0^2(22)$ moment is usually referred to as the "triple vector" correlation which describes the relative orientation of all three vectors. The other bipolar moments, $\beta_0^0(44)$, $\beta_0^2(24)$, $\beta_0^2(42)$, $\beta_0^2(44)$ and $\beta_0^2(64)$, are high order moments. The $\beta_0^0(44)$ moment can be interpreted semi-classically as the expectation value of the fourth order Legendre polynomial: $\langle P_4(cos\theta)\rangle$ where θ is the angle between the **v** and ***j*** vectors. The rest of the high order bipolar moments describe the correlation between all three vectors and are not physically intuitive. The ranges of values for physically meaningful bipolar moments are given by Dixon and shown in Table 1.1 below. A more detailed discussion can be found in Dixon's work.[34]

Table 1.1: The ranges of values for physically meaningful bipolar moments. The data in this table are adapted from Dixon, JCP, 85 (4), 1866 (1986).[34]

	Lower limit	Upper limit
$\beta_0^2(20)$	-0.5	1
$\beta_0^2(02)$	-0.5	1
$\beta_0^0(22)$	-0.5	1
$\beta_0^2(22)$	-1	0.5
$\beta_0^2(24)$	-0.5	1
$\beta_0^2(44)$	-1	0.75
$\beta_0^0(44)$	-3/7	1
$\beta_0^2(42)$	-0.5	1
$\beta_0^2(64)$	-0.5	1

CHAPTER II

THE EXPERIMENTAL APPARATUS AND THE IMAGES*

A Brief Overview of VMI Apparatus

The molecular beam/velocity map ion imaging (VMI) apparatus is assembled in the Department of Chemistry, Texas A&M University, with chamber parts from Dr. Paul Houston's laboratory at Georgia Institute of Technology.[65, 66] A general diagram of the apparatus is shown in Figure 2.1. The apparatus consists of three collinearly arranged sections: the source, the main (ionization), and the detector regions, arranged collinearly. The source and the main region are separated by a conical skimmer. A gate valve is used to separate the detector region from the main region. Each of the regions has a connected turbo-molecular pump, which is backed by a mechanical vacuum pump.

* Part of this chapter is reprinted from "W. Wei, C. J. Wallace, G. C. McBane and S. W. North, The Journal of Chemical Physics 145 (2), 024310 (2016) ", with the permission of AIP Publishing.

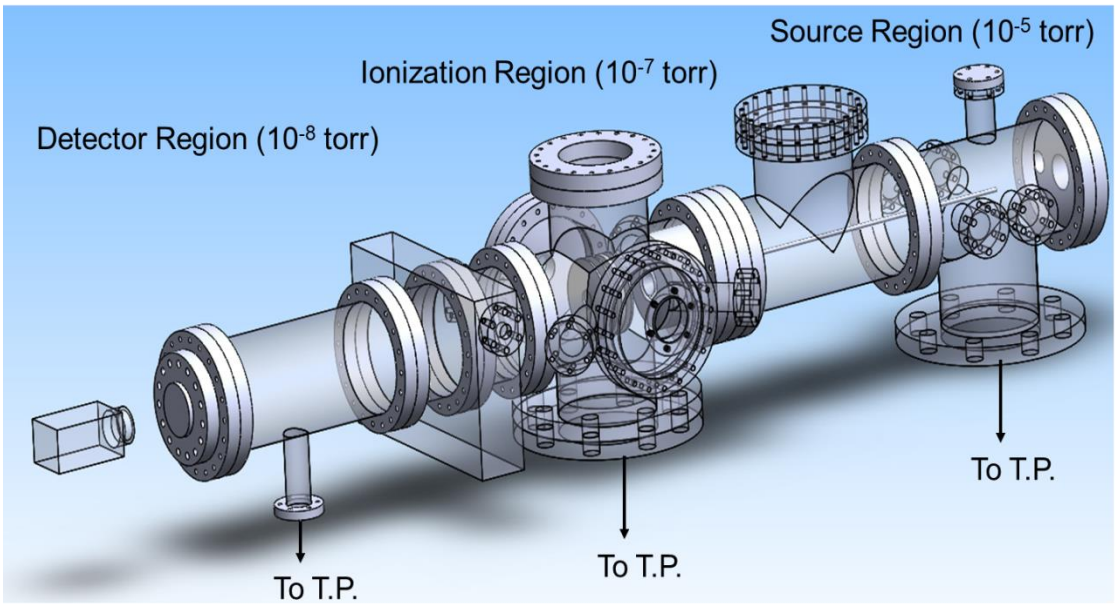

Figure 2.1: Diagram of the vacuum chamber system. The supporting vacuum lines and pumps are not shown.

The apparatus is under high vacuum during experimental operations. The pressure of the source chamber is typically about $3x10^{-6}$ torr, and increases to $9x10^{-5}$ torr when samples are injected. The pressures in the main region are typically $2x10^{-6}$ torr with minimal change during samples injection. The detector region pressure is about $1x10^{-7}$ torr during operation. When experiments are not being conducted, the gate valve between the main and detector region is closed, and the pressure in the detector region is maintained at around $5x10^{-8}$ torr. The benefit of high vacuum is to provide a "collision-free" environment for the experiment. The measurements of scalar and vector properties of photodissociation dynamics rely on the preservation of the recoil velocity of the photofragments. If photofragments collide after produced, both the magnitude and the direction of recoil velocity of the photofragments can be altered. The mean free

path of molecules in the atmosphere is around 70 nm, while at $5x10^{-6}$ torr it is around 10 m. Thus in high vacuum, most of the photofragments will not undergo any collisions before reaching the detector. Besides, the detector components are air sensitive and should be kept under vacuum.

During experimental operations, a free jet expansion molecular beam is produced by a General Valve series 9 pulsed valve in the source region. The pulsed valve opens at a repetition rate of 10 Hz and has an opening time of 500-700 μs, depending on the desired molecular beam condition. The molecular beam will be collimated by the conical skimmer and enter the main region. There are four einzel lenses with bores in the center of each lens plate, and the molecular beam travels through the bore of the first lens (the Repeller). Two windows, one on each side of the chamber, allow counter-propagating laser beams to intersect the molecular beam at 90°, in the interaction region between the Repeller and the second einzel lens. The lasers will dissociate the molecules in the beam and selectively ionize the photofragments. The photo-ions will be accelerated by the einzel lenses toward the detector. The acceleration of the ions by the einzel lenses is important for both time-of-flight mass selection and velocity mapping. The accelerated photo-ions will travel through an electric field free tube with a total length off 76 cm, and will be detected by a time-gated ion detector. The key of the velocity mapping condition is that the ions with the same velocity will be focused onto the same position of the detector, regardless of starting position.

The detector, which faces the beam source, contains a two-dimensional position sensitive device: a pair of 40 mm diameter chevron microchannel plates (MCP). A high-voltage pulse generator (DIRECTED ENERGY, INC) supplies the MCP with high

voltage pulses, with 2200V high position (open), 1300V low position (close), and pulse durations between 40ns – 200ns depending on experimental requirements. Each ion hitting the positively charged MCPs will generate a cascade of electrons. This cascade will hit a P51 phosphor screen, located behind the MCPs and will produce an instant glow spot on the phosphor screen. Generally the signal quantity correlates to the MCP high voltage pulse duration, and the intensity of each signal spot correlates to the pulse voltage. The instant overall signal intensity is collected by a Hamamatsu R928 photomultiplier tube (PMT). An IDS uEye gated CCD camera is used to record the two dimensional signal on the phosphor screen. A picture of the detector region is shown in Figure 2.2.

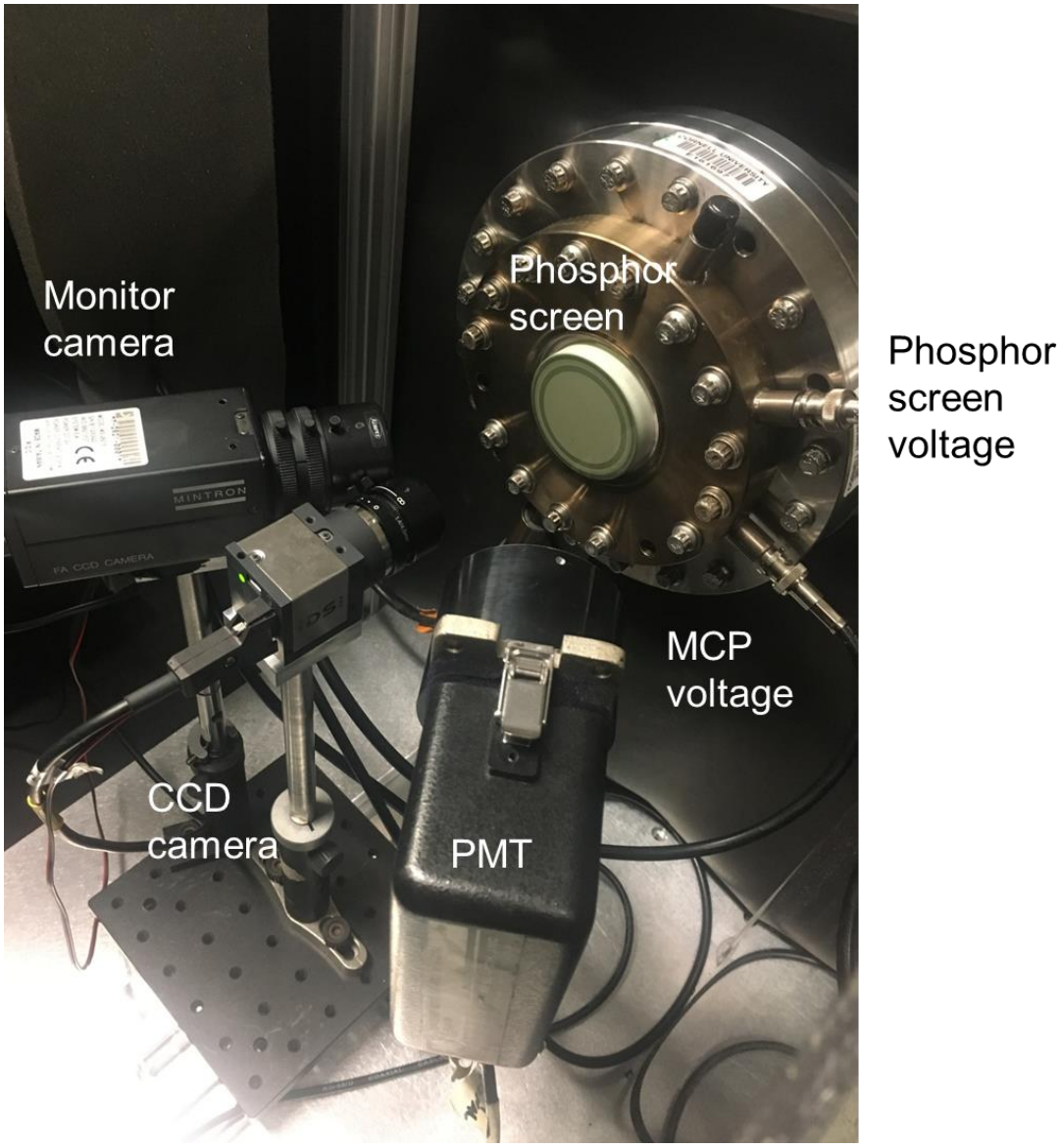

Figure 2.2: A picture of the back of the detector. The monitor camera serves as an instant image monitor, not a required component.

The entire velocity map ion imaging apparatus also includes laser systems, control units and signal acquisition system. The layout of the entire experimental set up is shown in Figure 2.3.

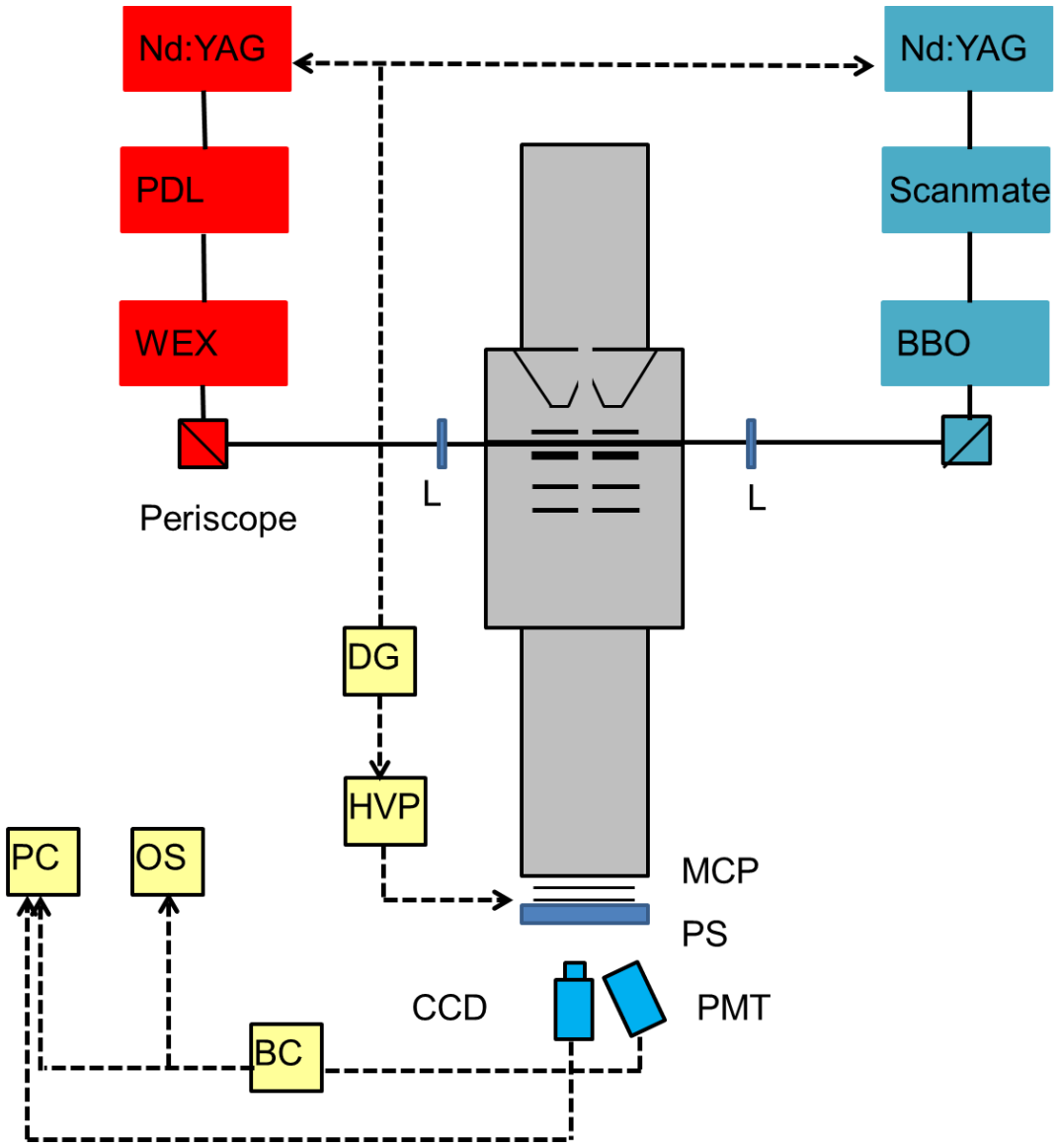

Figure 2.3: Schematic diagram of experimental setup. PDL: Pulsed dye laser; WEX: wavelength extender; BBO: Beta Barium Borate crystal; L: lens; MCP: microchannel plate; PS: phosphor screen; CCD: IDS uEye gated CCD camera; PMT: photomultiplier tube; DG: delay/pulse generator; HVP: high voltage pulse generator; OS: oscilloscope; BC: Boxcar average; PC: computer.

In order to obtain image signal, all of the components need to be synchronized. The pulse valve, the lasers, the detectors, need to be well times so that the pulsed molecular beam can be intercepted by the pulsed laser and the mass-selected ion signals generated can be detected. This synchronization is achieved by using delay generators (by Berkeley Nucleonics Corporation and Stanford Research Systems) to externally control the instruments. It also serves as the master clock of the system. The probe laser is delayed for 25 ns after the firing of the dissociation laser. The pulse valve opening time is set to be 480-1180 μs (usually 880 us) before the dissociation laser so that the molecular beams can arrive at the interaction region in the main chamber when the lasers arrive. The core of the detector, the MCPs require a pulsed high voltage to make mass selection. The high voltage pulse is in active around 3-12 us after the dissociation laser, depending on the mass to be selected. The camera is usually timed to open for 98 μs at 1056 μs after the dissociation laser. A schematic diagram of pulse sequences is shown in Figure 2.4.

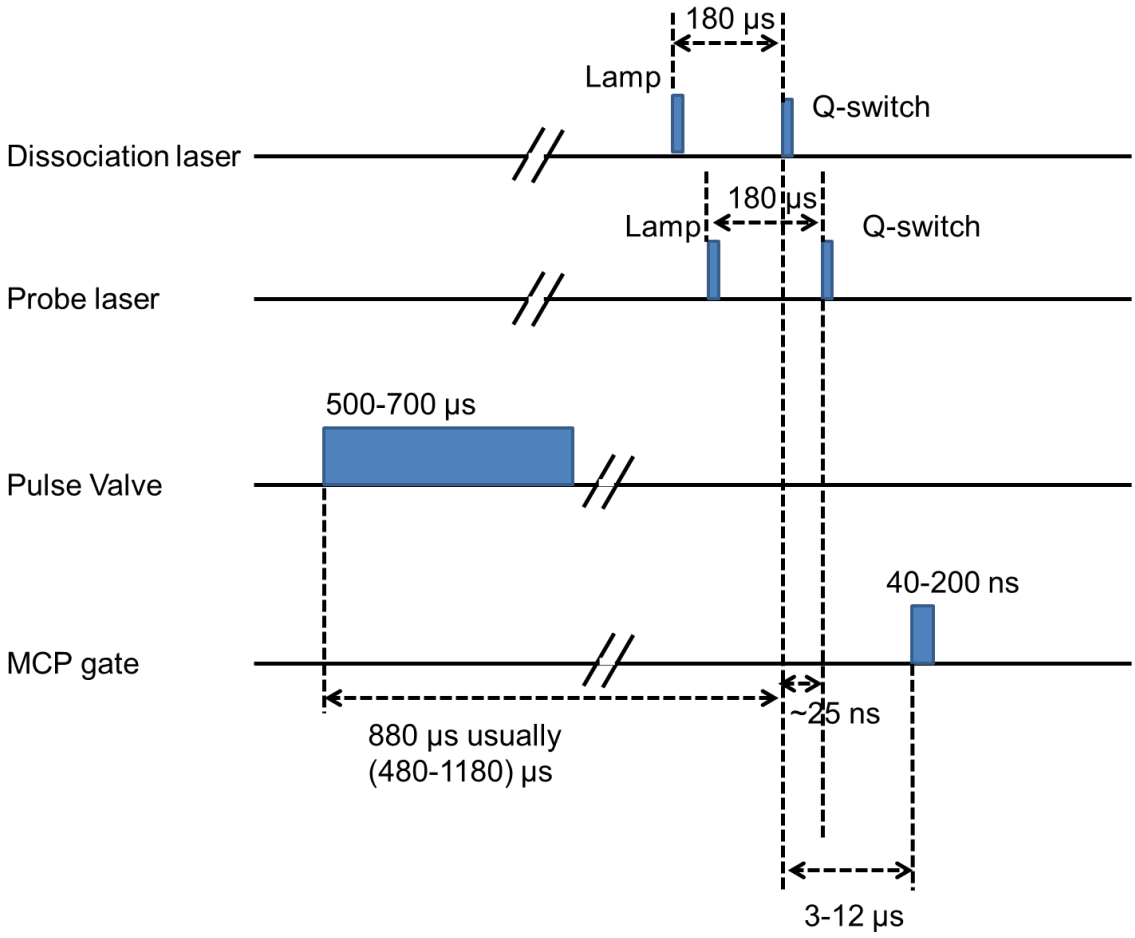

Figure 2.4: Pulse sequence for lasers, pulse valves and high-voltage pulse (mass gate).

The Molecular Beam

The sample gas is made by flowing 1 atm of helium through a bubbler containing liquid OCS at 196 K, yielding ~25% OCS in the molecular beam. The sample is made into a molecular beam and the beam goes through supersonic expansion. The supersonic expanded beam will be collimated by a conical skimmer. The supersonic expansion efficiency depends on the distance between the tip of the skimmer and the

aperture of the pulse valve. An ideal distance will be 20 times of the aperture size of the pulse valve, which is 2 cm in our system.[3, 4]

The purpose of employing supersonic expansion is to greatly reduce the internal energy of the parent molecule, which is necessary to ensure the precision of photofragment kinetic energy measurements. Characterization of the rotational temperature is conducted by measuring the E-X resonance-enhanced multi-photon ionization (REMPI) spectrum of a molecular beam with a 5% mixture of CO in helium gas. A forward convolution simulation with a Boltzmann distribution is used to fit the CO E-X REMPI spectrum. From simulation, the principal rotational temperature of the CO molecular beam is about 8 K. The rotational temperature of OCS in the molecular beam has not been evaluated separately. The details of REMPI spectrums and forward convolution simulation will be discussed later.

The temperature in the molecular beam is not uniform. The internal energy of the molecules in the early period of the pulse is higher, and in the later period is lower. We usually conduct the photodissociation experiments on the middle period of the pulse.

The Lasers

The experiments usually involve two counter-propagating linearly polarized lasers. One laser is used to dissociate the parent molecules and the other laser is used to selectively ionize the photofragment of interest. In some “one color experiments”, the same laser supplies photons to dissociate and probe the photofragments. In order to maintain a high photon density for dissociation and ionization, the laser beams are focused into the interaction region using lens. The lasers are pulsed with a 10Hz

frequency and the wavelengths are typically in the ultraviolet range. The lasers are linearly polarized to provide a laboratory frame direction. The polarizations of laser is either set as “horizontal”, meaning the electric field vector of the laser is polarized along the direction of the molecular beam (z axis, H geometry) and perpendicular to the detector plane; or “vertical”, meaning the electronic vector of the laser is polarized parallel to the detector plane in the laboratory frame (x axis, V geometry).

There are four major experiments presented in this dissertation: probing the CO fragment of the photodissociation of OCS around 230 nm with a 214 nm laser, probing the S fragment of the photodissociation of OCS around 214 nm with a 291.18 nm laser, and probing the CO of the photodissociation of OCS around 214 nm with a 230 nm laser and with a 214 nm laser. The 230 nm pulsed laser is generated by a Spectra Physics Lab-150-10 Nd:YAG using the third harmonic (355 nm) to pump a LAS LDL 2051 dye laser to generate laser wavelengths around 460nm (Coumarin 460 laser dye with methanol solvent). The dye output is frequency doubled to generate wavelength corresponding to the 2 + 1 REMPI transitions of CO through the B-X (0,0) and (1,1) band (229-230.5 nm).[67, 68] The laser power was between 150-400 μJ/pulse. The laser beam is focused into the interaction region using a 30 cm focal length lens. The 291.18 nm laser was generated by the second harmonic of a Spectra Physics Lab-150-10 Nd:YAG (532 nm) which pumped a PDL-1 dye laser (Rhodamine 610 laser dye with methanol solvent). The output was frequency doubled by the Wavelength Extender (WEX) for the 2+1 REMPI transition of S($^1D_2$) at 291.18 nm via the $^3P_1$ intermediate state[69, 70] and focused into the interaction region using a 30 cm focal length lens. Typical energy for the 291.18 nm pulses was 900 μJ/ pulse. The 214 nm laser was generated by the third harmonic of a Spectra Physics Lab-150-10 Nd:YAG laser (355 nm) which

pumped a Lambda Physik Scanmate dye laser (EXALITE 428 laser dye with p-Dioxane solvent) to generate 430 nm. The dye laser output was frequency doubled using a type-I Beta Barium Borate (BBO, from CASIX) crystal to generate wavelengths corresponding to the 2 + 1 REMPI transitions of CO through the E-X (0,0) band (213-216 nm).[67, 68, 71]The focus of the 214 nm pump beam was detuned when collecting the sulfur images. The typical energy for the 214 nm pulses was 500 μJ/ pulse. Each light beam coming out of the laser is sent through a set of periscope lenses with the top lens vertically rotated 90 degrees from the position that is parallel to the bottom lens. Such periscope can adjust the direction and height of the laser beam. More importantly, it can rotate the polarization of laser.

Another attempt was also made to obtain pulsed laser at wavelength around 215 nm by frequency tripling of laser wavelength around 645 nm. The vertically polarized 645 nm fundamental laser (typically 35 mj/ pulse) is generated by the second harmonic of a Spectra Physics Lab-150-10 Nd:YAG (532 nm) which pumped a PDL-1 dye laser (DCM laser dye with methanol solvent). The output was frequency doubled by the WEX to generate a horizontally polarized laser with wavelengths around 322.5 nm with a power of 1 mJ/ pulse. The doubling efficiency is around 10% with a typical power of 5 mj/ pulse and in this particular case the doubled laser will not be separated from the residual fundamental 645 nm laser. The frequency tripling required the polarization of both the 322.5 nm and 645 nm lasers to be the same. Accordingly, the 645nm laser polarization needed to be rotated by a half-wave plate, ideally with coating specifically for 645 nm light. Since such precisely coated plates are not available, a more practical way is to employ a half-wave plate (Thorlabs, Inc) with coating for 633 nm light, and precisely tilt it around the vertical axis so that the tilted 633 nm coating is equivalent to

the coating for 645 nm light. The combination of horizontally polarized 322.5 nm laser and vertically polarized fundamental 645 nm laser is sent through the finely tilted half-wave plate with coating for 633 nm (Thorlabs, Inc) to rotate the polarization of the residual 645 nm laser to horizontal direction. The polarization of the co-propagated 322.5 nm laser will not be altered in this situation. The combined laser beams are then sent through a Type I BBO crystal with finely tuned incident angle to achieve frequency tripling. The resulting 215 nm laser beam is vertically polarized with a typical power of 100 μJ/ pulse and a power efficiency of 0.3%. A Pellin-Broca prism is used to separate the 215 nm laser from the other laser beams.

There are several technical issues with this method in our laboratory. The primary reason is that the line-width of the fundamental dye laser (0.01 nm) is not sharp enough. The frequency doubling and tripling efficiency is highly dependent on the line-width of the fundamental laser. Thus the output 215 nm laser power is too low to be sufficient for our experiments. Besides, frequency tripling efficiency is highly sensitive not only to the phase matching angle of the non-linear optics for frequency doubling and tripling, but also to the tilting angle of the half-wave plate mentioned above. In the experiments the tilting angle and BBO phase matching angles can be optimized with regard to 215 nm power at each wavelength. However, when scanning of wavelength is needed (which is often), the half-wave plate, the frequency doubling and tripling crystals all need to be step-wise optimized simultaneously to maintain the 215 nm laser power which is hard to achieve in our experimental setting.

When the molecular beam enters the interaction region in the main chamber, some of the parent OCS molecules absorb photons and dissociate. In our experimental condition, most of the parent OCS molecules absorb a single photon. Among the

molecules intercepted by the dissociation laser, the percentage of molecules dissociated can be determined by the following Equation:

$$P_{dissociation} = 1 - e^{-\sigma\eta} \quad (2.1)$$

where σ is the absorption cross section of OCS molecules at a given wavelength, and η is the photon density in unit area. The photon density varies with respect to laser beam diameter. When focused down, a Gaussian beam will have a minimum focal spot diameter:

$$w_f = \frac{0.89f\lambda}{D} \quad (2.2)$$

where w_f is the focal spot radius, f is the focal length, λ is the laser wavelength, and D is the lens diameter.[72] With this equation, the photon density at the focal spot can be determined and the dissociation percentage can be estimated. Focused down by a 1" diameter lens with a focal length of 30 cm, both 214 nm and 230 nm laser with 0.5 mj/pulse of power will be able to dissociate more than 90% of the molecules at the focal spot.

The photofragments from the dissociation will have a wide quantum state distribution. Specific quantum states selection and ionization can be achieved simultaneously via 2+1 REMPI. There are three types of 2+1 REMPI utilized in this work, probing ^{1}D state S (around 291.18 nm) and probing X $^1\Sigma^+$ state CO via two different intermediate resonant states (E-X transition around 215 nm and B-X transition around 230 nm). The first step of REMPI is a two-photon resonant transition exciting the photofragment ^{1}D state S or ($^1\Sigma^+$, v, j) state CO to an intermediate state ($^3P_1$ state for S, E state or B state for CO). Then, the last photon will be absorbed non-resonantly to excite the molecule above the ionization threshold and the molecules become cations.

In this work, the three photons in a 2+1 REMPI will be at the same wavelength. An example of CO E-X REMPI scheme can be found on Figure 2.5.

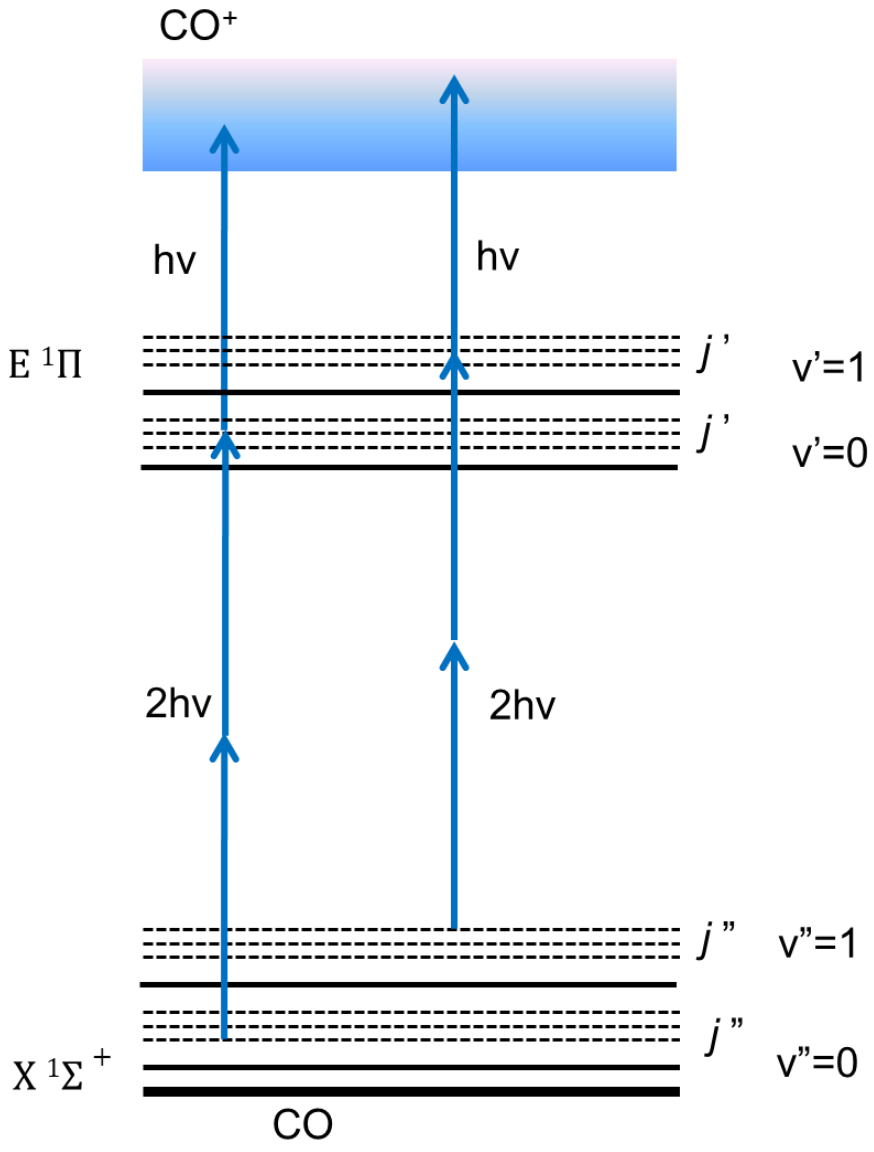

Figure 2.5: CO E-X REMPI scheme. Energy levels are not to scale.

The ionization yield will be wavelength dependent, and the yield will be greatly enhanced when the wavelength of each photon matches with the two-photon resonant transition. The ionization yield is also highly laser power dependent and laser line-width dependent. For our experiments, a satisfying ionization yield requires typical laser power of >500 μj/pulse for 215 nm laser (0.002 nm line-width), >300 μj/pulse for 230 nm laser (0.002 nm line-width) and >1mj/pulse for 290 nm laser (0.01 nm line-width).

The Detection of Ions

The photofragments which are not ionized will eventually be removed from the main region by the vacuum system. The selected photofragment ions will immediately be accelerated down the time of flight tube toward the detector by the einzel lenses. The einzel lenses, shown in Figure 2.6, are a set of four positively charged stainless steel plates parallel to the detector plane, named Repeller, L1, L2 and L3 following the direction of molecular beam.[73] The voltage of the lenses will vary depending on the experimental conditions. There are three main purposes for employing the einzel lenses. Firstly, with a proper voltage, the einzel lenses will be able to focus the ions to the detector so that when hitting the detector, the ions of the same displacement from the center will have the same x-y (detector plane) velocity, regardless of the initial position of the ions in the molecular beam.[28]

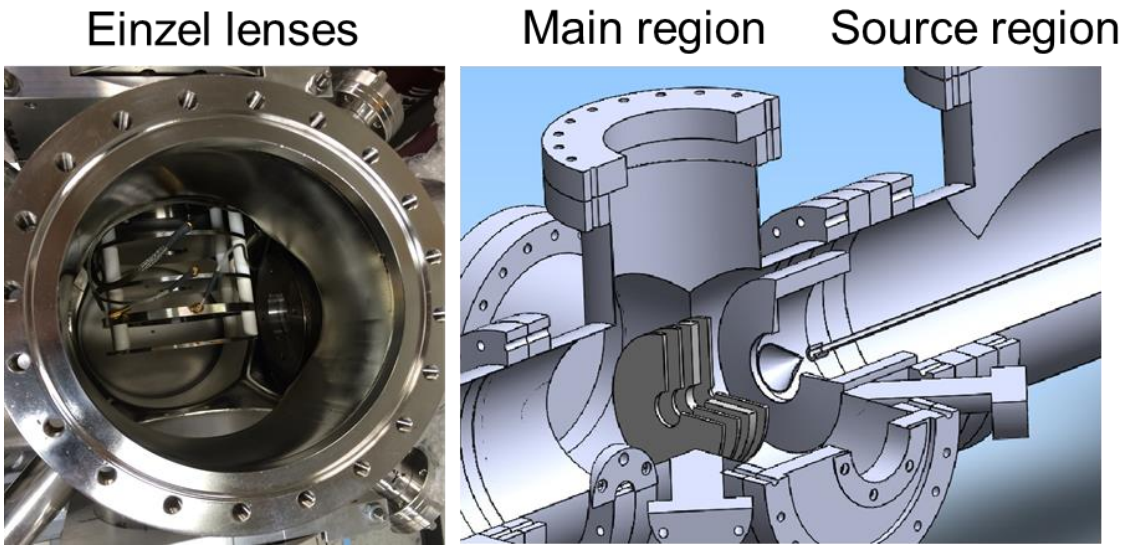

Figure 2.6: Einzel lenses in the main region.

Secondly, einzel lenses are an essential part of the time-of-flight mass selection. The flight time of ions through the time-of-flight tube, from the moment of ionization to the moment of hitting the detector, is determined by

$$t \propto \sqrt{m/(qV_R)} \tag{2.3}$$

where t is the flight time of ions of a given mass-to-charge ratio, m is the mass of the ion, q is the charge of the ion, and V_R is the voltage of the Repeller.[74] As the equation shows, for ions of a given mass-to-charge ratio, the flight time will only be affected by the Repeller voltage.

It is difficult and inconvenient to precisely measure the flight distance of ions and other details of time-of-flight tube. Alternatively, calibrations can be conducted to determine the quantitative relation between t and m. The calibration is usually conducted by using the VMI apparatus to measure the full mass spectrum of ions from residual hydrocarbon molecules in the VMI main chamber. The hydrocarbon residuals

(primarily pump oil) in the main chamber can be dissociated and ionized by the 214 nm laser. This process will produce a complete set of ions with mass-to-charge of 12, 24, 36 etc. They are usually considered as background noise in an experiment, but can be used as a calibration of the time-of-flight mass spectrum. The flight time t of each major mass signal from the mass spectrum is recorded and assigned to a mass-to-charge ratio. Their correlation is shown in Figure 2.7. A clear linear correlation between flight time and square root of mass is presented and serve as time-of-flight mass spectrum calibration curves. The calibration coefficient is Repeller voltage dependent and needs to be recalibrated at different voltage. The non-zero offset is a result of the non-zero time duration, include phosphor screen respond time, signal transmit and processing time, etc. which all happen after the event of photodissociation.

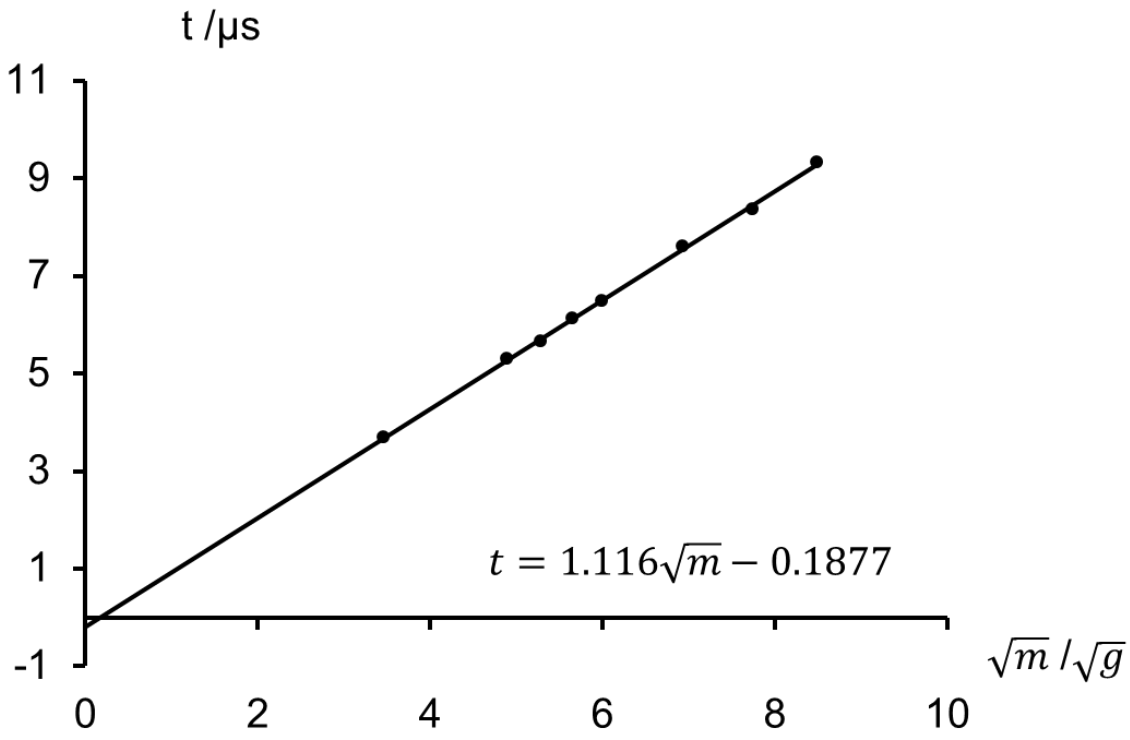

Figure 2.7: The correlation between mass and flight time, with a Repeller voltage of 4000V.

The final purpose of the einzel lenses is to “compress” or “stretch” the temporal profile of the ion clouds flying toward the detector. In our experiments, we either collect “crushed” or “sliced” signal of the ion clouds. If we collect the ion signals from the whole ion cloud, we utilize two einzel lenses to “crush” the temporal profile of the ion cloud to a very narrow time period (much smaller than the 100 ns detector time gate) and the whole ion cloud will hit the detector almost “simultaneously”. These “crushed” images will generally have better spatial resolutions for translational energy extraction purpose. However, the “crushed” process converts the three-dimensional ion cloud to a two-dimensional image. In order to obtain the velocity distribution and angular distribution of

the true ion cloud, mathematical treatments are required to reconstruct the three-dimensional ion cloud information from the two-dimensional image. Such mathematical treatments require the ion clouds to preserve cylindrically symmetry with respect to x axis vertical in the image plane. Such requirements will not be fulfilled when one of the laser polarizations is perpendicular to the imaging plane (z axis).[72] In some situations, it is more beneficial to collect only the center finite slice of the ion cloud (DC-slicing).[73] The DC sliced imaging method utilizes all four einzel lenses to stretch the temporal profile of the ion cloud. In our experiments the typical time width of the ion cloud is 200 ns. With a 40ns detector time gate, the center slices of 3-D ion clouds can be directly collected. Compared to the traditional non-sliced imaging method, the experimental requirements are more critical and the spatial resolution will be lower. However, there are two major benefits of slicing conditions. DC-sliced imaging allows for the direct measurement of image anisotropy information, without requiring cylindrical symmetry of the ion clouds. This way, the polarization of the lasers does not have to be vertical. Besides, when the ion cloud possesses multiple speed components (multiple rings), reconstruction of crushed images will be more likely to introduce errors. In this case, DC-slicing is more reliable, especially when collecting speed-dependent image anisotropy information. In this work, crushed and DC-sliced imaging methods are utilized for different purposes.

The REMPI Signal Accumulation and Spectrum Simulation

As discussed earlier, photofragments are probed state-selectively by the REMPI. The total ion signal of a selected mass generated by the REMPI is a function of

the probe laser wavelength. By scanning the probe laser wavelength and collecting the total signal of the ion cloud, a REMPI spectrum can be obtained.

For more technical details, the total signal of the ion cloud here is a measurement of the instant glow on the phosphor screen caused by crushed ion cloud hitting the detector. The glow signal is collected by the photomultiplier tube (PMT), with a 600 V-1000 V working voltage, and converted into an instant voltage signal. The output signal is time gated by a Boxcar averager to select only the signal arising from the mass of interest and is converted to an analog signal, which is then sent to a Data acquisition (DAQ) device (National Instruments) and send to the computer for signal processing.

The three probe laser systems each have a different way of scan control and signal processing. The LAS dye laser system, which generates 230 nm, has its own signal process system which only requires synchronization trigger and PMT signal input. The scan operation and resulting REMPI spectrum can be accessed by the program Wavescan.exe (Sirah/Lasertechnik, Inc.). The Scanmate dye laser, which generates the 215 nm laser, is controlled by the program Scanmate.exe (Lambda Physik, Inc.). This program, however, does not include a REMPI spectrum function. It only provides an output analog voltage signal (0-10 V) indicating the current wavelength while scanning. The relation between the voltage signal and current wavelength is given by

$$U = \frac{\lambda_c - \lambda_s}{\lambda_e - \lambda_s} \times 10\ V \tag{2.4}$$

where λ_s, λ_c and λ_e are the starting, current and stopping wavelengths (fundamental, not frequency doubled) of the scan. The REMPI spectrum is collected with a home-made program written in Labview language (National Instruments). This program reads the

output wavelength analog signal from Scanmate dye laser and the ion cloud signal from the Boxcar averager via the DAQ device mentioned before. Usually, the scan is conducted over a range of 0.2 nm (fundamental) and the stepwise wavelength is 0.002 nm (fundamental), so the voltage change for each wavelength step is 0.1 V. At each step, the laser will fire for 3 seconds with a rate of 10 Hz. The program is designed to first record the raw wavelength analog input signals and Boxcar averaged ion cloud intensity signal at each laser shot. Then it will process the signal by identifying the wavelength at each voltage, and for each wavelength, the signal from the first 30 laser shots is averaged to give a single intensity data point. The new wavelength-intensity plot is recorded as the REMPI spectrum. An example of raw and processed CO E-X REMPI spectra is shown in Figure 2.8.

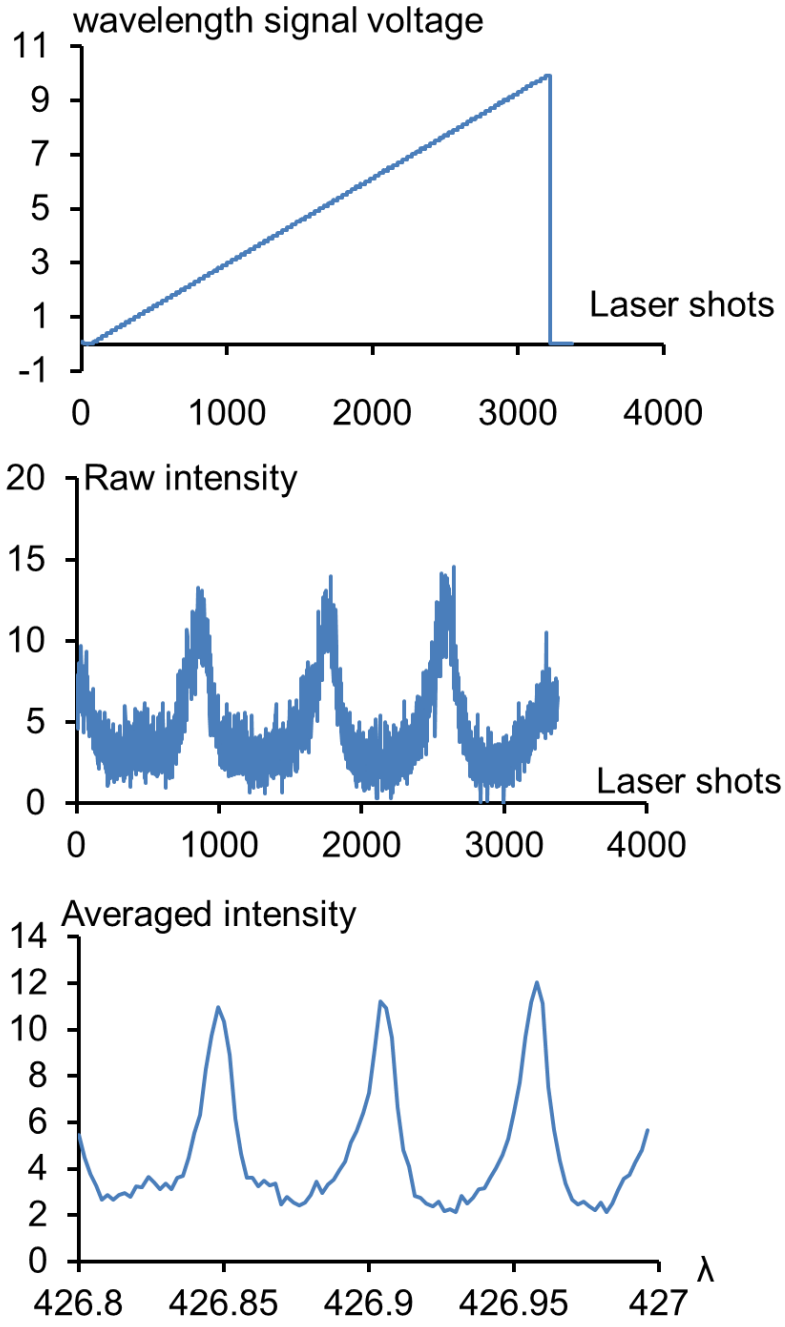

Figure 2.8: CO E-X REMPI spectrum. The top panel is the change of voltage signal of wavelength over laser shots; the middle panel is the raw signal intensity over laser shots; the bottom panel is the REMPI spectrum after ion signal averaging and wavelength signal conversion.

The wavelength scanning function of the PDL dye laser (291 nm laser) is achieved by a PC controlled stepper motor which is connected to the dye laser grating. The REMPI spectrum collection program is adapted from a home-made control program written by former student Dr. Michael Grubb with Labview language. The scan REMPI program simply scans the stepper motor one step at a time, and collects the Boxcar averaged ion cloud intensity signal. A diagram of ion cloud intensity as a function of stepper motor steps is recorded as the raw REMPI spectrum. The step number is linearly correlated with the wavelength of the laser and can be converted to wavelength by Dr. Grubb's program.[75,76] Since the primary objective of scanning the PDL laser is to find the REMPI wavelength of a single transition (S $^3P_1$-$^1D_2$) and fix the wavelength at that transition, the scanning program for this PDL laser is not programed to convert stepper motor steps to wavelength.

The CO REMPI spectrum can also be simulated and fit to the experimental spectrum. Each REMPI peak is simulated with a Gaussian function peaked at a calculated REMPI transition wavelength. The wavelength is calculated by the following equation:

$$\mathrm{E}_{h\nu} = [\mathrm{T}_{\mathrm{vv}} + \mathrm{B'}_{\mathrm{v}} j'(j'+1) - \mathrm{D'}_{\mathrm{v}} j'^2 (j'+1)^2\,] - [\mathrm{B"}_{\mathrm{v}} j"(j"+1) - \mathrm{D"}_{\mathrm{v}} j"^2 (j"+1)^2\,] \quad (2.5)$$

the T_{vv} , $\mathrm{B'}_{\mathrm{v}}$, $\mathrm{D'}_{\mathrm{v}}$, are the spectroscopic constants for CO molecules in a given electro-vibrational state, and j is the rotational state. The double prime denotes an electronic ground state and the single prime denotes an electronic excited state. The heights of the peaks are determined by two factors: transition probability and population of the initial state of the transition. The transition probability for different rotational ranches within the same electro-vibrational transition can be calculated by the two-photon line-strength factors[77].

The rotational population distributions vary depending on the system. For a thermalized system, like the cold CO molecular beam coming out of the pulsed valve, the population distribution can be determined by the Boltzmann distribution:

$$I = N_0(2j+1)e^{-\mathrm{B_e}j(j+1)hc/k_BT} \tag{2.6}$$

where N_0 is the population of the rotational ground state, B_e is the rotational constant, h is the Planck constant, c is the speed of light, k_B is the Boltzmann constant.[78]

Figure 2.9 is the Boltzmann plot of the populations derived from the REMPI spectrum of CO beam. From the slope of the plot, the rotational temperature of the CO beam is determined to be 22±3 K.

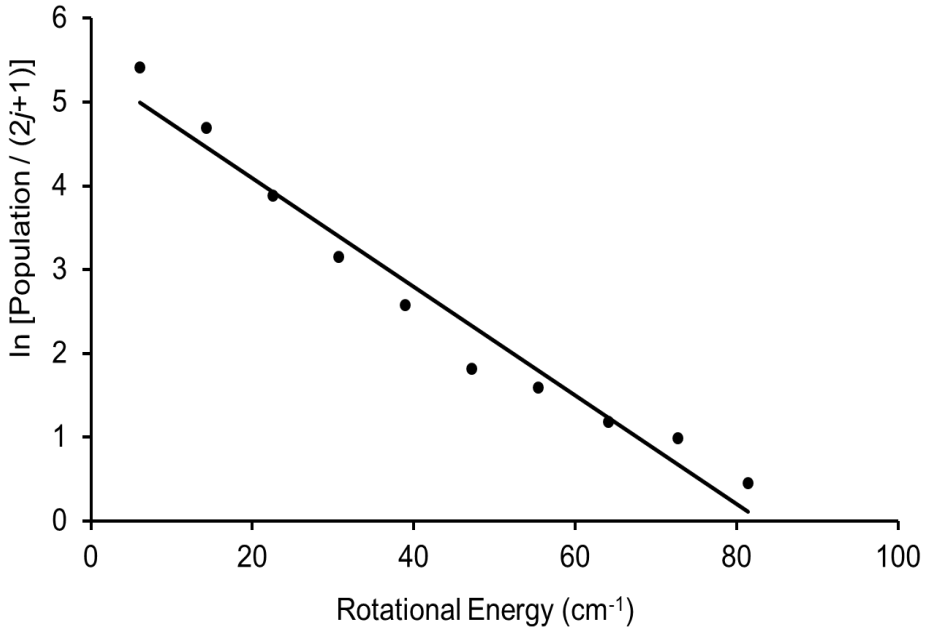

Figure 2.9: Rotational population derived from the CO E-X (0-0) REMPI. The solid line represents the best fit to a Boltzmann distribution

The transition probability of two-photon absorption is given by Bray and Hochstrasser.[77] For our case of CO E-X transition, the transition probability of each rotational branch is given as:

$$O: \frac{(J-1)(J-2)J^2}{15J(J-1)(2J-1)} \tag{2.7}$$

$$P: \frac{J(J+1)^3}{30J(J-1)(J+1)} \tag{2.8}$$

$$Q: \frac{J(J+1)(2J+1)}{10J(J+1)(2J-1)(2J+3)} \tag{2.9}$$

$$R: \frac{(J+1)(J+2)J^2}{30J(J+1)(J+2)} \tag{2.10}$$

$$O: \frac{(J+2)(J+3)(J+1)^2}{15(J+1)(J+2)(2J+3)} \tag{2.11}$$

With the wavelength and the peak intensities determined, the simulated peaks are summed up to form a simulated spectrum.

The Image Accumulation and Processing

Image capturing and processing are achieved using a program developed by Dr. Grubb[75]. Each snapshot captured by the camera is represented as a two dimensional array of intensities data. The resolution of each snapshot is 768 by 768 pixels, and the 2D-array is composed of 589,824 pixels, with each pixel representing about 70 μm in size, which is smaller than the glow produced by a single event on the phosphor screen. A “centroiding” process is included in the image accumulation process to determine the true ion position by weighing the intensity of the pixels in each glow spot. Then each snapshot captured by the camera is converted to a binary image, in which each pixel associated with the center of ion hitting location is counted as one hit, and all other

pixels are counted 0. The binary images are summed up to form a 768 by 768 unsigned 8-bit (0 to 255 for intensity of each pixel) accumulated image (raw image). Since the centroiding process is involved, sometimes when multiple ions hit the detector simultaneously, the centroiding algorithm will treat the centroid of a multi-ion event as the center of a single hit, instead of identifying the centers of each single ion event. In this case, the accumulated image will start to show unreasonable pattern, like the image on the right of Figure 2.10. In such situation, we usually slightly detune the laser to decrease the amount of ions generated, avoiding the centroiding error.

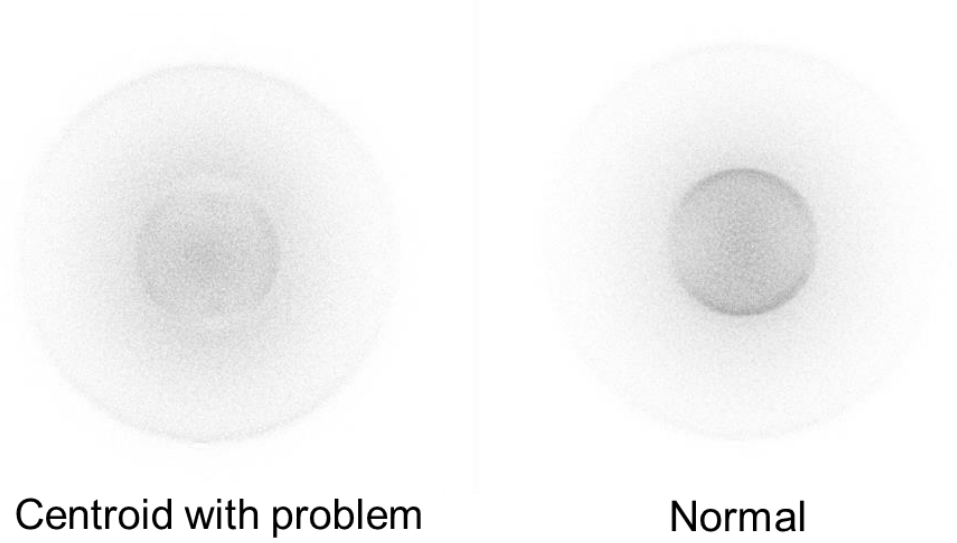

Figure 2.10: Problems introduced by centroid function when taking images. The left figure is a result of centroiding errors due to too many ions hitting the detector simultaneously. The real ion image should look like the one on the right.

In order to perform analysis on the raw images, the center or the image needs to be determined. Additionally, in many situations, the four quadrants of the experimental

images are not symmetrical due to presence of defects on the detector or other issues. Both of these issues can be resolved by four-fold symmetrization of the image. Vertical and horizontal mirror reflection operations are performed on the raw image, with the position of the vertical and horizontal mirror planes determined by the manually inputted center coordinates x_{center}, y_{center}, respectively. The original raw image will be merged with the three mirror images. The guessed image center coordinates values can then be adjusted until the reflections overlap each other precisely, as the two mirrors passing the real center of the raw image will generate reflections that overlap with the original image. In this way, both the image center and the symmetrized image can be obtained. An example of symmetrization can be found in Figure 2.11. The raw image shows some asymmetry and can be symmetrized.

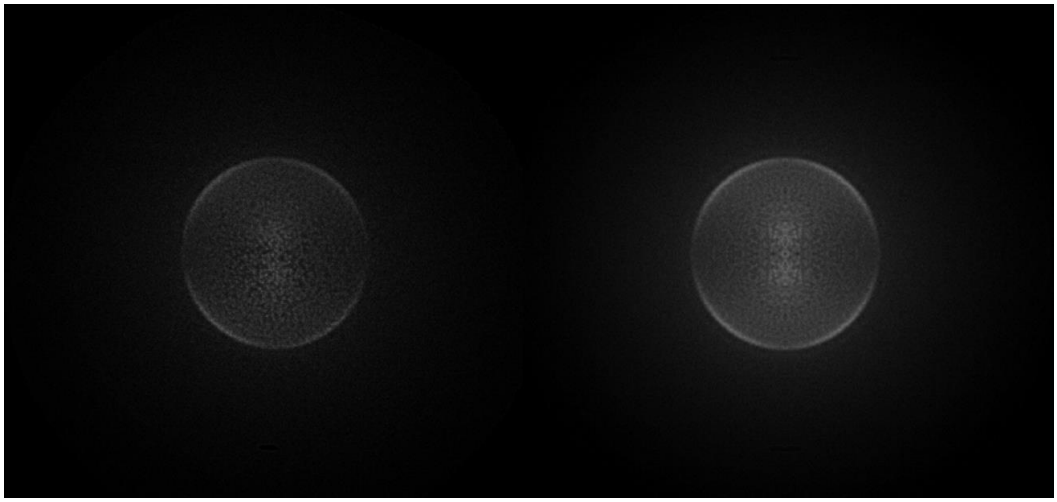

Figure 2.11: Example of the symmetrization. The image on the left is the raw image while the image on the right is the symmetrized image.

The primary source of noise in the images is ions generated by the ionization of hydrocarbons from pump oil. These ions are pulse valve independent and will have broad speed distributions and isotropic angular distributions, like the image shown on the top panel of Figure 2.12. (The trace of rings in this background image is a result of a not completely off-resonance probe laser.) The middle panel demonstrates an image symmetrized without any treatment on background noise. The noise ions will have two impacts on the experimental results: lowering the resolution of the product speed distributions and lower the observed anisotropy of angular distributions. The impacts on the angular distribution are especially significant since the measurements of all of the vector properties rely on the precise measurements of angular distribution, and the background noise is isotropic. When the number of ions coming from photochemical process of interest is low compared to the number of noise ions, the anisotropy of the whole image will be washed out.

In such cases, it is necessary to collect background noise ion images and make background subtractions. If the signal of interest is generated by REMPI, the background image should be collected with the probe laser tuned off-resonance. If the signal of interest is two-laser dependent, and one of the laser also generates ions signal not of interest, the background image should be collected with these signals. The background ion signals can be subtracted from the image of interest by utilizing the ImageJ program.[79] Before subtraction, the background image should be intensity scaled to match the intensity of the image of interest. The scaling is not critical because, using the image subtraction algorithm in ImageJ, if certain pixels on the background image have higher intensity compared to the same ones on the image of interest, the resulting

intensities of these pixels will be 0 instead of negative values. The bottom panel of Figure 2.12 shows the resulting image from the background subtraction.

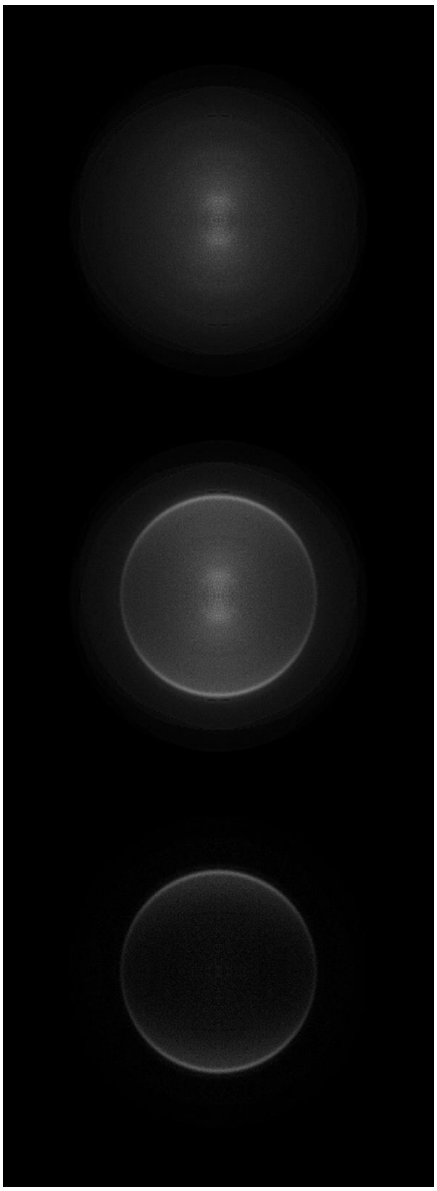

Figure 2.12: Example of the background image subtraction. The top panel shows the image of background ions; the middle panel shows an image of interest without background subtraction; the lower panel shows the image after background subtraction.

Analysis of Images

The symmetrized images are 768 by 768 pixels with Cartesian coordinates x, y. The images will be converted to polar coordinates (r, θ) with the radial coordinate r (in pixels) as the distance from the center of image and the angular coordinate θ as the angle away from the x axis of image plane (also called image angle). These polar coordinates are more applicable for further analysis and are physically more meaningful because the value of r is related to the speed of the detected photofragments and the θ is related to the direction of recoil photofragments. The relation between Cartesian coordinates and polar coordinates is given below:

$$r = \sqrt{(x - x_{center})^2 + (y - y_{center})^2} \tag{2.12}$$

$$\theta = \arctan(\frac{x - x_{center}}{y - y_{center}}) \tag{2.13}$$

where x_{certer} and y_{center} are the Cartesian coordinates of the center of images. The intensity distributions $I(r, \theta)$ obtained by this method still do not represent the true intensity distribution of the photofragment ions yet because it is either only the projection of a three-dimensional distribution projected to a two-dimensional detector plane (crushed images), or a finite (but not perfect) slice of the ion cloud (DC-sliced images). Different algorithms are required to reveal the true intensity distribution of the photofragment ions, depending on whether the images are crushed or DC-sliced images.

For crushed images, the Polar Onion Peeling method can be applied to reveal the three-dimensional distribution from the crushed images if the ion clouds preserve cylindrical symmetry along the x axis of the detector plane.[26] Such prerequisites are usually fulfilled if both the dissociation and the probe lasers are linearly polarized vertically (VV geometry, along the x axis of image plane). The processing of crushed

images in this work utilizes the POP module in the home-made Labview based program by Dr. Grubb[75], adapted from the work of Roberts *et al*.[26] . The algorithm assumes the outer edge of the images to be equivalent to the true two-dimensional center slice of the ion cloud. Since the ion cloud is cylindrically symmetric, the three-dimensional intensity distribution of the outer edge shell can be reconstructed. Then this outer shell can be "peeled away" from the crushed image. This same process of reconstruction based on cylindrical symmetry is repeated until all the layers are "peeled away". The intensity distributions $I(r,\theta)$ obtained by this reconstruction now represent the entire two-dimensional intensity distribution of the photofragment ions $I(r,\theta)$. The true three-dimensional radial (pixel) distribution can be obtained by:

$$I(r) = \int I(r,\theta) \cdot r \, d\theta \tag{2.14}$$

where the r factor is included because on each radial shell, the true distribution should represent a two-dimensional shell instead of a one-dimensional circumference.

For the DC sliced images, the slicing time width can sometimes be not small enough compared to the ion cloud time width. In such a case, the population of the ions with small velocity from the wide-sliced images can potentially be altered. DC sliced images were treated using the finite slice algorithm described by Komissarov *et al.* to obtain the true speed distributions.[80]

Sometimes if no background images are taken and no background subtraction can be made directly on the raw images, corrections can be made directly to the radial distribution. The radial/ speed distribution can be treated with a polynomial simulation to fit the baseline of the distribution. The simulated intensity baseline is then subtracted from the original distribution.

From the obtained radial distribution, a lot of information of photodissociation dynamics can be revealed. Certain calibration methods can be implemented to determine the speed to pixel ratio of the photofragment. The speed distribution can also be converted to fragment translational energy distributions. Since the total energy of the photodissociation process is conserved and the internal energy of the detected photofragment is known and the translational energy is correlated to the internal energy of the co-fragment, the internal energy distributions of the co-fragments can be obtained with certain transformation methods. These energy distributions can be utilized to test the existing theories of photodissociation dynamics.

Photofragment angular distributions can also be obtained from analysis of the images. The anisotropy of the images is the result of both the correlations of the three vectors (transition dipole moments $\boldsymbol{\mu}_{\mathbf{par}}$, photofragment recoil velocity vector **v** and photofragment angular moment vector ***j***) and the detection laser polarization. Or it can arise as the result of an anisotropic spatial velocity distribution of the photofragments with respect to the dissociation laser and the detection sensitivity differences of photofragments with different rotational angular momentum directions.

The orientations of the parent molecules are evenly distributed. However, when through the use of linearly polarized lasers, a laboratory frame can be established. In order to absorb a photon and evolve to a product channel, the transition dipole moment of the parent molecule $\boldsymbol{\mu}_{\mathbf{par}}$ needs to interact with the electronic vector $\boldsymbol{E_d}$ of the dissociation laser. The transition probability of the parent molecule is proportional to the square of the modulus of the dot product of $\boldsymbol{E_d}$ and $\boldsymbol{\mu}_{\mathbf{par}}$, i.e. the projection of $\boldsymbol{E_d}$ onto $\boldsymbol{\mu}_{\mathbf{par}}$

$$I = |E_d \cdot \mu|^2 = |E_d|^2 |\mu|^2 cos^2\theta_{E_d\mu} \tag{2.15}$$

where the $\theta_{E_d\mu}$here is the angle between $\boldsymbol{E_d}$ and $\boldsymbol{\mu_{par}}$. This means that a laboratory frame absolute directional preference is established and those parent molecules whose $\boldsymbol{\mu_{par}}$ are aligned parallel to this laser $\boldsymbol{E_d}$ will be most likely to dissociate; while those parent molecules whose $\boldsymbol{\mu_{par}}$ are perpendicular to $\boldsymbol{E_d}$ will be least likely to dissociate. The general trend can be described with a $cos^2\theta_{E_d\mu}$ distribution.[31, 81]

When state selectively detecting the photofragments, the photofragments resonantly absorb two photons (the general case in this work) and are then ionized by non-resonantly absorbing a third photon. The resonant step also requires interaction between the electronic vector of the probe laser $\boldsymbol{E_p}$ and transition dipole moment of the selected photofragment $\boldsymbol{\mu_{frag}}$. Since the $\boldsymbol{\mu_{frag}}$ is dominated by the rotational angular momentum ***j***, the probe laser $\boldsymbol{E_p}$ can establish an orientational preference for the ***j*** of the photofragments. Each probe laser photon absorbed by the selected photofragment will introduce a $cos^2\theta_{E_pj}$ distribution. So in this work, signal angular distribution can be up to $cos^6\theta$ dependent.[64]

Angular distributions can be extracted from sliced images by integrating the intensity over a narrow radial range. In case of a crushed image with a single component, the integration should be over a narrow radial range (7-10 pixels) around the outer edge of each crushed image. When the measured images consist of a single speed component, the signal at the maximum ion cloud radius is equivalent to the angular distribution that would be obtained from sliced imaging.[82, 83]

The angular distributions derived from ion images can be expressed as a weighted sum of Legendre polynomials, $P_k(x)$:

$$I^{FG}(\theta) = 1 + \beta_2^{FG}P_2(\cos\theta) + \beta_4^{FG}P_4(\cos\theta) + \beta_6^{FG}P_6(\cos\theta) \qquad (2.16)$$

where the β_k^{FG} are called image anisotropy parameters; *F* and *G* are the lab frame pump and probe polarizations respectively, each of which in these experiments is polarized either parallel (F/G written as V) or perpendicular to the imaging plane (F/G written as H). k is an even number in case of linearly polarized light. For a certain FG laser polarization geometry, the upper limit of the k value will be 2(m+n), where m is the number of vertically polarized photons involved in the dissociation process and n is the number of vertically polarized photons involved in the resonance step of the REMPI process. Here m=1 if the dissociation laser is vertically polarized and m=0 if horizontally polarized. In the 2+1 REMPI case, n=2 if the probe laser is vertically polarized and n=0 if horizontally polarized. Therefore, up to 6th order polynomials are required; in the semi-classical limit, orders higher than six may be neglected for a two photon process.[64] The derived image anisotropy parameters β_k^{FG} are the key experimental parameters which encrypt vector correlation information.

The experimental angular distribution can be fit with Equation (2.16) to obtain the image anisotropy parameters β_k^{FG}. Genplot, a graphical data analysis and plotting program, is employed to conduct least squares regression fits to the experimental angular distributions.[84] The resulting image anisotropy parameters β_k^{FG}, can be used to calculate vector correlation information with the equations derived in the next chapter.

CHAPTER III

THE METHOD OF EXTRACTING VECTOR CORRELATIONS FROM 2+1 REMPI ION IMAGES*

The anisotropy of the collected ion image is the product of the spatial distribution of photofragments (dependent on the relative photodissociation laser polarization) along with their angular sensitivity to detection (dependent primarily on the probe laser polarization). The values of image anisotropy parameters β_k^{FG} are affected by two factors: detection laser polarization (detection geometry VV, VH or HV) and photofragment vector correlations. In order to extract the bipolar moments, a set of equations (2+1 REMPI Equations) expressing image anisotropy parameters β_k^{FG} as functions of bipolar moments for images detected with 2+1 REMPI are needed, one for each of the β_k^{FG} parameters given by the three laser detection geometries. These equations also include parameters which specify detection branch information.

There are a number of previously published analysis methods for extracting vector correlations from experimental ion imaging data. Previously, Grubb *et al.* reported a method for extracting speed-dependent bipolar moments from images obtained using 1+1 REMPI detection.[82, 83] This method is mathematically convenient and can be used to analytically determine bipolar moments values from sliced image anisotropy parameters. However, this method was designed to be applied to images

* Part of this chapter is reprinted from "W. Wei, C. J. Wallace, M. P. Grubb and S. W. North, The Journal of Chemical Physics 147 (1), 013947 (2017)", with the permission of AIP Publishing.

collected with 1+m REMPI detection, while the majority of ion imaging studies employ 2+1 REMPI detection. Bañares *et al.* have shown that 2+1 REMPI image anisotropy parameters can be analyzed using the 1+1 REMPI Equations of Grubb *et al*., in the cases where the high order anisotropy parameters are negligible. [85-87] However, this is not a general result and its applicability is limited. In most cases, different equations are necessary for the analysis of images from 2+1 REMPI detection. An extension of the work of Grubb *et al.* has been developed to treat images collected with 2+1 REMPI detection which links semi-classical bipolar moments and experimental angular distributions from either sliced or reconstructed non-sliced images.

Derivations of the Working Equations

The derivation of the 2+1 REMPI Equations here follows a similar approach as described in Grubb *et al*. [82, 83]

$$\beta_k^{FG} = \int_0^{\pi} I[\Theta,\ \Phi,\ \theta_\varepsilon,\ \beta, a_q^{(k)}(p)] P_k(\cos\theta)\frac{2k+1}{2} sin\theta d\theta \qquad (3.1)$$

where θ is the lab frame image angle between fragment velocity and the x axis of image (origin of image angle). $I\left[\Theta,\ \Phi,\ \theta_\varepsilon,\ \beta,\ a_q^{(k)}(p)\right]$ is a function describing the photofragment detection probability in the molecular frame.[35, 36, 60] We have adapted Equation (16) from Rakitzis *et al.*[35] to include k=4 terms which emerge from 2+1 detection, shown below as Equation (3.2). In this equation, the interference terms have been omitted due to the fact that they go to 0 in the high-*j* semi-classical approximation.

$$I\left[\Theta,\ \Phi,\ \theta_\varepsilon,\ \beta, a_q^{(k)}(p)\right] = 1 + \beta P_2(\cos\theta_\varepsilon) + s_2\left\{(1+\beta)\ cos^2\theta_\varepsilon\ a_0^{(2)}(\|)\ P_2(\cos\Theta) + \right.$$

$$\left.\left(1-\frac{\beta}{2}\right)\ sin^2\theta_\varepsilon\ a_0^{(2)}(\perp)\ P_2(\cos\Theta) + (1-\beta/2)\ sin^2\theta_\varepsilon\ a_2^{(2)}(\perp)\ \sqrt{3/2}\ sin^2\Theta\cos(2\Phi)\right\} +$$

$$s_4\left\{(1+\beta)\,cos^2\theta_\varepsilon\,a_0^{(4)}(\|)\,P_4(\cos\Theta)+(1-\beta/2)\,sin^2\theta_\varepsilon\,a_0^{(4)}(\perp)\,P_4(\cos\Theta)+(1-\right.$$

$$\left.\beta/2)\,sin^2\theta_\varepsilon\,a_2^{(4)}(\perp)\,\sqrt{5/8}\,sin^2\Theta\,(7\,cos^2\Theta-1)\cos(2\Phi)\right\} \quad (3.2)$$

where Θ is the angle between the recoil velocity vector of the photofragment **v** and the probe laser polarization vector ***P***, θ_ε is the angle between **v** and the dissociation laser polarization vector ***E***, Φ is the azimuthal angle between ***P*** and ***E*** about **v**, β is spatial anisotropy parameter and $a_q^{(k)}(p)$ are a set of Rakitzis's molecular frame polarization parameters [35] In the case of sliced images with linearly polarized dissociation and probe lasers, the θ_ε and Θ angles either become image angle θ if the respective lasers are polarized parallel to x axis in the imaging plane or become π/2 if the respective lasers are polarized perpendicular to imaging plane. Angle Φ is 0 if the dissociation and probe lasers are polarized parallel or π/2 if the two lasers are perpendicular to each other.[82, 83]

This function also contains detection sensitivity factors, s_k, which are related to detection sensitivity for different rotational branches. The values are specified in Table 1 from published work by Rakitzis and Alexander.[36] These detection sensitivity factors were referred to as alignment sensitivity coefficients in Grubb *et al*.[82, 83] At high *j*, the O/S-branch s_2 and s_4 factors approach the limiting values of -5/7 and 3/7 respectively, while the P/R-branch s_2 and s_4 factors approach 5/14 and -12/7 respectively. The Q-branch is special in 2+1 REMPI because the resonant step can consist of either two parallel transitions (Δ*j*=0) or two perpendicular transitions (Δ*j*=+1 and -1). In reality the resonant step will be a combination of the two situations.

The Q-branch s_2 and s_4 factors must be determined for each molecular system calculated from Equation (19) of Rakitzis *et al*.[36]

$$s_k = P_k\frac{[J(J+1)]^{k/2}\sqrt{2k+1}\sqrt{2J+1}}{c(k)<J||J^{(k)}||J>} \quad (3.3)$$

in which the c(k) can be found from Equation (28) of Orr-Ewing and Zare,[38] and $< J||J^{(k)}||J >$ is the reduced matrix element.[30] The P_k values in Q-branch need to be determined with the knowledge of the ratio between parallel and perpendicular component of transitions to the intermediate virtual state for Q-branch transition. An example of determining the P_k values can be found in work of Mo *et al.* [88, 89]

A set of equations (bridging equations) are used to substitute Rakitzis's molecular frame polarization parameter $a_q^{(k)}(p)$ with bipolar moments in the photofragment detection probability function. For low order parameters, ($a_0^{(2)}(\parallel)$, $a_0^{(2)}(\perp)$, $a_2^{(2)}(\perp)$), Equations 7(a-e) from Rakitzis *et al.* are used.[90] For higher order parameters ($a_0^{(4)}(\parallel)$, $a_0^{(4)}(\perp)$, $a_2^{(4)}(\perp)$), Equations (2)-(5) from Denzer *et al*. [91] can bridge high order polarization parameter and bipolar moments. However, after we apply Equations (2)-(5), we found that the results are not physically reasonable for test cases which will be discussed later. Consequently, we derived our own bridging equations for high order polarization parameters $a_q^{(k)}(p)$. These new bridging equations are similar in format to the equations given by Denzer *et al.* but with subtle differences, and they provide results that are more physically reasonable in selected test cases. The derivation procedure is shown below.

The derivation of the bridging equations linking the high order terms of Rakitzis's molecular frame polarization parameter, $a_q^{(4)}(p)$, and Dixon's bipolar moments generally follows work by Rakitzis *et al.*,[90] which is to use polarization parameters $a_q^{(k)}(p)$ to describe the experimental Doppler profile.

The equation we used describing photofragment detection probability in the molecular frame has been shown earlier as Equation (3.2). The terms in this equation

have also been defined earlier. The angles in this equation are molecular frame angles, which need to be converted to lab-frame Doppler detection angles Γ, Δ, and Φ here with same equations used in Rakitzis *et al.*[90]

$$\cos\theta_\varepsilon = \cos\gamma\cos\Gamma + \sin\gamma\sin\Gamma\cos\chi \tag{3.4}$$

$$\cos\Theta = \cos\gamma\cos\Delta + \sin\gamma\sin\Delta\cos(\Phi - \chi) \tag{3.5}$$

$$\cos\Phi = \{\sin^2\gamma\cos\Gamma\cos\Delta + \sin\Gamma\sin\Delta\cos\Phi - \sin\gamma\cos\gamma\,[\sin\Delta\cos\Gamma\cos(\Phi-\chi) + \sin\Gamma\cos\Delta\cos\chi] - \sin^2\gamma\sin\Gamma\sin\Delta\cos(\Phi-\chi)\cos\chi\}/(\sin\theta_\varepsilon\sin\Theta) \tag{3.6}$$

where Γ is the angle between dissociation laser polarization and detection axis, Δ is the angle between probe laser polarization and detection axis (usually Δ = π/2), Φ is the azimuthal angle between the projection of dissociation and probe laser polarization on to the plane perpendicular to the detection axis, χ is the azimuthal angle that describes all the photofragments that have the same Doppler shift, ranging from 0 to 2π, γ is the angle between photofragment recoil velocity and detection axis, and $\cos\gamma$ is equivalent to the Doppler shift x_D. The definitions of these angles are same as Rakitzis *et al.*, except that we used Φ to represent Φ in his paper because of a symbol conflict. The Doppler profile can be described by:

$$I_{lab} = \frac{1}{2\pi}\int_0^{2\pi} I[\Gamma, \Delta, \Phi, \beta, \chi, a_q^{(k)}(p), \mathrm{x_D}]d\chi \tag{3.7}$$

The resulting equation is equivalent to another well-known equation describing fluorescence intensity as a function of Doppler shift x_D with bipolar moments formalism, given by M. P. Docker.[64]

$$I_{(\mathrm{x_D})} = \mathrm{C}\sum g_j P_j(\mathrm{x_D}) \tag{3.8}$$

where $P_j(\mathrm{x_D})$ is Legendre polynomial and g_j is given as:

$$g_0 = 1 + b_1\beta_0^2(02) \tag{3.9}$$

$$g_2 = b_2\beta_0^2(20) + b_3\beta_0^0(22) + b_4\beta_0^2(22) + b_5\beta_0^2(24) \quad (3.10)$$

$$g_4 = b_6\beta_0^2(42) + b_7\beta_0^0(44) + b_8\beta_0^2(44) \quad (3.11)$$

$$g_6 = b_{10}\beta_0^2(64) \quad (3.12)$$

in two-photon resonant probe case.

The b_i coefficients contain functions of probe detection angles Γ, Φ and also contain detection sensitivity factors s_k. Here instead of expanding the whole equation out, we simply substitute the values of detection angles into Equation (3.7) before integration to significantly simplify the equations. We re-organized the resulting equation as $[\dots]P_j(\mathrm{x_D})$ terms. Meanwhile, we also only use b_i values from Table 3.1 to simplify Docker's Doppler profile function. By comparing terms which share same $P_j(\mathrm{x_D})$ between simplified Docker's functions and $[\dots]P_j(\mathrm{x_D})$ re-organized from integration, relations between $a_q^{(k)}(p)$, and Dixon's bipolar moments can be obtained. Some of the $[\dots]P_j(\mathrm{x_D})$ groups contain more than one $a_q^{(k)}(p)$ terms which cannot be directly related to bipolar moment terms. Three classic detection cases (A, B, D) are used to generate three functions with different detection angles substituted so that multiple $a_q^{(k)}(p)$ parameters can be determined in this case.

Table 3.1: The b_i coefficients, adjusted from Docker, Chem. Phys. 135 (3), 405 (1989).[64] The coefficients for detection sensitivity are not listed here.

Geometry	b_1	b_2	b_3	b_4	b_5	b_6	b_7	b_8	b_{10}
A	4/5	-1	-1	4/7	-2/7	27/35	3/8	-15/77	-25/88
B	-2/5	-1	-1	-8/7	1/14	9/35	3/8	30/77	-5/88
D	-2/5	2	-1	4/7	3/14	-36/35	3/8	-15/77	15/44

The bridging equations solved with this method contain detection sensitivity factors s_k. This is because we omit them when substituting b_i coefficients. These s_k factors were omitted to match the format as those low order bridging equations given by Rakitzis.

The resulting bridging equations are shown below:

$$a_0^{(4)}(\|) = \frac{1}{(1+\beta)}\left[\frac{18}{11}\beta_0^2(64) - \frac{4}{11}\beta_0^2(44) + \beta_0^0(44)\right] \tag{3.13}$$

$$a_0^{(4)}(\perp) = \frac{1}{(1-\beta/2)}\left[\frac{3}{11}\beta_0^2(64) + \frac{32}{77}\beta_0^2(44) - \frac{6}{7}\beta_0^2(24) + \beta_0^0(44)\right] \tag{3.14}$$

$$a_2^{(4)}(\perp) = \frac{\sqrt{10}}{(1-\beta/2)}\left[\frac{1}{2}\beta_0^2(64) + \frac{3}{14}\beta_0^2(44) - \frac{2}{7}\beta_0^2(24)\right] \tag{3.15}$$

By substituting the $a_q^{(k)}(p)$ expressions above into Equation (3.2) and integrating we obtain image anisotropies as functions of bipolar moments, detection laser geometries, and REMPI branches. The full equations are shown below:

$$\beta_2^{VV} = \frac{5\{[9800\,\beta_0^2(64)+2100\beta_0^2(44)-3080\,\beta_0^2(24)]s_4+[3168\,\beta_0^2(42)-7920\,\beta_0^2(22)-1848\,\beta_0^2(02)+16170\beta_0^0(22)]s_2+16170\beta_0^2(20)\}}{231\{[96\,\beta_0^2(42)+40\,\beta_0^2(22)+84\beta_0^2(02)]s_2+175\}} \tag{3.16}$$

$$\beta_4^{VV} = \frac{-[88200\,\beta_0^2(64)+95900\beta_0^2(44)-69300\,\beta_0^2(24)-148225\beta_0^0(44)]s_4-[-165528\,\beta_0^2(42)+58080\,\beta_0^2(22)-81312\beta_0^2(02)]s_2}{847\,\{[96\,\beta_0^2(42)+40\,\beta_0^2(22)+84\beta_0^2(02)]s_2+175\}} \tag{3.17}$$

$$\beta_6^{VV} = \frac{25\,[2590\,\beta_0^2(64)+60\beta_0^2(44)-220\,\beta_0^2(24)]s_4}{363\,\{[96\,\beta_0^2(42)+40\,\beta_0^2(22)+84\beta_0^2(02)]s_2+175\}} \tag{3.18}$$

$$\beta_2^{VH} = \frac{-10\,\{[455\,\beta_0^2(64)+510\beta_0^2(44)-638\,\beta_0^2(24)]s_4+[792\,\beta_0^2(42)-1056\beta_0^2(22)]s_2-1848\,\beta_0^2(20)\}}{[10220\,\beta_0^2(64)+3840\beta_0^2(44)-6380\,\beta_0^2(24)+3465\beta_0^0(44)]s_4+[-1584\,\beta_0^2(42)-5280\,\beta_0^2(22)-3696\,\beta_0^2(02)-9240\,\beta_0^0(22)]s_2+9240} \tag{3.19}$$

$$\beta_2^{HV} = \frac{5\{[35\,\beta_0^2(64)+15\beta_0^2(44)-20\,\beta_0^2(24)]s_4+[18\,\beta_0^2(42)-24\,\beta_0^2(22)-42\,\beta_0^0(22)]s_2\}}{[35\,\beta_0^2(64)+15\beta_0^2(44)-20\,\beta_0^2(24)]s_4+[18\,\beta_0^2(42)+60\,\beta_0^2(22)+42\,\beta_0^2(02)]s_2+105\beta_0^2(20)-105} \tag{3.20}$$

$$\beta_4^{HV} = \frac{-105\left[25\,\beta_0^2(64)+14\beta_0^2(44)-22\,\beta_0^2(24)+11\beta_0^0(44)\right]s_4}{11\{\left[35\,\beta_0^2(64)+15\beta_0^2(44)-20\,\beta_0^2(24)\right]s_4+[18\,\beta_0^2(42)+60\,\beta_0^2(22)+42\,\beta_0^2(02)]s_2+105\beta_0^2(20)-105\}} \quad (3.21)$$

Equations (3.16)-(3.21) are the central results of this chapter. They provide a connection between the bipolar moments and image anisotropy parameters β_k^{FG} which can be extracted from experimental images via Equation (2.16). We suggest two major applications of these new 2+1 REMPI Equations for extracting fragments bipolar moments: direct inversion and forward convolution. For direct inversion, the bipolar moments are numerically solved directly from the Equations (3.16)-(3.21) (2+1 REMPI detection equations). For forward convolution, a trial set of bipolar moments are used in Equation (3.16)-(3.21) (2+1 REMPI detection equations) to generate a set of β_k^{FG} parameters which are used to simulate image angular distributions. The bipolar moments are then optimized to achieve best fits to the experimental image angular distributions.

Direct Inversion Method

The direct inversion method is self-evident. Obtaining analytical expressions of bipolar moments as functions of image anisotropy parameters β_k^{FG} is technically difficult. Instead, the experimentally derived anisotropy parameters are inserted into the left hand sides of Equations (3.16)-(3.21) (2+1 REMPI detection equations) and the equation set is numerically inverted to solve for bipolar moments. Despite the simplicity of the direct inversion approach, there are some practical difficulties. For 1 photon dissociation followed by 2+1 REMPI detection, there are 9 relevant bipolar moments: $\beta_0^2(20)$, $\beta_0^2(02)$, $\beta_0^2(22)$, $\beta_0^0(22)$, $\beta_0^2(24)$, $\beta_0^2(42)$, $\beta_0^2(44)$, $\beta_0^0(44)$, $\beta_0^2(64)$. This indicates

that 9 experimental image β_k^{FG} parameters are required to form a fully determined set for analysis. For images with significant background, errors in the derived image anisotropy parameters can lead to unphysical bipolar moments. Additionally, without further approximations, direct inversion requires extra measurements since the commonly reported combinations of images represent an underdetermined set. In the case of 2+1 REMPI images, an image detected with VV geometry will provide three image β_k^{FG} parameters (β_2^{VV}, β_4^{VV}, β_6^{VV}), while the HV geometry provides just two image β_k^{FG} parameters (β_2^{HV}, β_4^{HV}), and the VH geometry just provide a single parameter β_2^{VH}. In order to solve the nine dimensional equation set, three more image β_k^{FG} parameters are needed from one or more additional image measurements. As a result, we do not recommend the direct inversion method in general, except in special cases when one or more bipolar moments can be independently determined. For example, in cases of jet-cooled triatomic molecules photodissociation (like OCS), by conservation of angular momentum, recoil velocity vectors of photofragments **v** must be approximately perpendicular to the rotational angular momentum vector ***j***. In this case, it is often assumed that $\beta_0^0(22)$=-0.5 and $\beta_0^0(44)$=0.375.

There are additional approximations which can also be applied. In the semi-classical limit the moments $\beta_0^2(42)$ and $\beta_0^2(64)$ can be expressed as linear combinations of other bipolar moments. Using Equation (7d) from Rakitzis *et al.*[90] and Equation (4) from Ritchie *et al.*[91] and assuming the interference terms are negligible, we find

$$\beta_0^2(42) = \frac{7}{12}\beta_0^2(02) - \frac{5}{12}\beta_0^2(22) \tag{3.22}$$

$$\beta_0^2(64) = \frac{11}{14}\beta_0^2(24) - \frac{3}{14}\beta_0^2(44) \tag{3.23}$$

With these approximations and with as assumed **v** perpendicular to ***j*** correlation, there are five bipolar moments remaining in the equation set to be solved. In this case, only five β_k^{FG} parameters from images are needed, which can be obtained from two different combinations of measurements. The five β_k^{FG} parameters can be determined from a set of images with three different geometries (VH, HV, VV) from a single rotational transition or one set of VV geometry images using two different rotational branches (S/O+R/P) for detection. Either combination will provide six β_k^{FG} parameters which are sufficient to extract all the remaining bipolar moments.

In practice, however, high quality sliced images with HV detection geometries are difficult to obtain in the cases of rapid dissociations via a parallel transition. In such cases, the horizontally polarized dissociation laser will generate product clouds which have a nodal plane. We find that sliced HV images often show relatively low signal to noise ratio, which generally results in large uncertainties in the experimental β_k^{FG} parameters. On the other hand, images using the VV geometry produce more photofragments and ions in the imaging plane. An additional benefit of the VV geometry is that it is possible to reconstruct a non-sliced image to obtain a sliced image. Ion clouds generated in this geometry will preserve cylindrical symmetry, which fulfill the requirements of Abel-inversion based reconstruction algorithms.[26, 60] Perhaps the most important advantage of using the VV geometry is that one-color experiments can be used to extract fragment vector correlations.

Forward Convolution Method

In many cases, direct inversion will not be an ideal method, as will be shown in the next chapter. In such cases, we suggest using the forward convolution method to

simulate angular distributions which fit to the experimental data. For the forward convolution method, a trial set of bipolar moments are used in Equations (3.16)-(3.21) (2+1 REMPI detection equations) to generate a set of β_k^{FG}parameters which are used to simulate image angular distributions. The bipolar moments are optimized to achieve best fits to the experimental image angular distributions.

There are multiple ways of searching for the best trial bipolar moments. The most straight forward way is to manually adjust all nine bipolar moments until a reasonable fit is achieved. In practice, some lower order bipolar moments $\beta_0^2(20)$, $\beta_0^2(02)$, $\beta_0^0(22)$ should be adjusted first to make the simulated angular distributions qualitatively match the shape of the experimental distribution. Next, the remaining bipolar moments can be iteratively adjusted to refine the simulated distributions. However, this method is difficult to apply because the simulated images will be sensitive to value changes of all 9 bipolar moments. And sometimes higher order bipolar moments, like $\beta_0^0(44)$ and $\beta_0^2(64)$ can have a dramatic effect on the shapes of the distributions. In addition, the optimized bipolar moments set from this method can sometimes provide a less physically reasonable picture of photodissociation dynamics. For example, a resulting set may include a $\beta_0^0(22)$ value close to -0.5 indicating a physical picture of the photofragment ejected from the parent molecule in a cart-wheeling style, along with a $\beta_0^0(44)$ value close to 1 which indicates a physical picture of the photofragment ejected with a helicopter style movement. In some cases these two bipolar moments from the same optimized set may be contradictory, and unphysical.

It is beneficial if the bipolar moment sets can be constrained by certain physical models so that only dynamically reasonable combinations of bipolar moments are available. It should be noted that the bipolar moment sets from this constrained search

still covers the whole phase space of all the possible combination of bipolar moment sets. These constraints also reduce the number of variables for the simulation. The fitting procedure can be constrained by utilizing the five limiting cases developed by Dixon. Dixon discussed five possible limiting cases, each with a different extreme relative orientation (either parallel or perpendicular) of the three vectors (**μ**, **v** and ***j***). A schematic diagram of the five limiting cases is shown in Figure 3.1. Case A and B describe parallel transitions, while cases C-E describe perpendicular transition. The Case A and D describe "helicoptering" motions of photofragments, while the cases B, C and E describe "cartwheeling" motions of photofragments. Each of these limiting cases has a corresponding set of bipolar moments with the values shown in Table 3.2. The expected vector correlations of a real molecule can be described as a linear combination of these limiting cases.[34, 92] In this way, the measured bipolar moments can often be interpreted as terms of specific dynamical pathways.

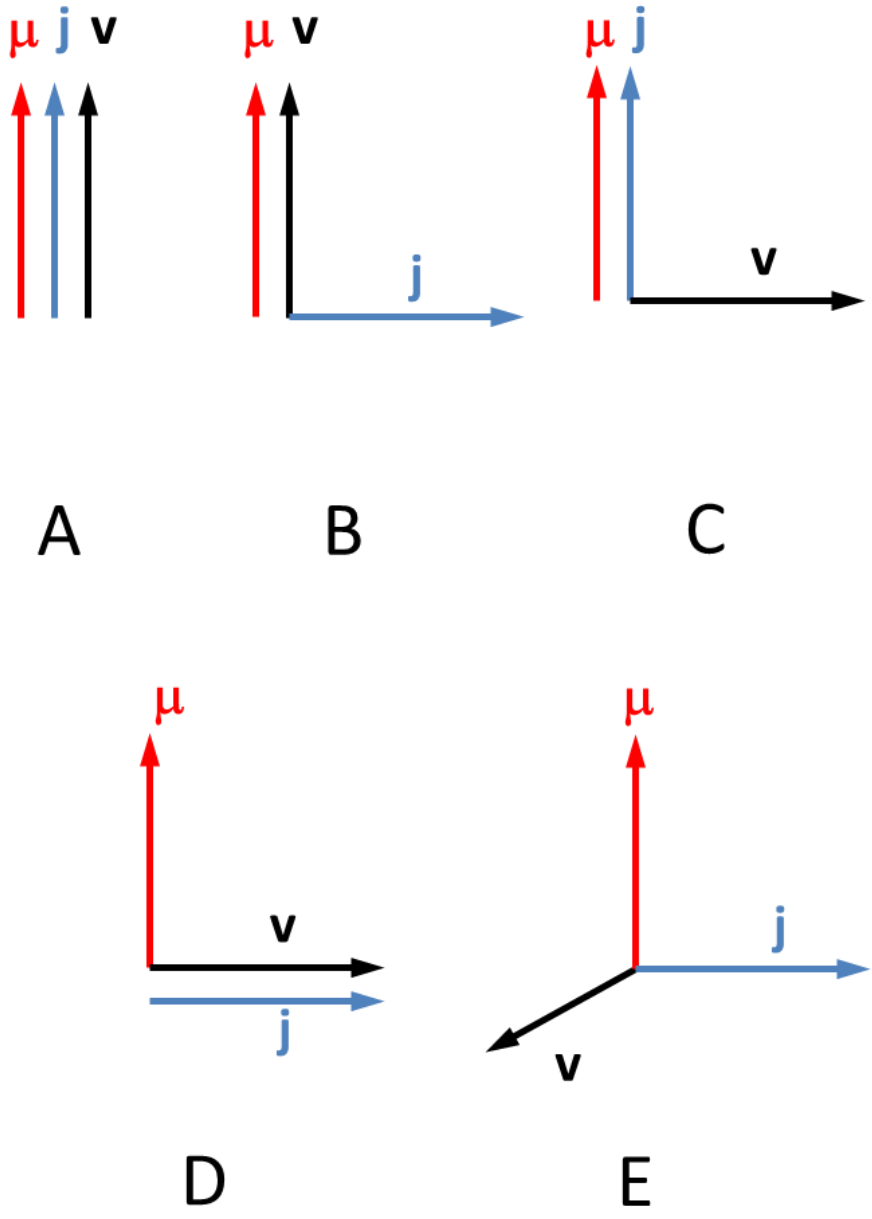

Figure 3.1: The vector correlation configurations of limiting cases.

We have adopted their approach of using a linear combination of limiting cases to generate full sets of physically meaningful bipolar moments for simulation purposes (excluding the $\beta_0^0(44)$ moment, which will be discussed later). With our 2+1 REMPI Equations the resulting set of bipolar moments can yield image anisotropy parameters β_k^{FG} and thus image angular distributions to be compared with experimental image measurements.

Table 3.2: Bipolar moments associated with Limiting Cases A-E. The data in this table are adapted from Dixon, JCP, 85 (4), 1866 (1986) and Docker, Chem. Phys. 135 (3), 405 (1989).[34, 64]

Bipolar moments	Case A	Case B	Case C	Case D	Case E
$\beta_0^2(20)$	1	1	-0.5	-0.5	-0.5
$\beta_0^2(02)$	1	-0.5	1	-0.5	-0.5
$\beta_0^0(22)$	1	-0.5	-0.5	1	-0.5
$\beta_0^2(22)$	-1	0.5	0.5	0.5	-1
$\beta_0^2(42)$	1	-0.5	0.375	-0.5	0.125
$\beta_0^0(44)$	1	0.375	0.375	1	0.375
$\beta_0^2(24)$	1	0.375	-0.5	-0.5	0.125
$\beta_0^2(44)$	-1	-0.375	-0.375	0.5	0.75
$\beta_0^2(64)$	1	0.375	-0.3125	-0.5	-0.0625

Based on the values in Table 3.2, the $\beta_0^0(44)$ moment generated from linear combinations of limiting cases will always range from 1.0 to 0.375, and will not span the full range from -3/7 to 1. As a consequence, the forward convolution simulations with linear combination of limiting cases generating $\beta_0^0(44)$ produce noticeably poorer fits than when treating the $\beta_0^0(44)$ moment as an adjustable parameter for fitting (*vide infra*). The limiting cases B, C and E describe the vector correlations of diatomic fragments

arising from the photodissociation of a triatomic molecule at *j*=0. The fragments are constrained by angular momentum conservation to have a delta-function distribution of **v**⊥***j*** correlations with limiting values of $\beta_0^0(22)$=-0.5, (lower bound of this moment) and $\beta_0^0(44)$ = 0.375 (not the lower bound of this value). For a real system with *j*≠0, depolarization will broaden the **v**-***j*** correlation distribution, while still peaking at **v**⊥***j***. The depolarization of the **v**⊥***j*** correlation can be represented in the A-E parameter space by mixing in small amounts of cases A and D which correspond to **v**∥ ***j*** correlation. This procedure works because the range of $\beta_0^0(22)$ values spans the full range monotonically. In this scenario, the $\beta_0^0(22)$ moment will be a non-limiting value representing depolarization. However, this fails for $\beta_0^0(44)$. Cases A and D contribute a $\beta_0^0(44)$=1, while the B, C, and E cases contribute a $\beta_0^0(44)$=0.375 which do not describe the limits of the range of $\beta_0^0(44)$ values. Additionally, the function that describes the transition from the A and D $\beta_0^0(44)$ value of 1 to the B, C, and D $\beta_0^0(44)$ value of 0 is not monotonic. Due to these two issues, depolarization of $\beta_0^0(44)$is not well described by utilizing partial contributions of the A and D cases.[93] As a consequence, we have chosen to treat the $\beta_0^0(44)$ moment as an adjustable parameter while using a linear combination of limiting cases to generate other bipolar moments, as a practical approach. The uniqueness of this $\beta_0^0(44)$ moment revealed that this method may be incomplete and it is still an unsolved question whether the five limiting cases cover the full phase space of the bipolar moments in a two-photon REMPI process. We are not certain whether or not there could be another limiting case which describes the two-photon excitation process and contribute to some high order bipolar moments, including the $\beta_0^0(44)$ moment.

The simulation with all of the bipolar moments has nine degrees of freedom. After employing the linear combination of limiting cases, the degrees of freedom are reduced to five. Based on Equation (2.16) in Chapter II and relevant discussions, the angular distribution of an image with VV laser detection geometry can be fully determined by three image anisotropy parameters (β_2^{VV}, β_4^{VV}, β_6^{VV}); the angular distribution with HV laser detection geometry can be fully determined by two image anisotropy parameters (β_2^{VV}, β_4^{VV}); and the angular distribution with VH laser detection geometry can be fully determined by one image anisotropy parameters (β_2^{VV}). As a result, a single image could at most provide three image anisotropy parameters and more parameters are required to make the set of nine bipolar moments fully determined. The larger the experimental data set, and thus the more image anisotropy parameters, the greater the number of constraints on the analysis. Ideally a pair of two images acquired in the VV geometry at two different detection branches (S/O+R/P) or a set of three images in three geometries (VV, HV and VH) with the same detection branch should give a number of six image anisotropy parameters, which is sufficient to determine the full set of bipolar moments. The former approach does require multiple isolated rotational branch transitions, but is well suited for one-color experiments. The latter approach does not require multiple isolated rotational branch transitions and we find that in practice it provides more reliable fits than the former method.

When using forward convolution simulation to fit the experimental angular distributions, we have used two general methods to conduct the fitting: manual adjustment and Monte Carlo sampling. When conducting a manual adjustment, the fractional contributions of each of the five limiting cases (with an extra constraint that the sum of the A-E percentage equals 100%) and the $\beta_0^0(44)$ moment are adjusted until

the simulated angular distributions overlap the best with the experimental distributions. The Monte Carlo sampling, on the other hand, can perform simulation fits automatically given a chi square minimization constraint.

Monte Carlo Sampling

Monte Carlo sampling can be utilized in generating sets of bipolar moments for the forward convolution simulation of the image angular distributions. In each loop, nine random generators will generate a full set of nine bipolar moments, which will be plugged into the 2+1REMPI Equations to generate image anisotropy parameters β_k^{FG} for the images to be simultaneously fitted, Equation (2.16) in Chapter II is then utilized to generate simulated angular distributions, which are then compared to the experimental angular distributions. A chi-squared criterion is employed to evaluate the fit to each of the simultaneously fitted image angular distributions, and these chi-squared values are summed together. If the sum of the chi-squared values is lower than the user designated threshold, the corresponding set of randomly generated bipolar moments will be accepted and stored; if the sum of the chi-square values is greater than the threshold, the bipolar moments will be rejected. The above steps will be repeated in loops and a data base of suitable bipolar moment sets can be achieved.

The resulting bipolar moment sets that yield acceptable fits are not always physically reasonable. This issue also presents at manual adjustments with full bipolar moment sets. In order to eliminate physically unreasonable results, and also to save CPU time, the range of randomly generated bipolar moments should be limited. For example, if the image is from photodissociation of triatomic molecules in a jet-cooled

molecular beam, the recoil velocity should be perpendicular to the rotational angular momentum. Thus, the $\beta_0^0(22)$ moment should be limited to negative values.

Similarly, we can also apply Monte Carlo sampling to the linear combination of limiting cases. Instead of utilizing random number generator to generate bipolar moment sets, we can randomly generate percentages of the limiting cases A-E. In practice we treat the $\beta_0^0(44)$ moment independently from the linear combinations of limiting cases, and use random generators to generate values for this bipolar moment. The rest of the procedures are the same as the other Monte Carlo sampling methods mentioned above. Using this method, the selected fits will correspond to physically reasonable bipolar moments.

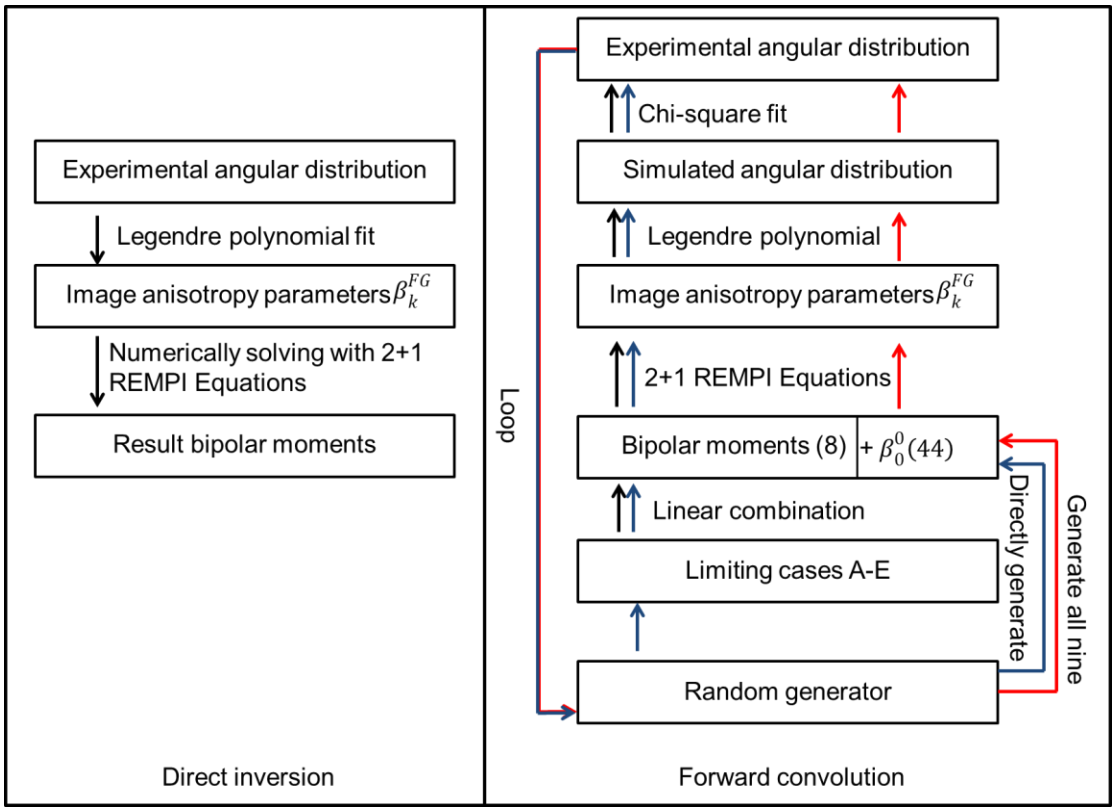

Figure 3.2: Flow chart of the methods. The left panel shows the direct inversion method. The right panel shows forward convolution with manual adjustments (black arrows); Monte Carlo sampling bipolar moments (red arrows); and Monte Carlo sampling linear combination of limiting cases (blue arrows).

A flow chart comparing the similarities and differences of the different methods described in this chapter is shown in Figure 3.2. When comparing the manual adjustments method and the Monte Carlo sampling methods, there are indeed advantages and disadvantages for both methods. The advantage of manual adjustments is that it is more forgiving of noise in the experimental angular distributions. For example, if there are unphysical data points in the experimental angular distribution, a manual adjustment simulation is likely to ignore these data points. On the other hand, manual adjustment is much more likely to introduce bias in fittings. The Monte Carlo sampling will be unbiased and will evenly sample over the phase space of bipolar

moment sets/ linear combination of limiting cases sets. One major disadvantage of the Monte Carlo sampling in this work is that when the number of simultaneously fit image angular distributions increases, the amount of loops necessary for sampling will increase dramatically (on the magnitude of billions of loops if simultaneously fitting six images) to obtain only less than one hundred acceptable fits.

This Monte Carlo sampling method discussed here is a relatively efficiency, and easy programing method because of its lack of optimization algorism. A future improvement can involve certain stepwise optimization processes. For example, in each new step, the program should select one variable (bipolar moments or linear combination of limiting cases) and randomly change the value of it from the last accepted value, creating a new set of variables that will be used to generate the new angular distributions. Then the chi-square test should be utilized to determine whether the new step fits better (accept) or worse (reject). If accepted, the next step optimization will use variables from this accepted step. If rejected, the next step will try another random variation of one variable based on the last accepted step. This way, the bipolar moments from fitting will converge to certain results, instead of sampling freely. This type of program with Monte Carlo optimization algorithm will be more CPU efficient, but will have risks of converging to local optimizations instead of global optimizations.

CHAPTER IV

EVALUATION OF THE NEW METHOD*

Application of the Direct Inversion and Forward Convolution Methods to OCS Experimental Results

In order to test Equations (3.16)-(3.21), we first re-analyzed our OCS one-color CO non-sliced ion images (*j*=58, 62, 72).[65] Both the direct inversion and forward convolution methods, described in Chapter III, were utilized in order to compare their performance. For analysis with the direct inversion method, we used the previously obtained imaging β_k^{VV} parameters. These imaging β_k^{VV} parameters were calculated by applying Equation (2.16) to angular distributions of the CO images. Each set of data consist of 5 β_k^{VV} parameters from one pair of S and R-branch images for each ***j***; β_2^{VV} and a β_4^{VV} from the S-branch image and β_2^{VV}, β_4^{VV}, β_6^{VV} from the R-branch image. The set of 5 β_k^{VV} were treated with the Equation (3.16)-(3.21) and the necessary approximations shown as Equations (3.22)-(3.23). We also adopted the assumptions that $\beta_0^0(22)$=-0.5 and $\beta_0^0(44)$=0.375, which have been discussed earlier. The resulting bipolar moments are listed in Table 4.1 as “Direct inversion”. Forward convolution simulations, as described earlier, were also applied to our OCS one-color CO images using linear combinations of the limiting cases in conjunction with Equation (3.16)-(3.21). The angular distributions of an S and an R-branch image were simultaneously fit

---

* Part of this chapter is reprinted from “W. Wei, C. J. Wallace, M. P. Grubb and S. W. North, The Journal of Chemical Physics 147 (1), 013947 (2017)”, with the permission of AIP Publishing.

for each rotational state. The resulting bipolar moments are listed in Table 4.1 as "Forward convolution". By comparison, it is clear that the bipolar moments from both direct inversion and forward convolution methods with Equation (3.16)-(3.21) are consistent with our previously reported bipolar moments.[65] The only result that is slightly different is the $\beta_0^2(20)$ value for *j*=72, by forward convolution method of this work. These bipolar moments are also consistent with the theoretical calculations reported in our earlier OCS work.[65]

Our earlier OCS work used the set of bridging equations given by Denzer *et al*.[91] to convert from Rakitzis alignment parameters to bipolar moments, which is slightly different from the bridging equations used in this work (Equations (3.13)-(3.15)). Detailed discussions of the differences of these two versions of the equations will be given in the later in this chapter.

Table 4.1: Bipolar moments for OCS photodissociation at 214 nm, analyzed with direct inversion and forward convolution methods. Table reproduced from Wei *et al*.[94]

	j	$\beta_0^2(20)$	$\beta_0^2(02)$
Direct inversion	58	0.07± 0.06	0.14± 0.12
Forward convolution	58	0.09± 0.03	-0.01± 0.13
Direct inversion	62	0.20± 0.06	-0.22± 0.12
Forward convolution	62	0.22± 0.03	-0.29± 0.13
Direct inversion	72	0.27± 0.06	-0.38± 0.12
Forward convolution	72	0.47± 0.03	-0.41± 0.13

New non-sliced velocity map ion images were collected arising from the photodissociation of OCS at 230 nm which has been extensively studied. The spatial anisotropy and vector correlations of the products have been previously reported.[95-97] We have utilized 2+1 E-X REMPI (both via S and R-branch) detection for CO (v=0, *j*=48) due to the sensitivity to alignment.[68] The images were analyzed and angular distributions of each image were obtained. Forward convolution simulations with linear combination of the limiting cases and the 2+1 REMPI Equations were used to simultaneously fit the angular distributions of an S and an R-branch image for *j*=48.

Two different simulations were performed; one treating the $\beta_0^0(44)$ moment as a freely adjustable parameter and the other where the $\beta_0^0(44)$ moment is the result of linear combinations of limiting cases. The results for both simulations are shown in Figure 4.1. It is clear that when the $\beta_0^0(44)$ moment values that are calculated from linear combinations of limiting cases are used in the simulation, the fits are worse. Although they match the general shape of the angular distribution, they miss the details. These poor fits are not isolated issues and are due to the fact that $\beta_0^0(44)$ moment values calculated from linear combinations of limiting cases do not cover the full range of possible values, as mentioned in the last chapter. As a consequence, we recommend that $\beta_0^0(44)$ moment values not be determined from linear combinations of limiting cases.

The resulting bipolar moments from the approach of treating the $\beta_0^0(44)$ moment as a freely adjustable parameter are $\beta_0^2(20)$=0.11±0.08 (**μ-v**), $\beta_0^2(02)$=0.24 ±0.22 (**μ-*j***) and $\beta_0^0(22)$ =-0.39±0.11 (**v-*j***).[98] Previous measurements by Janssen *et al.* yielded $\beta_0^2(20)$=0.12±0.01,[95] similar to our derived value. The $\beta_0^2(02)$ (**μ-*j***) moment is small but positive at *j*=48, consistent with CO products arising from dissociation via both the A

state and B state of parent OCS.[96] The A state will yield product CO with **μ** perpendicular to ***j*** correlation ($\beta_0^2(02)$=-0.5), while B state will yield CO with **μ** parallel to ***j*** correlation (positive $\beta_0^2(02)$). Our analysis also yields the $\beta_0^0(22)$ (**v-*j***) moment close to -0.5 (perpendicular), as expected. Deviations of $\beta_0^0(22)$ values from the limiting value are consequence of non-negligible parent rotational motions.

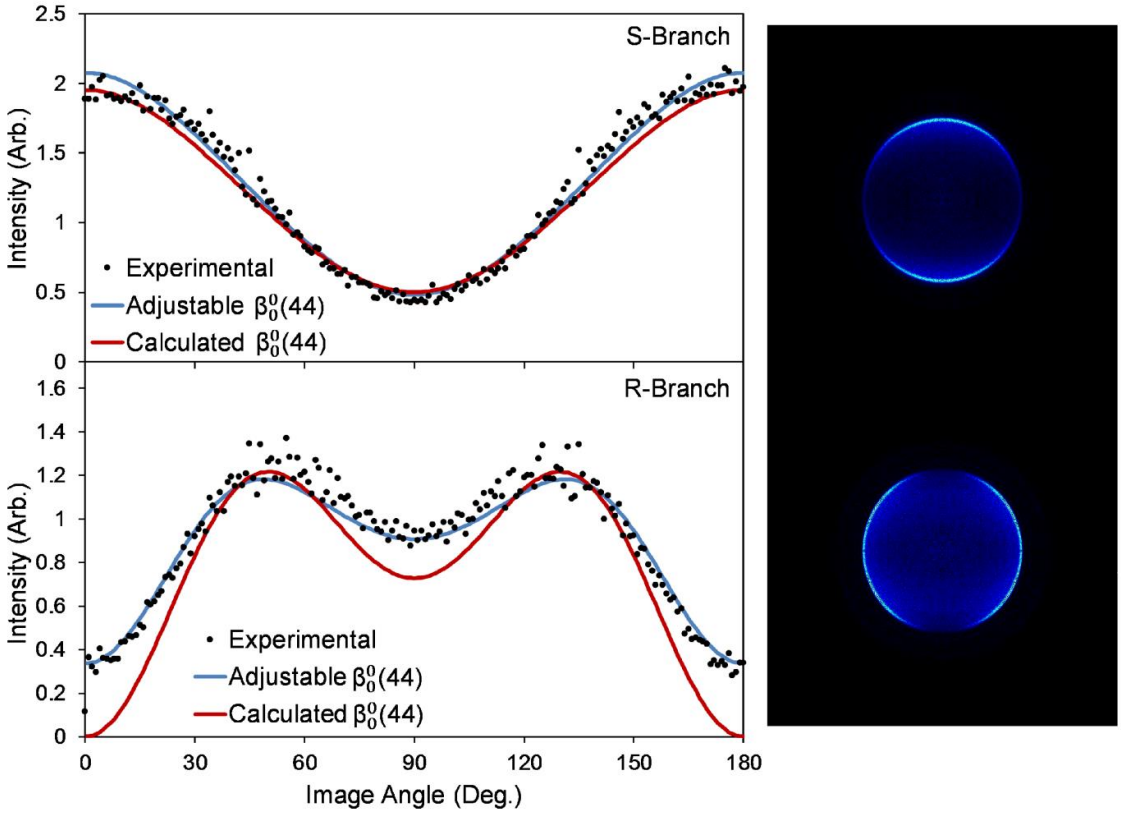

Figure 4.1: Experimental angular distributions from the photodissociation of OCS at 230 nm, probing CO(*j*=48) near 214 nm fit with the forward convolution method. The dissociation and probe laser polarization of both images are vertical. The top panel corresponds to the S-branch and the bottom panel is R-branch. The simulation with $\beta_0^0(44)$ moment treated as a freely adjustable parameter is shown in blue, while the simulation with $\beta_0^0(44)$ moment treated as a linear combination of limiting cases is shown in red. Figure reproduced from Wei *et al*. JCP, 147, 013947 (2017). [94]

A Second Test Case: 2+1 REMPI Q-Branch System

As an additional test of our method on Q-branch data, we also analyzed NO Q-branch 2+1 C-X REMPI non-sliced ion images from NO_2 photodissociation at 355 nm using three laser polarization geometries: VV, HV, and VH, from earlier publication of Mo *et al.*[88] One challenge in experiments involving Q-branch detection is that the detection sensitivity factor s_k for Q-branch is often not known a priori and must be determined independently for each REMPI system. These factors need to be determined with the knowledge of the ratio between parallel and perpendicular component of transitions to the intermediate virtual state for Q-branch transition. As discussed in the last chapter, the Q-branch s_2 and s_4 factors can be determined using Equation (3.3). Mo *et al.* [88, 89] has previously determined the ratio between the parallel and perpendicular transitions and reported the P_k values to be P_0:P_2:P_4=1: 0.94: 0.18 at j=30.5. With these values, the Q-branch s_2 and s_4 factors are determined to be s_2=1.051 and s_4=0.542.

We have analyzed three NO ($X\ ^2\Pi_{1/2}$, v=0, j=30.5, f) Q-branch images of different laser geometries (VV, VH and HV) from earlier publication of Mo *et al.*[88] The images were four-fold symmetrized prior to analysis. Angular distributions of the images are obtained and the best fits are shown in Figure 4.2.

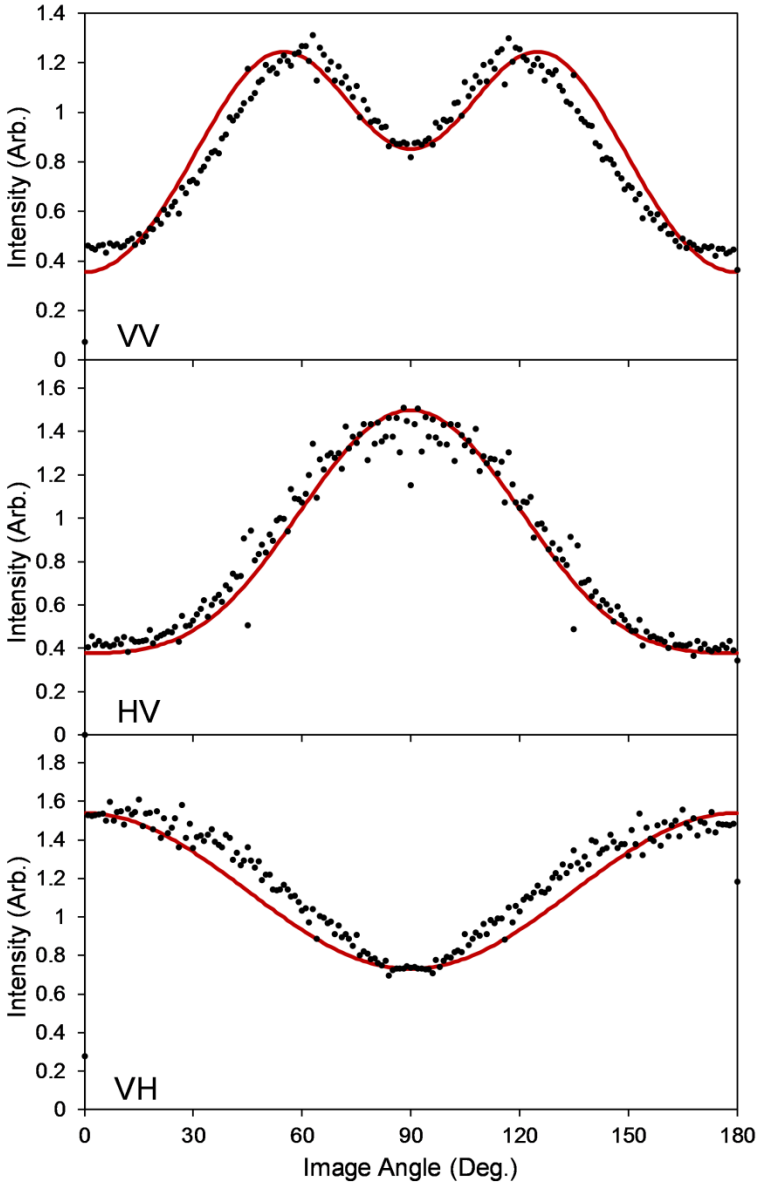

Figure 4.2: Experimental angular distributions of NO ($X\ ^2\Pi_{1/2}$, v=0, j=30.5, f) 2+1 REMPI Q-branch images from NO_2 355 nm photodissociation fit with the forward convolution method. Three detection geometries (VV, HV and VH top to bottom panels) are shown. The raw data, adapted from Mo *et al*. [88] [99], is shown as closed circles and our simulations as the solid lines. Figure reproduced from Wei *et al*. JCP, 147, 013947 (2017). [94]

We find that reasonable fits can be achieved using the calculated s_2 and s_4 factors reported by Suzuki and coworkers. Although these are some differences between our fits and the VH image angular distribution, which should only exhibit a $\cos^2(\theta)$ dependence, we suggest that the asymmetry in the experimental data and subsequent symmetrization is a likely source of the error.

The obtained bipolar moments, $\beta_0^2(02)$ (**μ-*j***), $\beta_0^0(22)$ (**v-*j***), and $\beta_0^2(20)$ (**μ-v**), shown in Table 4.2, are all consistent with conclusions given by the original paper by Mo *et al.* [88] The values of $\beta_0^2(02)$ and $\beta_0^0(22)$ indicate **μ** perpendicular to ***j*** and **v** perpendicular to ***j*** correlations respectively. Modest deviation of $\beta_0^0(22)$ values from the limiting case values are the result of depolarization caused by parent rotation. In the original paper, the authors reported an angle between **μ** and **v** to be in the range of 38-44 degrees, corresponding to $\beta_0^2(20)$ =0.28-0.43, in good agreement with our simulations.

Table 4.2: Comparison of bipolar moment values from this work to Mo *et al*. The results from this work are obtained by forward convolution simulation fitting of angular distributions from their NO images. The literature values were calculated from the geometric model given in Figure 3 from Mo *et al*. [88] Table reproduced from Wei *et al*. JCP, 147, 013947 (2017).[94]

	$\beta_0^2(02)$	$\beta_0^0(22)$	$\beta_0^2(20)$
This work	-0.43±0.18	-0.43±0.06	0.35±0.08
Mo et al.	-0.5	-0.5	0.28-0.43

An Issue with the Earlier Version of the 2+1 REMPI Equations

In the last chapter it was noted that when deriving the working 2+1 REMPI Equations (3.16)-(3.21) we derived our own equations as the bridging equations

between Rakitzis's molecular frame polarization parameter $a_q^{(k)}(p)$ and Dixon's bipolar moments. The reason for choosing to derive our own bridging equations instead of using the similar equations published by Ritchie and coworkers [91] is that in certain cases utilizing their bridging equations, failed to produce reasonable results.

The test case used was the simulation of the angular distributions resulting from an image of a hypothetical case where there were no correlations between the parent molecule transition dipole moment and the other vectors. It was assumed that in this special scenario the only correlated vectors are the photo-fragment recoil velocity vector and the rotational angular momentum vector of the photofragments, and they are perpendicular to each other (**v**⊥***j***). With these assumptions, we set $\beta_0^0(22)$ =-0.5, $\beta_0^0(44)$=0.375 and set all other 7 bipolar moments to zero. The simulated angular distributions of VH detection geometry images are shown in Figure 4.3.

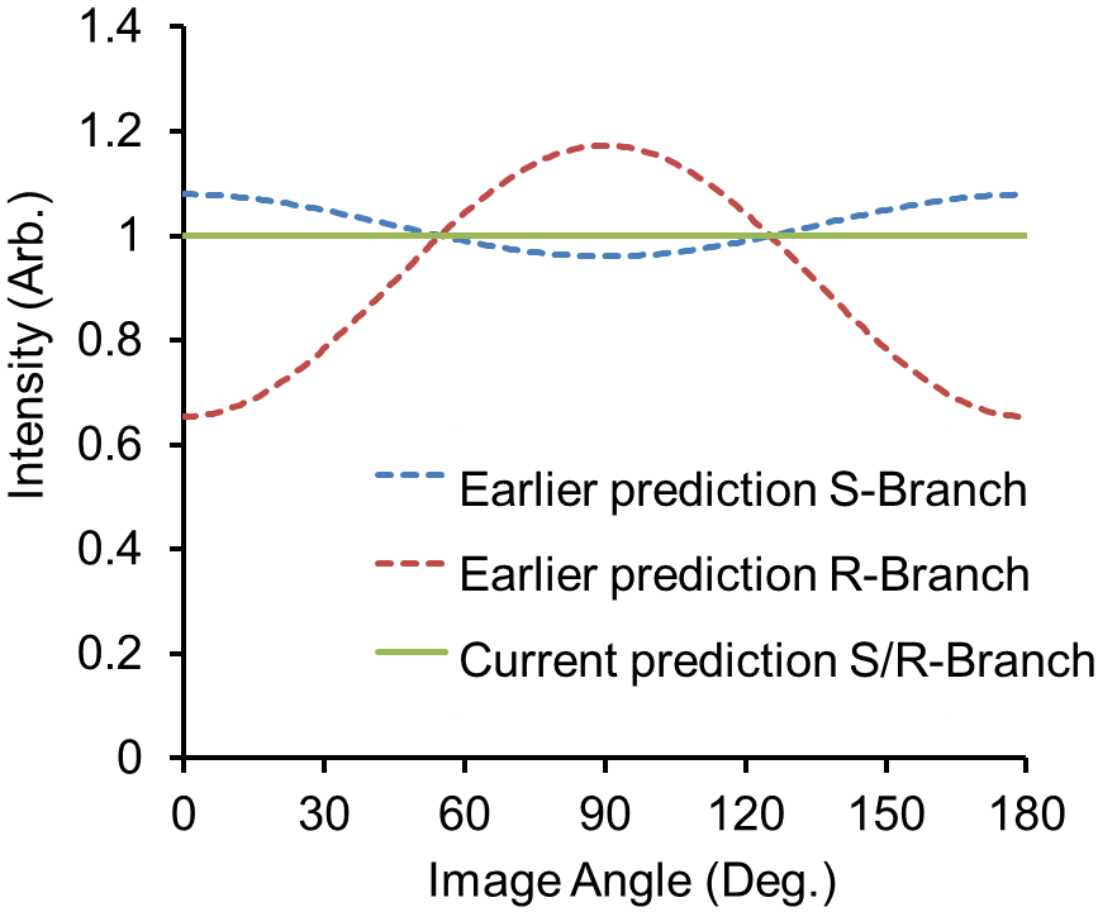

Figure 4.3: The simulation of angular distribution of the hypothetical case, with different two versions of the 2+1 REMPI Equations. The distributions in dashed blue line (S-Branch) and dashed red lines (R-Branch) are simulated by the earlier version of our 2+1 REMPI Equations with bridging equations from Ritchie and coworkers, while the distribution in solid green line is by the Equation (3.16)-(3.21) with our own bridging equations.

It can be clearly seen that the angular distributions with bridging equations of Richie and coworkers are anisotropic and they show the opposite anisotropy pattern from S branch to R branch. Meanwhile, the angular distributions with our own bridging equations are isotropic, regardless of probe branch. We believe that isotropic distribution should be the true result for this hypothetical case. Since there are no

correlations between the parent molecule transition dipole moment and photo-fragment recoil velocity vectors, the photofragments will form an isotropic distribution in the product cloud. Meanwhile, since there are no triple vector correlations, the horizontally polarized probe laser will have same detection efficiency for all of the photofragments on the image plane, both for the S/O branches and for the R/P branches. We can see that the earlier version of 2+1 REMPI Equations failed to predict such isotropic distribution.

Discussion of Applications of 1+1 REMPI Equations to 2+1 REMPI Detected Images

In this section, we use the angular distributions resulting from images of the hypothetical case we demonstrated earlier, to discuss the possible applications of the 1+1 REMPI Equations on images detected by 2+1 REMPI. The hypothetical case has no vector correlations other than **v** perpendicular to ***j***. With these assumptions, we set $\beta_0^0(22)$=-0.5, $\beta_0^0(44)$=0.375 and set all other 7 bipolar moments to zero. Our 2+1 REMPI Equations were used to simulate S/O and R/P-branches angular distributions with VV, and HV detection geometries.

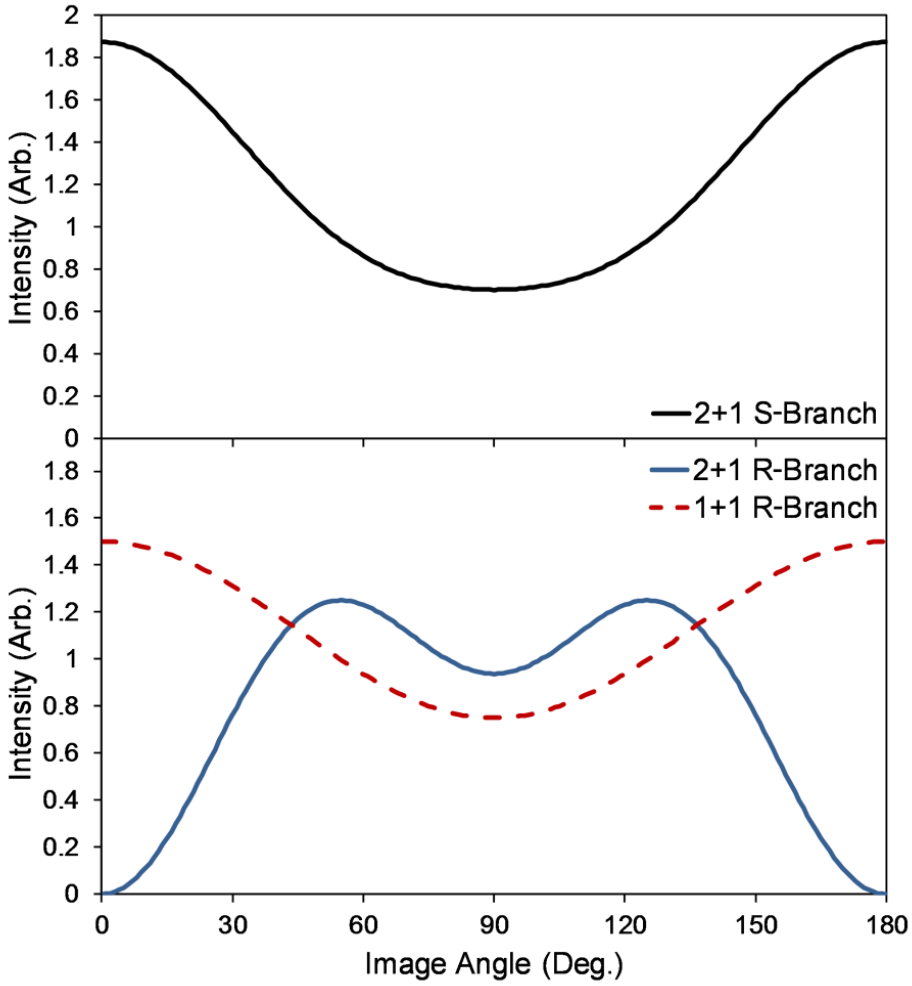

Figure 4.4: Simulated angular distributions of the hypothetical case with no spatial anisotropy and with v⊥*j* correlation. The top panel shows simulated angular distribution detected by 2+1 REMPI S-branch with β_2^{VV}=0.714 and β_4^{VV}=0.161. In the bottom panel simulated angular distributions detected by R-branch 2+1 REMPI (solid line) and 1+1 REMPI (dashed line) are shown with β_2^{VV}=-0.357 and β_4^{VV}=-0.643 for 2+1 and β_2^{VV}=0.5 for 1+1. Figure reproduced from Wei *et al*. JCP, 147, 013947 (2017). [94]

The simulated angular distributions of images taken with HV and VV geometries in the same branch are identical. This is also consistent with the loss of spatial anisotropy in the laboratory frame. Figure 4.4 shows the angular distributions arising

from VV geometries for this hypothetical case. The simulated 2+1 REMPI ion images for S/O-branches exhibit modest $\cos^4(\theta)$ contributions. The simulated 2+1 R/P-branch REMPI ion images, however, are more interesting since they exhibit clear four-fold symmetry and have a very pronounced $\cos^4(\theta)$ dependence. The $\cos^4(\theta)$ angular dependence is a consequence of the two-photon process for 2+1 REMPI. We are currently pursuing experimental measurements which will verify these predictions. As a comparison, we have simulated the angular distributions of image from 1+1 REMPI R-branch detection using the 1+1 REMPI Equations reported by Grubb *et al.*[82, 83] for the same set of bipolar moments (lower panel of Figure 4.4). It is clear that based on these simulations that R-branch 1+1 REMPI and 2+1 REMPI detection will result in significantly different anisotropies and analysis of 2+1 REMPI data using 1+1 REMPI Equations will lead to erroneous results.

Previously, Bañares and coworkers utilized the 1+1 REMPI Equations of Grubb *et al.* to analyze images acquired with 2+1 REMPI detection.[85-87] The authors demonstrated that in cases where the image anisotropy parameter β_6^{VV} from VV laser polarization geometry and β_4^{HV} of HV geometry were negligible the images were only sensitive to k=2 terms of bipolar moments ($\beta_0^2(02)$, $\beta_0^0(22)$, $\beta_0^2(20)$, $\beta_0^2(22)$ and $\beta_0^2(42)$). In such cases, it would appear that the 1+1 REMPI Equations could be used to treat images from 2+1 REMPI detection.[87] While we agree that the 1+1 REMPI Equations can be used in such cases, we note that this is not a general result. For example, the image of O_2 ($a^1\Delta_g$) from ozone photodissociation at 248 nm probed by 4-0 band R/P rotational branch using 2+1 REMPI with HV geometry exhibited clear four-fold symmetry which indicates strong $\cos^4(\theta)$ angular dependence.[100] Thus it is not possible to achieve a reasonable fit of this distribution with only second order Legendre

polynomials. This is particularly true for many images detected by 2+1 REMPI R/P-branches. Therefore, one must be cautious when applying 1+1 REMPI Equations on images detected with 2+1 REMPI.

In certain cases, it is possible to apply the 1+1 Equations on images detected with 2+1 REMPI. For images detected with 2+1 S/O-branch REMPI, if they show no significant $\cos^4(\theta)$ angular dependence with HV laser polarization geometry or no significant $\cos^6(\theta)$ angular dependence with VV laser polarization geometry, it is techincally possible to apply the 1+1 Equations because a two-photon S/O branch process can be viewed like two consecutive one-photon R/P branch processes. The angular distributions resulting from a 2+1 S/O branch REMPI will have a similar shape, as the angular distributions from a 1+1 R/P branch process, but with sharper distributions. Such similarity can be clearly seen from Figure 4.5. However, a slight difference in the distributions can be clearly seen, since more photons are involved in the alignment of angular momentum in a 2+1 REMPI image.

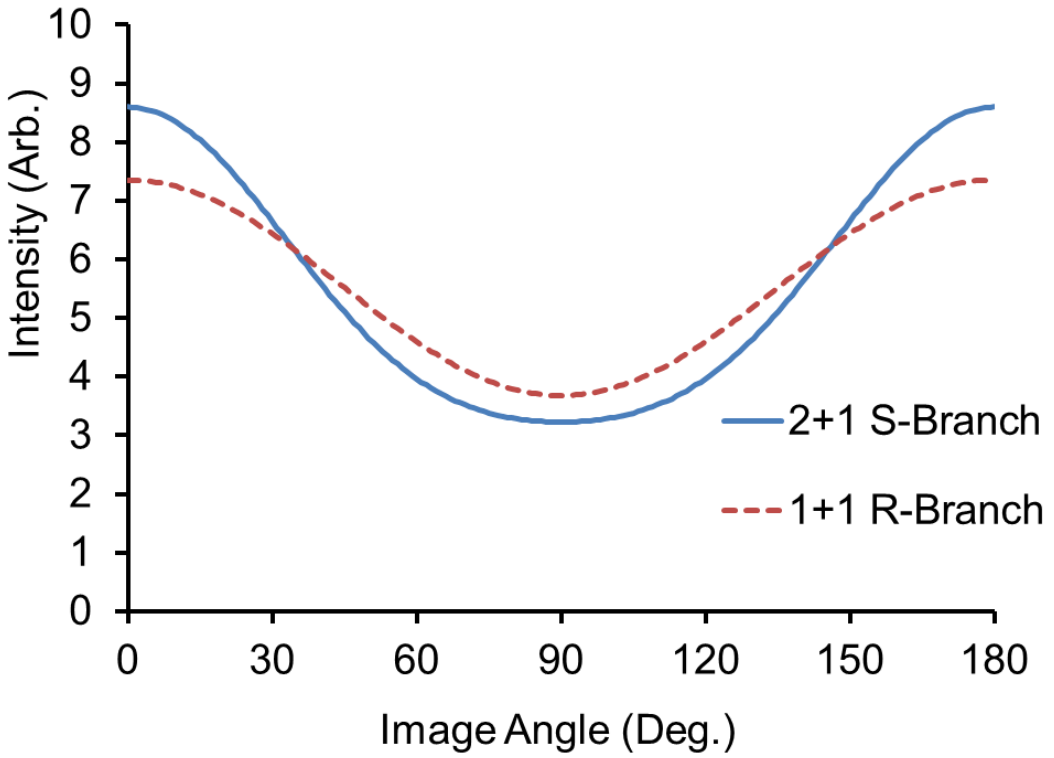

Figure 4.5: Angular distributions of images from the hypothetical case detected by 2+1 S/O branch REMPI (blue) and by 1+1 R/P branch REMPI (red), both assuming the probe lasers are vertically polarized.

The applications of utilizing 1+1 REMPI Equations to treat 2+1 REMPI detected images are only a possible approach and the resulting bipolar moments from these empirical methods has not been quantitatively tested. We still recommend using our 2+1 REMPI Equations.

Application of Monte Carlo Methods for Analysis

The Monte Carlo approach of analysis has been described in the last chapter. There are two major types of applications of the Monte Carlo sampling in this work:

sampling for linear combinations of limiting cases, which can generate a set of bipolar moments with extra constraints, or directly sampling for sets of bipolar moments. We will discuss both approaches and conclude that the former approach is more appropriate.

The images of the 2+1 E-X REMPI probed (both via S and R-branch) CO (v=0, *j*=48) from photodissociation of OCS at 230 nm were used to test the two applications of the Monte Carlo sampling method. Forward convolution simulations were conducted to fit the experimental angular distributions. In the simulations, linear combinations of the limiting cases A-E were chosen by Monte Carlo sampling. The $\beta_0^0(44)$ moments, as discussed before, are not generated from limiting cases, instead they were directly from the Monte Carlo sampling. The optimized fit is shown in Figure 4.6. Ten million loops are run for this fitting process and around 400 sets of linear combinations of limiting cases are obtained, all of which can generate reasonable fits to the experimental angular distributions. Their values for the limiting case ratios are averaged to give an optimized set of linear combinations of limiting cases A-E, which can be used to generate the bipolar moments. The results are shown in Table 4.3. The bipolar moments from the Monte Carlo sampling of linear combinations of limiting cases agree well with both previous publications [95-97] and with fits by manual adjustments forward convolution simulations.[94]

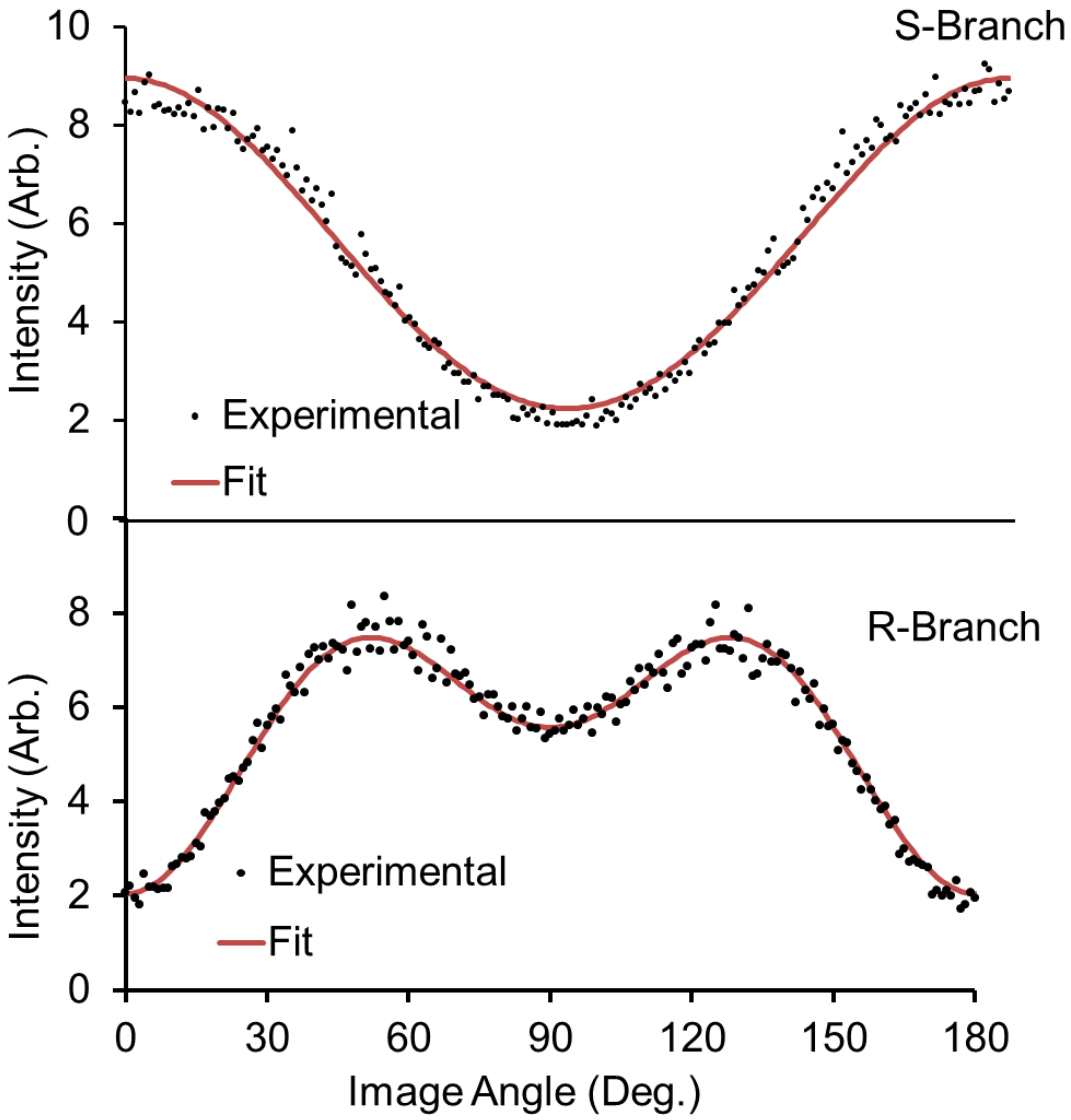

Figure 4.6: Experimental angular distributions from the photodissociation of OCS at 230 nm, probing CO(*j*=48) near 214 nm fit with the forward convolution method including Monte Carlo searching of suitable linear combination of limiting cases. The dissociation and probe laser polarization of both images are vertical. The left panel corresponds to the S-branch and the right panel is R-branch. In both panels, the experimental angular distributions are shown as solid black circles and the simulated angular distributions are shown as red lines.

Table 4.3: Comparison of bipolar moment values resulting from manual adjustments and Monte Carlo fits. The results from this work are obtained by forward convolution simulation fitting of angular distributions from the photodissociation of OCS at 230 nm, probing CO(*j*=48) near 214 nm. The manual adjustments results have been previously reported by Wei *et al*. JCP, 147, 013947 (2017). [94]

	$\beta_0^2(20)$	$\beta_0^2(02)$	$\beta_0^0(22)$
Monte Carlo	0.06±0.1	0.31±0.3	-0.37±0.1
manual adjustments	0.11±0.08	0.24±0.22	-0.39±0.11

The optimized fractional contributions of the limiting cases are: Case A 0.06, Case B 0.31, Case C 0.48, Case D 0.03 and Case E 0.12. The OCS molecules dissociated via the A excited state have transition dipole moments **μ** in the OCS plane slightly deviated from the C-S bond and perpendicular to the rotational angular momentums ***j*** of the CO molecules, which can be described by a combination of Limiting Case B and E. Meanwhile, the OCS molecules dissociated via the B excited state have transition dipole moments **μ** perpendicular to the OCS plane and parallel to the rotational angular momentums ***j*** of the CO molecules, which can be described by the Limiting Case C. For *j*=48, previous literature [94-97] suggests approximately equal possibilities of dissociation via the A and B excited states, which is consistent with our results here (B+E: 0.43, C: 0.48). There is a small amount of combination from Case A and Case D, which can be rationalized by **v**-***j*** correlations deviating from their ideal condition. Such deviation in this particular experiment is usually caused by non-negligible parent rotation from a (*j*≠0) finite temperature molecular beam.

After the Monte Carlo sampling, a data base of sets of linear combination of limiting cases is created, each of which can generate an unbiased, acceptable fit to the same experimental image angular distributions. Distributions of the contribution from

each limiting case are given in Figure 4.7. It is clear that Cases A and D have sharp distributions while the Cases B, C and E have relatively wide distributions. Among all of the possible combinations of the limiting cases, the contributions of Case B, C, and E are correlated and the sum of these three cases is relatively constant. The distributions of each of the bipolar moments generated by the suitable sets of limiting cases are given in Figure 4.8. All of the bipolar moments in this scenario have relatively narrow distribution of values, which is probably the result of constraints imposed by the limiting cases. The $\beta_0^2(02)$ moment seems to have a wider range, which will be discussed later.

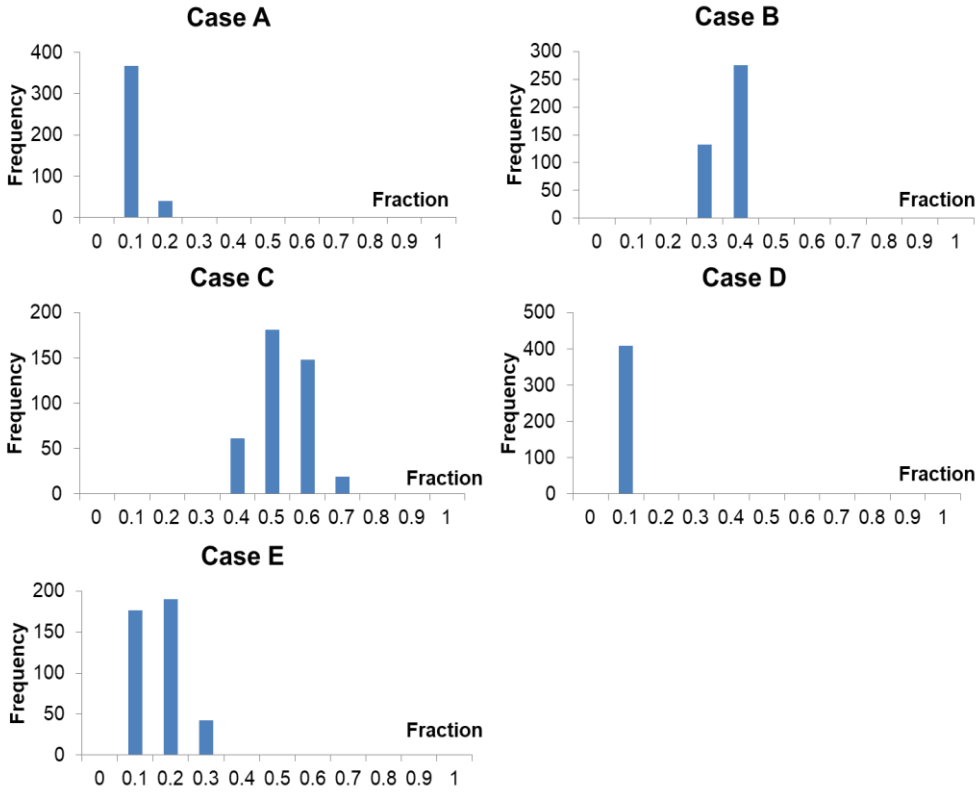

Figure 4.7: Distributions of the limiting cases resulting from the Monte Carlo search forward convolution fit of the OCS 230 nm dissociation experimental angular distributions.

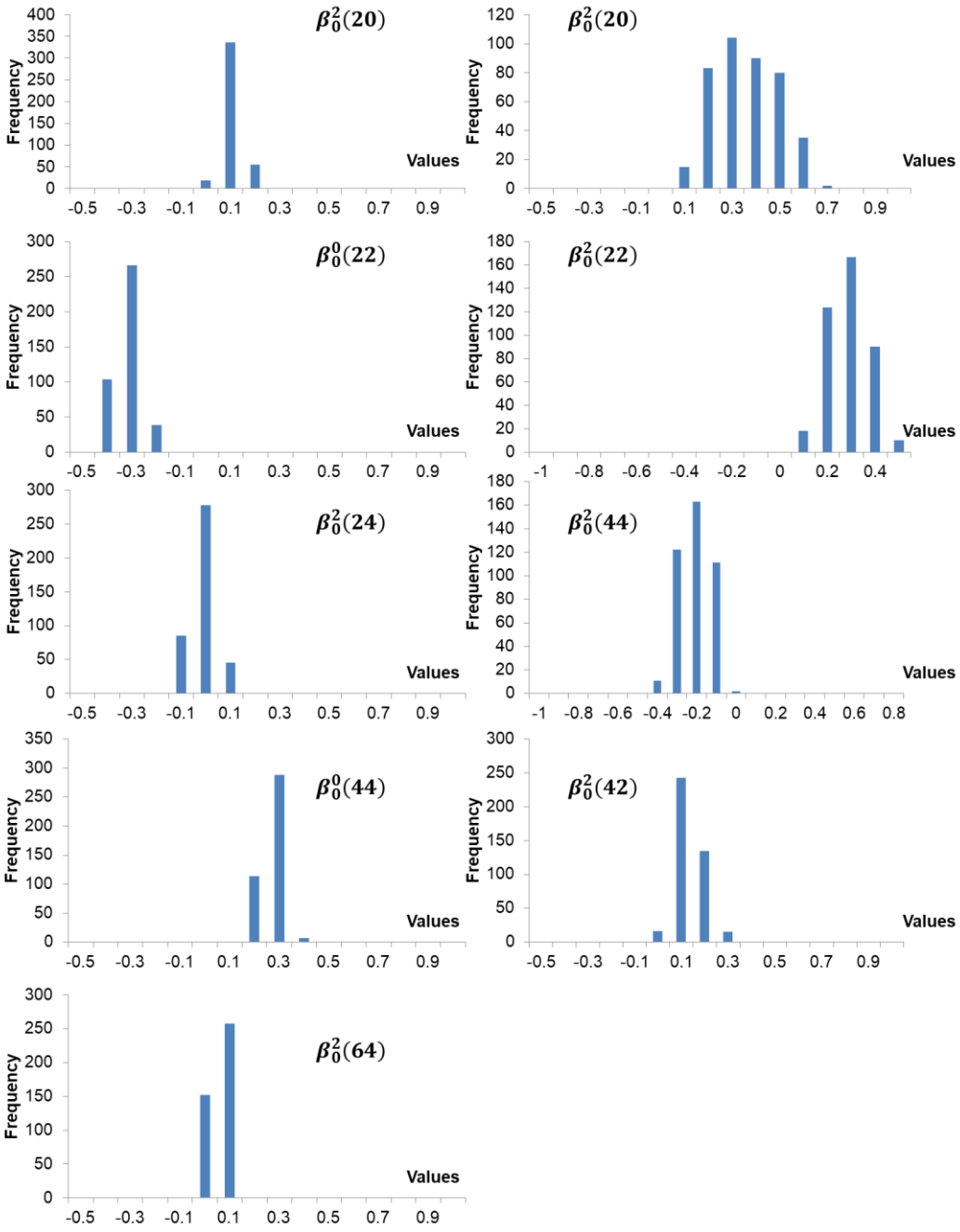

Figure 4.8: Distributions of bipolar moment values derived from linear combination of limiting cases results from the Monte Carlo searching shown in Figure 4.7. The $\beta_0^0(44)$ moment here is directly obtained by Monte Carlo searching instead of from the linear combination of limiting cases.

The Monte Carlo method is also directly used to search for sets of bipolar moments that can generate forward convolution simulations of angular distributions that fit the experimental results, as described in the last chapter. The same experimental OCS 230 nm dissociation data are used to test this method and the optimized simulation results fits the experimental angular distribution as well as all of the other forward convolution treatments. Although several of the low order bipolar moments, $\beta_0^2(20)$ and $\beta_0^0(22)$, are well determined by this approach, i.e. the subset of acceptable fits have narrow ranges of values for these bipolar moments, we have noticed that this approach often yields a broad distribution for the remaining bipolar moments. The optimized values of the $\beta_0^2(02)$ moment even span over the full range of possible values. A practical modification of this Monte Carlo search on bipolar moment method is to confine the range of certain bipolar moments based on the physical picture of the system. For example, for angular distributions from products of jet-cooled triatomic molecule photodissociation, $\beta_0^0(22)$ should be negative.

In order to further evaluate the sensitivity of the forward convolution simulations on the bipolar moments and to explore the possible correlations between these bipolar moments, the method of utilizing Monte Carlo to directly search for optimized bipolar moment sets for forward convolution simulation is tested with the hypothetical case we discussed earlier, i.e. a system with no vector correlations other than **v** perpendicular to ***j*** correlation. A pair of simulated angular distributions of images probed by 2+1 REMPI (one S branch and the other R branch) with VV geometries is generated. The Monte Carlo sampling method is utilized to directly find bipolar moment sets that can generate forward convolution simulations to simultaneously fit these distributions.

The distributions of bipolar moment values with acceptable fits are given in Figure 4.9. The $\beta_0^2(20)$, $\beta_0^0(22)$ and $\beta_0^2(64)$ moments had relatively sharp distribution of values and they were closed to the true values of 0, -0.5 and 0, respectively. The $\beta_0^0(44)$ and $\beta_0^2(42)$ moments had wider bell-shape distributions, but the averaged values were still near the true values 0.375 and 0. The rest of the bipolar moments demonstrated relatively wide and poorly defined distributions.

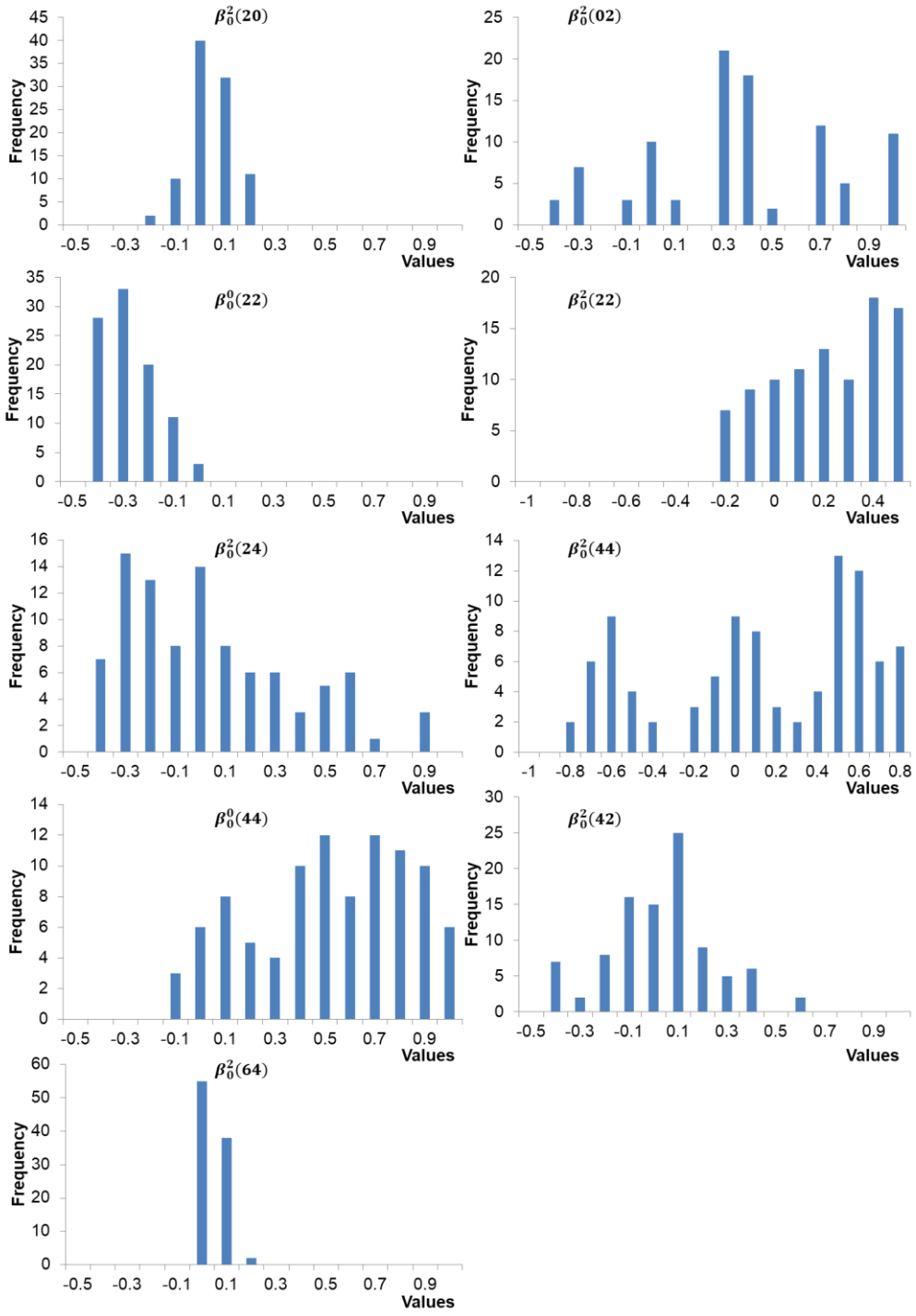

Figure 4.9: Distributions of bipolar moment values obtained directly from the Monte Carlo based forward convolution fit of the hypothetical case angular distributions.

In order to obtain fits with sharper bipolar moments values distributions, several attempts are made to “lock” some of the bipolar moments values to the true values while randomly generating the others for fitting. We noticed that as we increased the number of bipolar moments that are simultaneously “locked” during the Monte Carlo fitting, the bipolar moment distributions became sharper. An example is shown in Figure 4.10. In this case, the $\beta_0^2(20)$, $\beta_0^0(22)$ and $\beta_0^2(64)$ values are locked to be 0, -0.5 and 0, respectively, during the Monte Carlo search.

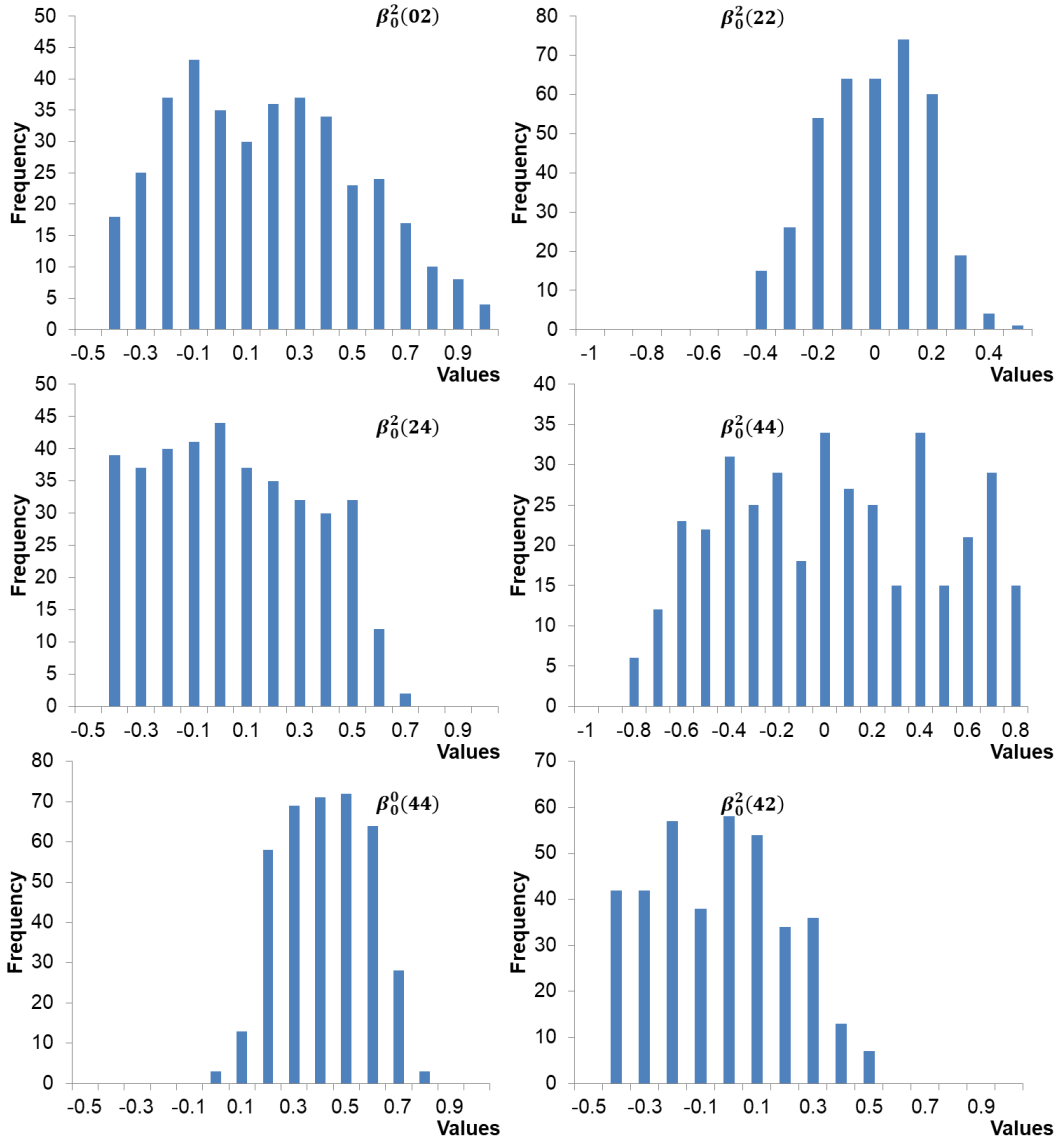

Figure 4.10: Distributions of bipolar moment values obtained directly from the Monte Carlo based forward convolution fit of the hypothetical case angular distributions. During this fit, the $\beta_0^2(20)$, $\beta_0^0(22)$ and $\beta_0^2(64)$ bipolar moments are constrained to their true values.

The reason for the wide distribution of bipolar moment values is that the full set of nine bipolar moments will form an underdetermined system. In the fittings we

demonstrated in this chapter, we usually simultaneously fit angular distributions from either two images (with VV detection geometries , one with S/O branch REMPI and the other with R/P REMPI) or three images (single rotational branch, each image with a different detection geometries VV, VH and HV). In both scenarios, all the fitted angular distributions can be fully determined by a set of six image anisotropy parameters β_k^{FG}. This means that the set of nine unknown bipolar moments is underdetermined by the six experimental image anisotropy parameters β_k^{FG}. Thus by constraining the values of three or more of the bipolar moments while floating others, the system becomes fully-determined and the distributions of bipolar moment values are sharper. Considering the fact that in real applications, constraining the bipolar moments is not always an acceptable approach, we suggest using the Monte Carlo method to search for linear combinations of limiting cases, instead of directly searching for all nine bipolar moments, because the limiting cases can lower the degrees of freedom of the bipolar moments.

The bipolar moment value distributions from the Monte Carlo method test on the hypothetical case also provide information about the sensitivity of the simulation on each of the nine bipolar moments. As discussed before, the $\beta_0^2(20)$, $\beta_0^0(22)$ and $\beta_0^2(64)$ values all had relatively sharp distributions of values. This means that the simulated angular distributions are generally more sensitive to these bipolar moments than the others. We also noticed that the $\beta_0^2(02)$ moment had a significantly wide distribution of values. In fact, the values span over almost the entire domain. This means that the simulated angular distributions are generally quite insensitive to the $\beta_0^2(02)$ moment. This can be rationalized by the fact that in the 2+1 REMPI Equations, the coefficients for the $\beta_0^2(02)$ moment are relatively small compared to those for the other bipolar

moments, especially those of the high order bipolar moments. This is not too surprising because for a two-photon REMPI process, the high order bipolar moments can play a significant role in the angular dependence of the probed signals.

As discussed above, the simulated angular distributions are generally less sensitive to the bipolar moments $\beta_0^2(22)$, $\beta_0^2(24)$, $\beta_0^2(44)$, $\beta_0^0(44)$. These bipolar moments resulting from the forward convolution methods generally have larger error bars when compared to low order moments like $\beta_0^2(20)$ and $\beta_0^0(22)$. Besides, $\beta_0^2(22)$, $\beta_0^2(24)$, $\beta_0^2(44)$ moments are not as physically intuitive, and thus do not lead themselves to easy a priori prediction for particular systems. Due to the lack of available experimental results for these moments, we are unable to evaluate the precision of these bipolar moments from our method. We have, therefore, not performed extensive analysis of the results for the higher order bipolar moments derived from our new method and we suggest caution should be used when interpreting the high order bipolar moments from our bipolar moments extraction methods.

We also examined the possible correlations among the bipolar moments, especially those involving the $\beta_0^0(44)$ moment, using the resulting sets of bipolar moments obtained by the Monte Carlo method when fitting the hypothetical case. No consistent evidence of correlations can be found between $\beta_0^0(44)$ and any other moment. However, we did realize that the $\beta_0^2(42)$ moment is consistently correlated to the $\beta_0^2(02)$ and $\beta_0^2(22)$ moments. We know that one high-*j* approximation for the $\beta_0^2(42)$ moment is given as:

$$\beta_0^2(42) = \frac{7}{12}\beta_0^2(02) - \frac{5}{12}\beta_0^2(22) \tag{4.3}$$

by calculating the $7/12\ \beta_0^2(02) - 5/12\ \beta_0^2(22)$ value for each set of bipolar moments and plotting them against the $\beta_0^2(42)$ values, we obtained the linear relations shown in Figure 4.11. The linear relation indicates that

$$-\beta_0^2(42) = \frac{7}{12}\beta_0^2(02) - \frac{5}{12}\beta_0^2(22) \tag{4.4}$$

which is reasonable because based on Equation (4.3), the non-zero sum of $\beta_0^2(02)$ and $\beta_0^2(22)$ moments combination will be compensated by the $\beta_0^2(42)$ moment values and the overall result is the true value 0.

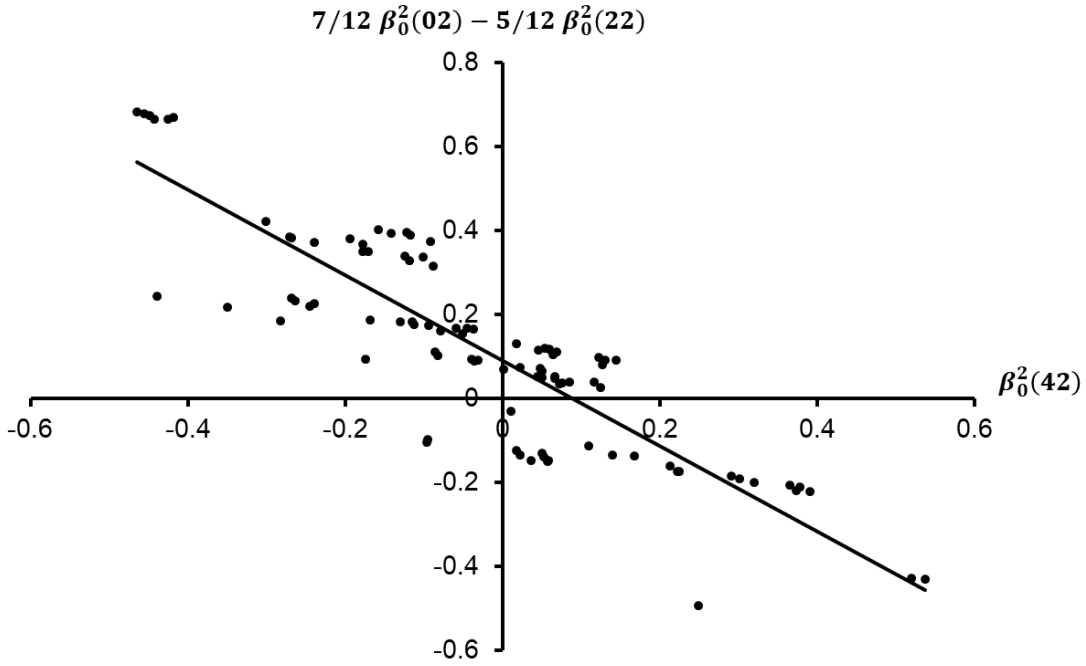

Figure 4.11: The correlation between the $\beta_0^2(42)$, $\beta_0^2(02)$ and $\beta_0^2(22)$ moments.

We also noticed that the $\beta_0^2(64)$ moment is consistently correlated to the $\beta_0^2(24)$ and $\beta_0^2(44)$ moments. The high-j approximation for the $\beta_0^2(64)$ moment is given as:

$$\beta_0^2(64) = \frac{11}{14}\beta_0^2(24) - \frac{3}{14}\beta_0^2(44) \quad (4.5)$$

However, by calculating the $11/14\,\beta_0^2(24) - 3/14\,\beta_0^2(44)$ value for each set of bipolar moment and plotting them against the $\beta_0^2(64)$ values, we did not find the similar result like Figure 4.11. The reason is still unclear.

CHAPTER V

PHOTODISSOCIATION DYNAMICS OF OCS NEAR 214 NM*

Carbonyl sulfide (OCS), the most abundant sulfur containing compound in the atmosphere,[101] is emitted into the troposphere by both biogenic and anthropogenic sources. The burning of biomass and natural gas and the oxidation of dimethyl sulfide and carbon disulfide account for the majority of OCS production.[102, 103] OCS is relatively inert with a global lifetime of 3.7 years in the troposphere, resulting in partial transport to the stratosphere where the lifetime is 63±15 years,[104, 105] with photolysis as the major loss pathway. The UV absorption spectrum of OCS shows a broad Gaussian-like peak near 223 nm with weak vibrational structure.[106-110] An absorption spectrum is shown in Figure 5.1. The lowest energy levels in linear OCS are the ground $^1\Sigma^+$ state and the excited $^1\Sigma^-$ and $^1\Delta$ states. Transitions from the ground state to $^1\Sigma^-$ and $^1\Delta$ states are forbidden by symmetry for linear OCS. Upon bending, the $^1\Sigma^+$ state becomes $1^1A'$ (called X by Schmidt *et al*,[111] whose naming we will follow). The $^1\Sigma^-$ state becomes $1^1A''$ (B) on bending, and the $^1\Delta$ state splits into a Renner-Teller pair $2^1A'$ (A) and $2^1A''$ (C). The A and B states have shallow wells at bent geometries, and dissociate directly. The C state and the very similar $2^3A''$ (c) state have deep wells at linear or nearly linear geometries and are quasibound. Transitions in bent OCS from the ground state to the A and B states contribute the smooth main part of its first absorption band, and Schmidt et al. concluded that transitions to C and c produce the superimposed vibrational

---

* Reprinted from "W. Wei, C. J. Wallace, G. C. McBane and S. W. North, The Journal of Chemical Physics 145 (2), 024310 (2016) ", with the permission of AIP Publishing.

structure.[111] The recent experimental study of OCS photodissociation at 210 nm showed that the triplet c ($2^3A''$) state can significantly contribute to the dissociation dynamics.[112]

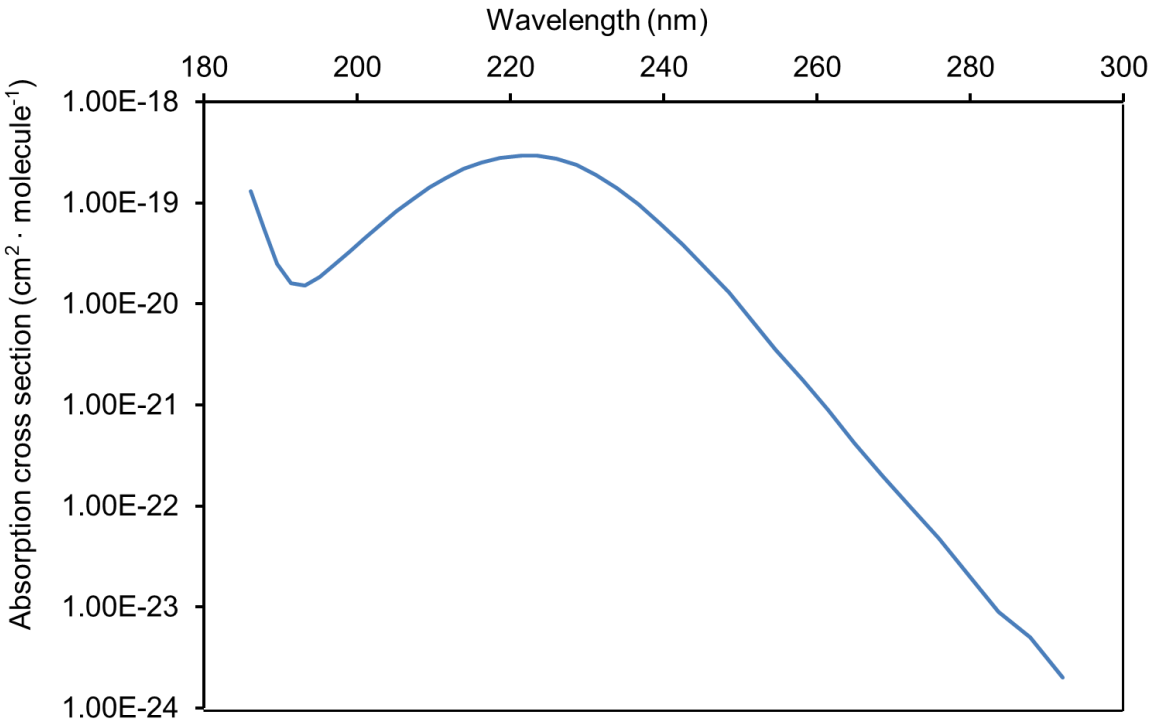

Figure 5.1: Absorption cross section (in logarithmic scale) as a function of wavelength for OCS at 225 K. Data adapted from Sander *et al*. [113]

There are two sulfur product channels in OCS photodissociation,

$$OCS(^1\Sigma^+) \rightarrow CO(^1\Sigma^+, v, j) + S(^1D_2) \quad (5.1)$$

$$\rightarrow CO(^1\Sigma^+, v, j) + S(^3P_J) \quad (5.2)$$

with the singlet channel (1) dominant at all wavelengths studied. At 222 nm, approximately 94% proceeds to the singlet channel.[114] We examine the singlet pathway in the present work.

The CO bond length is only 3% shorter in CO than in OCS, and the dissociation produces a cold CO vibrational state distribution. Sivakumar et al. observed no vibrationally excited CO following photolysis at any of 222, 235, and 248 nm and gave upper limits of 2% v=1 at 222 nm and 6% at 235 nm.[115] Sato et al. also detected no v>0 CO.[116] Rijs et al. did detect a small amount of v=1 CO at 230 nm, but did not give a quantitative estimate of the branching ratio.[117] Lee et al. saw hints of vibrationally excited, possibly including v=4, CO following 193 nm dissociation.[118]

Strong bending forces on the A and B state surfaces during the dissociation result in rotationally excited CO fragments. Sivakumar *et al*. were the first to observe the highly excited and bimodal rotational state distribution at 222 nm, with a main peak at *j*=56 and a subsidiary maximum at *j*=67.[115] Subsequent work by other groups showed that the bimodal character persists for photolysis wavelengths between 248 and 193 nm.[95, 115-119] As the excitation energy increases, the higher-j peak becomes more pronounced, both components of the rotational distribution shift to higher *j,* and the spacing between the two components diminishes. By 217 nm the two rotational distributions partially coalesce,[116] and at 193 nm the high-J peak is the largest.[118] At 288 nm in the far red wing of the absorption band, little excess energy remains for rotational excitation.[120]

Product angular distributions $I(\theta)$ have been reported at several dissociation wavelengths.[95, 114-116, 118-123] These are characterized by the spatial anisotropy parameter β according to $I(\theta) \propto 1 + \beta P_2(\cos\theta)$ where P_2 is the second Legendre polynomial and θ

is the angle between the outgoing fragment velocity and the polarization vector of the photodissociating light.[31, 81] For dissociation of bent but rotationless OCS, absorption to an A″ state will necessarily produce $\beta = -1$, while absorption to an A′ state may produce any value of β between 2 and -1 depending on the orientation of the transition dipole in the molecular plane and the extent of non-axial recoil. Most experiments indicate that β generally increases with CO rotational state, from relatively small positive values at the lowest populated *j* state to near the limiting value of 2 in the upper part of the rotational distribution. At 288 nm the slightly lower-energy B state dominates the absorption and $\beta \approx -0.7$.[120]

Sivakumar *et al*. also measured the CO rotational alignment, the distribution of CO angular momentum vectors **j** with respect to the polarization vector **μ** of the photolysis light.[115] The **μ-j** correlation is the experimental observable best suited to distinguish between products formed via A′ or A″ state excitation. Conservation of angular momentum constrains **v** to be perpendicular to **j** for photodissociation of a *j*=0 triatomic molecule. Since **μ** lies in the OCS plane for the A′ state excitation, **μ** and **j** must be perpendicular, while for the A″ state excitation **μ** and **j** must be parallel. Therefore, determination of the **μ**-**j** correlation can provide quantitative information regarding the relative contributions of the two product channels. Sivakumar *et al*. made the only previous measurements of this quantity for OCS, at 222 nm, and used them to estimate the fractional contributions of different electronic states as a function of product rotational state.[115] In this work we report new measurements of CO rotational alignment for dissociation near 214 nm.

The current understanding of OCS photodissociation dynamics in the first absorption band indicates that absorption to the A and B states play roughly

comparable roles in the lower part of the rotational distribution,[96, 115, 119] while the upper part is contributed by absorption to the A state followed by non-adiabatic transitions to the ground state. Non-axial recoil is important for both A and B state dissociations. The transition moment for the A-state absorption, which must lie in the triatomic plane, is displaced from the OCS axis by 30-40 degrees, compensating for non-axial recoil and yielding β parameters near 2 despite its presence.[96, 123] Absorption to the B state necessarily produces β=-1 for nonrotating OCS. The variation in β across the lower part of the rotational distribution reflects the relative contributions of the A and B states and their slightly different rotational distributions. The crucial transition dipole functions are relatively difficult to calculate accurately with electronic structure methods,[111] and the relative contribution of A and B states has therefore been the slowest part of the dynamical picture to come to consensus.

In this work we report experimental product state distributions, angular distributions, and rotational alignments for OCS photodissociation dynamics near 214 nm, extending previous similar measurements to shorter wavelength. The rotational distributions of the CO product for both v=0 and v=1 measured using 2+1 REMPI are bimodal but only partially resolved, reflecting the merging of the two rotational components that are resolved at longer wavelength. S($^1D_2$) images were collected to confirm the CO rotational distributions. The spatial anisotropy distribution obtained from the S($^1D_2$) image indicates that β increases in value from low j to high j, consistent with results at longer wavelength. CO fragment vector correlations including rotational alignments confirm that both $2^1A'$ and $1^1A''$ absorptions contribute to the low j component while the $2^1A'$ state is the main contributor to the high j component. Most of

the experimental results agree satisfactorily with corresponding surface-hopping calculations.

Product Internal State Distributions

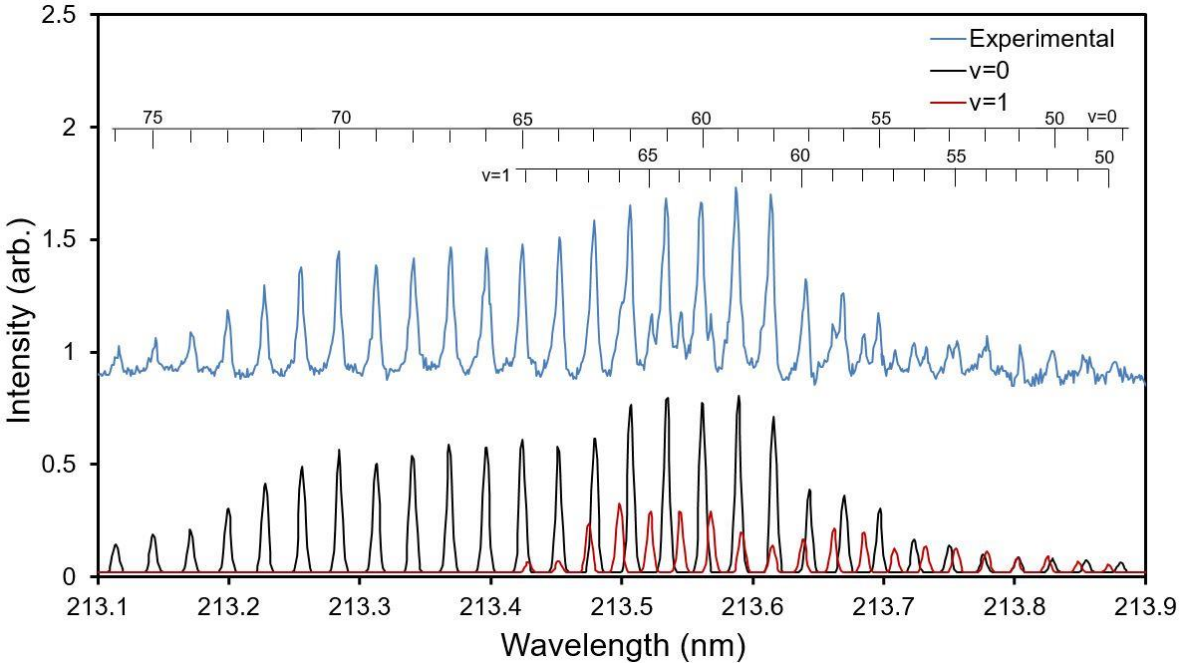

Figure 5.2: 2 + 1 REMPI scan of the CO S-branch from the one color photodissociation of OCS. The experimental data (upper trace) shows the clearly resolved v=0 and v=1 components. Simulated spectra for the v=0 (black) and v=1 (red) contributions are shown below. Figure reproduced from Wei *et al*. JCP, 145, 024310 (2016). [65]

A representative experimental 2+1 E-X REMPI scan of the CO fragment arising from OCS photodissociation near 213.5 nm is shown in Figure 5.2. Two-color imaging experiments probing the S($^1D_2$) fragment indicated that the small change in dissociation

wavelength, over a region similar in range to that of Figure 5.2, did not yield measurably different CO rotational populations. We therefore believe that the one-color measurements can be used to determine the CO rotational distribution over the narrow range of wavelengths employed. In the CO REMPI spectrum there are two clear sets of peaks corresponding to transitions associated with the (0,0) and (1,1) bands. The simulated (0,0) and (1,1) bands are shown as black and red respectively in the lower panel of Figure 5.2. The observed rotational states range from *j*=48-76 for the (0,0) band and *j*=50-69 for the (1,1) band. Quantitative comparison of the simulated REMPI spectrum with the experimental data required optimization of spectroscopic constants in order to obtain reasonable fits for both transitions. The spectroscopic constants were determined by fitting the peak positions to

$$E_{h\nu} = [T_{vv} + B'_v j'(j'+1) - D'_v j'^2 (j'+1)^2] - [B''_v j''(j''+1) - D''_v j''^2 (j''+1)^2] \quad (5.3)$$

The initial B_v'', D_v'', B_v', D_v', T_{00} for v=0 and v=1 were taken from Baker *et. al*.[124] T_{11} was calculated by taking the difference of T_{10} from Baker *et al*.[124] and v_0 from Plyler *et al*.[125] Using these values as a starting point, all of the parameters were optimized resulting in effective spectral constants for the X and E states. The final values used in the spectral simulations are shown in Table 5.1.

Table 5.1: The spectroscopic constants used to both fit the CO 2+1 REMPI spectra and simulate the sulfur speed distribution. All values reported are in cm^{-1}.

	B_v''	D_v''	B_v'	D_v'	T_{vv}
v=0	1.8889	$5.477x10^{-6}$	1.9312	$5.908 x10^{-6}$	92929.95[124]
v=1	1.8924	$6.1244x10^{-6}$	1.9261	$7.1526x10^{-6}$	92939.7*

*T_{11} was calculated by taking the difference between T_{10} (95081.9 cm^{-1}) from Baker *et al*.[124] and v_0 (2143.2 cm^{-1}) from Plyler *et al*.[125]

Simulations of the REMPI of the (0,0) and (1,1) bands are shown with solid black and red lines, respectively. Several of the peaks associated with the individual vibronic bands overlap in the spectrum, making a determination of relative intensities difficult. In order to determine the relative populations of the overlapping peaks, we collected CO ion images at wavelengths corresponding to the overlapping states: at 213.458 nm (*j*=64 v=0 and *j*=68 v=1), 213.478 nm (*j*=63 v=0 and *j*=67 v=1), 213.615 nm (*j*=58 v=0 and *j*=61 v=1) and 213.641 nm (*j*=57 v=0 and *j*=60 v=1). The relative intensity from each overlapped feature is obtained by integrating the intensity of each contribution. The non-overlapped v=0 and v=1 transition peaks were fit directly. The overall v=1 population is estimated based on the peak area of all the peaks from v=1 transitions over the sum of the peak areas from both the v=1 and v=0 transitions,

$$\mathrm{P(v=1)} = \frac{\sum_{j=0,v=1} \mathrm{I}(j)}{\sum_{j=0,v=0} \mathrm{I}(j) + \sum_{j=0,v=1} \mathrm{I}(j)} \tag{5.4}$$

The simulated spectrum is in good agreement with the experimental REMPI spectrum. The consistent trend of transitions rules out possibilities of isolated perturbations. The

Franck-Condon factors of (0,0) and (1,1) bands, computed using Morse potentials for the E and X states,[126] differ by less than 4%. However, a smooth competition between predissociation and ionization can still not be eliminated. A difference in ionization probability between v=0 and v=1 CO could affect the fraction of v=1 determined via Equation (5.4). No attempts are made to correct for these issues.

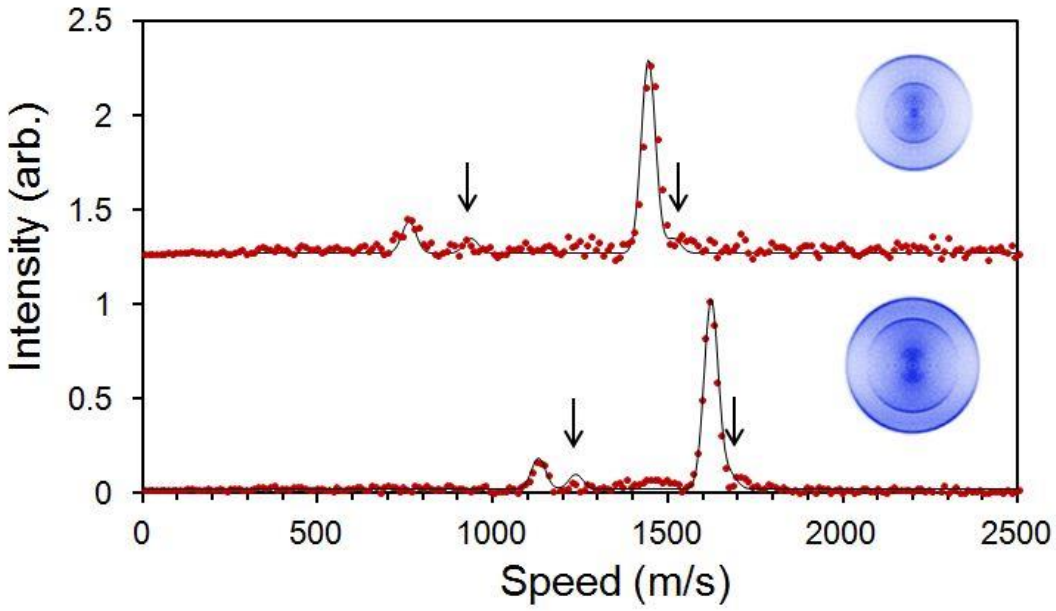

Figure 5.3: S branch CO ion images with their corresponding speed distributions and simulations at 213.478 nm on the left and 213.615 nm on the right. The inner rings originate from v=1 CO while the outer rings originate from v=0 CO. The top panel corresponds to *j*=63 for the outer ring and *j*=67 for the inner ring and the bottom panel corresponds to *j*=58 for the outer ring and *j*=61 for the inner ring. Filled circles are for the experimental speed distribution, while the solid lines show the simulated speed distribution. Minor contributions of CO products originating from vibrationally excited parent OCS are also shown and their locations are marked by arrows. Figure reproduced from Wei *et al*. JCP, 145, 024310 (2016).[65]

Figure 5.3 shows two images of one color dissociation at wavelengths corresponding to the overlapping states. Features corresponding to CO (v=0, *j*) (outer ring) and CO (v=1, *j*) (inner ring) products are clearly resolved. The ion images shown have been symmetrized and their corresponding speed distributions (filled circles) from reconstructed images are also shown in Figure 5.3. The relative contributions of v=0 and v=1 to each overlapped peak can be determined by integration of the corresponding features. In addition, the comparison of the speeds associated with the CO v=0 and v=1 components can be used to provide confirmation of the rotational state assignments. Gaussian peaks were used to simulate the speed distributions in Figure 5.3, using speeds derived from energy conservation. Based on this analysis we are confident of the final state assignments employed in the spectral simulations. In Figure 5.3, very weak features are observed near 1550 m/s and 1700 m/s consistent with vibrationally excited OCS parent (v_2=1) producing CO (v=0, *j*) fragments. Minor features corresponding to vibrationally excited parent are also present for the v=1 CO product channel. The simulated v=1 CO product originating from vibrationally excited parent OCS appears at 950 m/s and 1250 m/s for the upper and lower images respectively. Previous studies[95, 120, 123, 127-129] have observed contributions from the photodissociation of vibrationally excited OCS, which are most pronounced at the highest CO rotational states, suggesting that initial parent bending leads to greater final CO rotation. Our observations are consistent with these reports. Based on the intensities of the rotational lines, we find a v=1 contribution of approximately 21% which is larger than the theoretical prediction of 13.2%.[96] The values reported here are from trajectories including surface hopping, while those reported in McBane *et al*.[96] are from quantum calculations without coupling to the ground state.

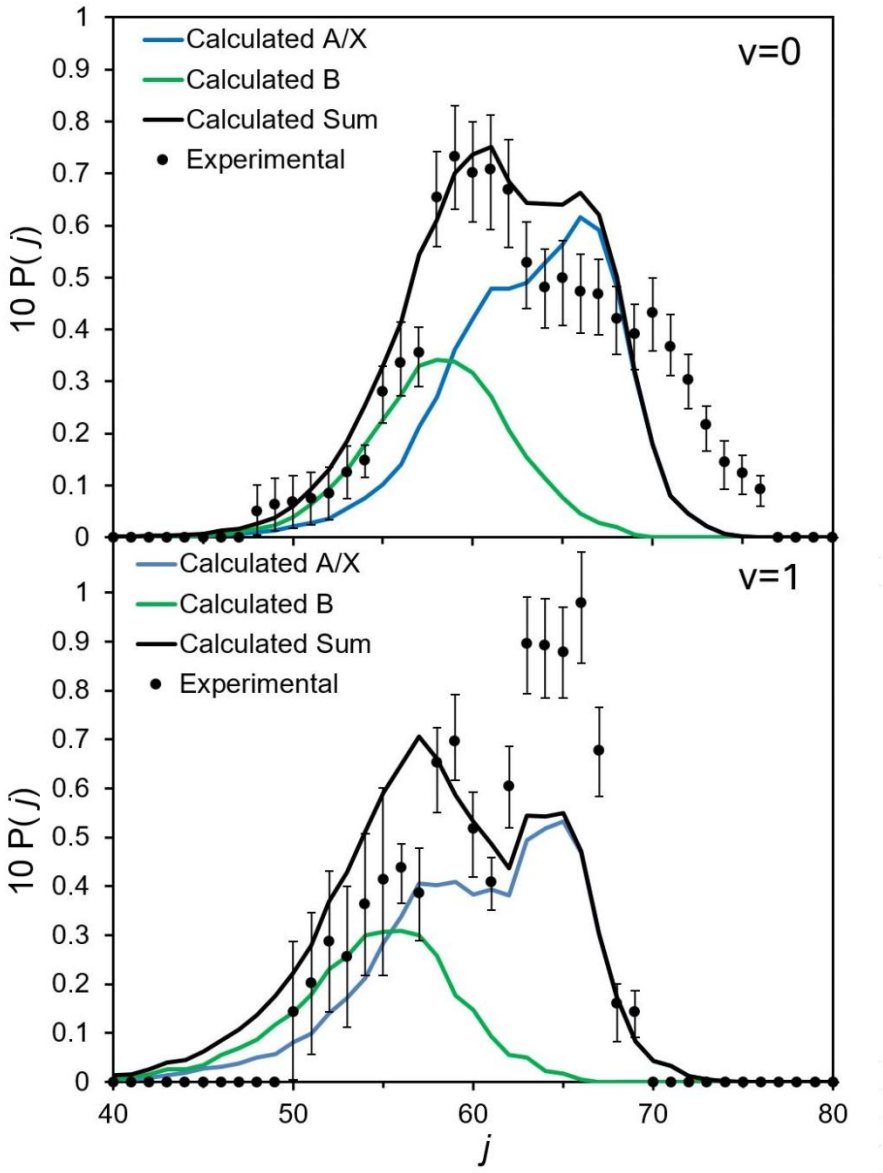

Figure 5.4: CO Rotational distributions associated with v=0 (upper panel) and v=1 (lower panel). In both panels, the experimental data are shown with filled circles and compared to the results of classical trajectory calculations (solid lines). The computed contributions from the A/X and B pathways are shown with blue and green lines respectively for both v=0 and v=1 CO products. The rotational populations have been normalized and scaled. Figure reproduced from Wei *et al*. JCP, 145, 024310 (2016).[65]

Figure 5.4 shows the CO rotational distributions from photodissociation near 214 nm. The experimental population for each CO rovibrational state was obtained from the fitted 2+1 REMPI spectrum shown in Figure 5.2. The experimental rotational populations have been normalized and are compared to classical trajectory/surface hopping calculations. The computed population contributions to each CO vibrational state from the A/X and B pathways are also shown. The A/X component includes any product that originated in the $2^1A'$ state, while the B pathway is for products from the $1^1A''$ state. Previous studies at longer wavelengths reported a clear bimodal distribution. At wavelengths near 214 nm, however, the two components have almost coalesced, although there are clearly two features present. For v=0 products, the lowest rotational state observed is *j*=48. The results from the trajectory calculations match the maximum in the experimental population distribution, although there are some differences at the highest states. The calculations overestimate populations near *j*=65 and underestimate those for *j*>70. The experimental CO v=1 rotational distribution is qualitatively in agreement with calculated results and the shift of the distributions to lower *j* is well reproduced. The rotational population starts at higher *j* and ends at lower *j* than the v=0 rotational distribution. If we lower the 1^1A" (B) state rotational population contribution, or even remove the 1^1A" (B) state contribution, the adjusted computational rotational distribution can fit the experimental results much better. This fit is also supported by preliminary experimental measurements of vector correlations of v=1 CO fragments from the North group.[130]

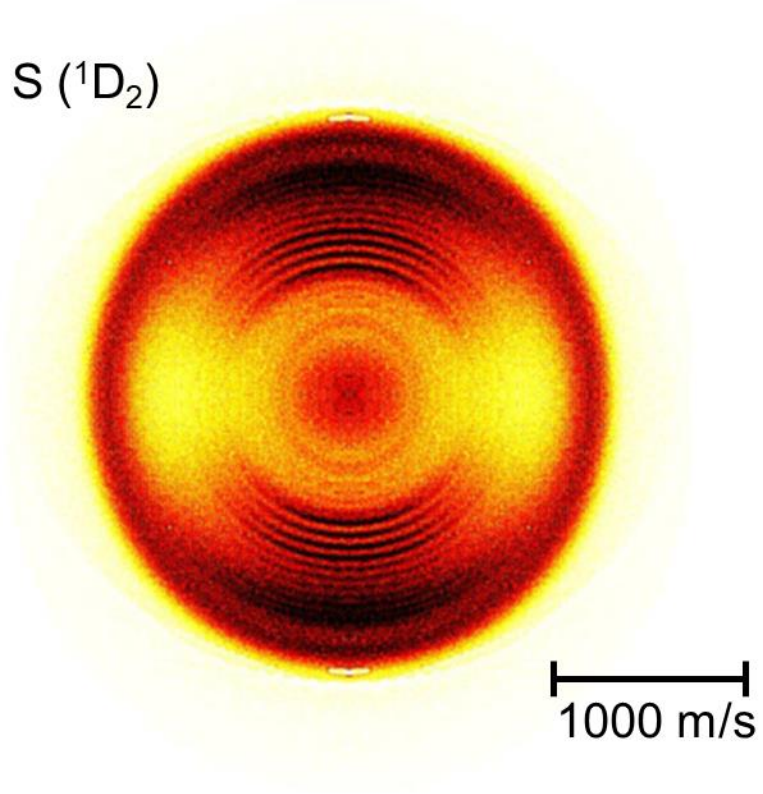

Figure 5.5: A DC sliced S($^1D_2$) ion image arising from OCS photodissociation at 214.2 nm with a VH geometry. Figure reproduced from Wei *et al*. JCP, 145, 024310 (2016).[65]

In order to confirm the rotational distribution derived from the CO REMPI, we collected ion images of the S($^1D_2$) fragment. Both DC sliced and crushed images were obtained and analyzed. Figure 5.5 shows a typical DC sliced S($^1D_2$) image arising from OCS photodissociation at 214.2 nm with a vertically polarized pump laser beam and a horizontally polarized probe laser beam. The clear ring-pattern structure in the image corresponds to specific rotational states of the coincident CO fragment due to energy conservation, given by

$$\mathrm{E_{avail}} = \mathrm{h}\nu - \mathrm{D_{00}} + \mathrm{E_{int}(OCS)} = \mathrm{E_{int}(CO)} + \mathrm{E_{int}(S)} + \mathrm{E_{trans}} \quad (5.5)$$

where E_{avail} is the available energy of photochemical products; $h\nu$ is the dissociation photon energy; D_{00} is the dissociation energy of OCS; $E_{int}(OCS)$, $E_{int}(CO)$, $E_{int}(S)$ are internal energy of OCS, CO, and S respectively; and E_{trans} is the translational energy of two fragments. We employed a value of D_{00} of 34641 cm^{-1} based on the work of Komissarov *et al*.[80] The S($^1D_2$) speed distribution derived from Figure 5.5 is shown in Figure 5.6.

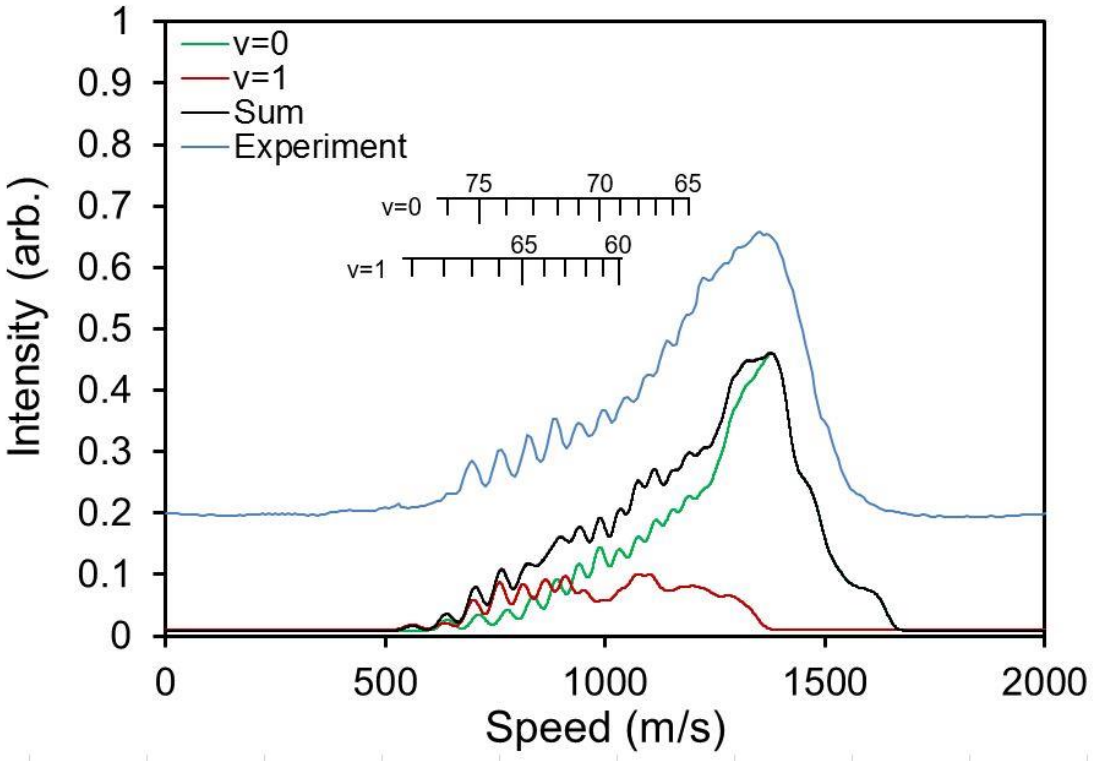

Figure 5.6: The speed distribution derived from the DC sliced S($^1D_2$) image shown in Figure 5.5. The simulation consists of two components based on the rotational distributions from the REMPI spectrum, v=0 in green and v=1 in red. The v=1 population of 21% is shown which was obtained from the REMPI spectrum. Figure reproduced from Wei *et al*. JCP, 145, 024310 (2016).[65]

The CO vibrational distribution can also be extracted from the sulfur images. Forward convolution simulations (solid black) using the optimized CO rotational state distributions for both the v=0 (green) and the v=1 (red) components derived from the CO REMPI spectra are shown in Figure 5.6. The ratio between the v=0 and v=1 states was adjusted in order to find the best fit to the sulfur speed distribution. The best fit, shown in Figure 5.6, resulted in a v=1 contribution of 21±8%, in excellent agreement with the result obtained from the REMPI spectrum.

The trajectory calculations predict that the v=1 population should be small but increase as the wavelength becomes shorter. The calculated populations in v=1 from McBane *et al*. are 2.3%, 2.7%, 4.7, 13.5%, and 13.2% at 248, 235, 230, 222, and 214.5 nm respectively.[96] The values reported here are from trajectories including surface hopping, while those reported in McBane *et al*.[96] are from quantum calculations without coupling to the ground state. The calculations therefore underestimate the 214.5 nm vibrational population modestly.

The 21% v=1 population found here is more surprising because of its discordance with experimental results at other wavelengths. Several groups[116, 117] have detected CO following 230 nm dissociation using 2+1 REMPI through the B state; it is not too surprising that most of those experiments did not observe highly rotationally excited CO, since the B state is predissociated in v=1 above *j*=17, and more strongly predissociated above *j*=37.[131] Rijs et al., using the same technique with photoelectron detection, did see a very weak spectrum corresponding to the Q branch of the (1-1) band.[117] The absence of rotational resolution in that spectrum, while the spectroscopically similar (0-0) band nearby was fully resolved, further indicates that predissociation at high *j* limits the sensitivity of the B-X REMPI probe. The 217 nm

experiment of Sato et al. used CO REMPI through the C state on a Q branch.[116] In that spectrum the (1-1) band can be expected to be hidden under the (0-0) band, except for the j<50 tail of the v=1 rotational distribution. In fact there is a small tail extending to lower *j* in their published spectrum between 217.45 and 217.5 nm that may well be the (1-1) band. However, the 222 nm experiment of Sivakumar et al, using one-photon laser induced fluorescence through the A state, should have been sensitive to v=1 CO, and that group found no v=1 during "extensive searches".[115]

Several other groups[95, 119, 123, 129, 132] have depended on REMPI of the sulfur atom, and extracted CO internal state distributions from the sulfur speed distributions. In those experiments it is hard to identify v=1 unless the sulfur speed distribution is fully rotationally resolved, as is evident in Figure 5.6; the slower atoms correlated with v=1 tend to merge with similarly slow atoms coincident with higher rotational levels in v=0.

In our experiment, predissociation or dissociative ionization of the E state during REMPI detection are also possibilities; these effects have been reported at $j \leq 31$.[67, 68, 124] The C^+ yield from CO^+ is j-state dependent and is not negligible near $j=20$. However, the influence of predissociation or dissociative ionization at $j>50$ has not been reported. Attempts were made to search for C^+ but no signal was detected, so we conclude that the yield of C^+ is unlikely to be significant. The v=1 level in the E state is more likely than v=0 to suffer these effects so they would probably cause an underestimate, rather than an overestimate, of the v=1 population.

We conclude that the branching ratio into v=1 changes substantially between 222 and 214 nm. Our trajectory calculations, and the quantum calculations reported in McBane *et al*.[96], do suggest a fairly steep rise (a factor of about 3) in the v=1 population between 230 and 222 nm. One possibility is that the steep rise does occur, but at

somewhat shorter wavelengths, so that the small v=1 population at 222 nm was below the detection limit of the LIF experiment but the v=1 yield rises to more than 14% by 214 nm.

Evidence against this hypothesis is that preliminary, unpublished two-color experiments have detected substantial v=1 product from 230 nm photolysis using the 214 nm E-state probe technique. Figure 5.7 shows a representative image from the two color experiments. By calculating the speed from energy conservation, the four rings shown in this image can be interpreted. The outer two rings came from 213.804 nm photodissociation, probed by the same wavelength. The inner two rings came from 230.2 nm photodissociation, probed by the 213.804 nm laser. The v=0 and v=1 component of the CO E-X S branch REMPI overlap at this probe wavelength. Thus the outer most ring came from ground vibrational CO (j=51) and the one inner to it came from vibrationally excited CO (j=53). Similarly, the second to the most inner ring came from ground vibrational CO (j=51) and inner most ring came from vibrationally excited CO (j=53). This clear signal of the inner most ring demonstrated that vibrationally excited CO fragments from 230 nm photodissociation exist and the vibrationally excited CO branching ratio at 230 nm is probably higher than previously believed.

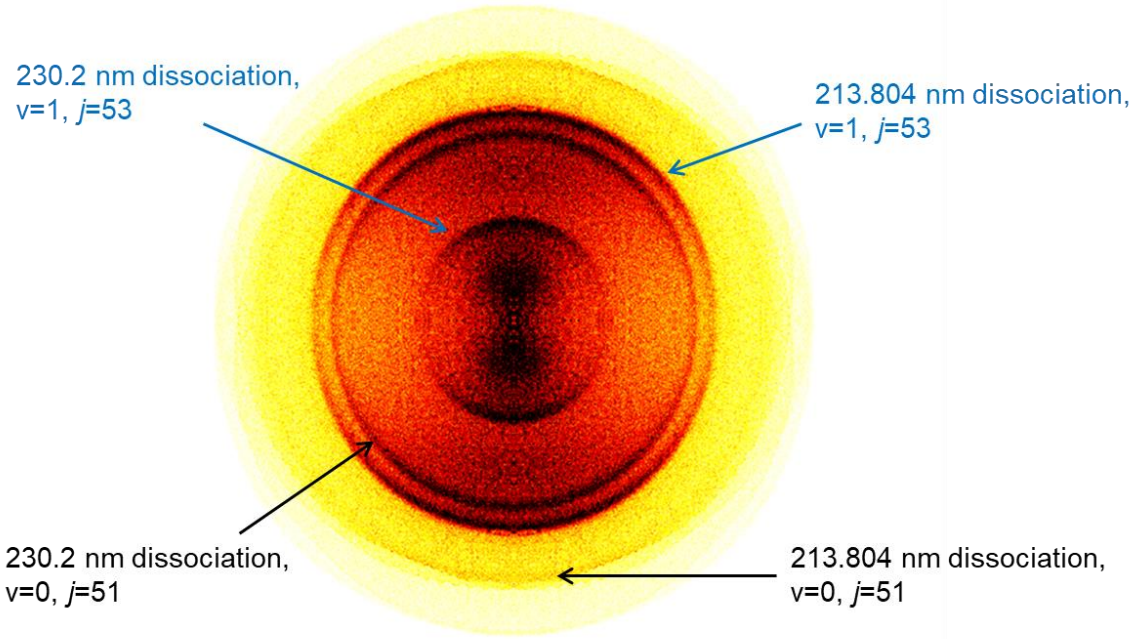

Figure 5.7: A crushed CO ion image probe by S branch E-X REMPI, arising from both OCS photodissociation at 214 nm and at 230 nm with a VV geometry.

Given the surprising inconsistencies among the different observations we must regard the wavelength dependence of the product vibrational distribution as an open question warranting further investigation. Our experiments clearly indicate that 214 nm dissociation produces a non-negligible amount of v=1 CO.

Computed Rotational Distributions and Interpretation

The computational chemistry calculations are conducted by Dr. George C. McBane.

The classical calculations were carried out as described in references by McBane *et al*.[96, 133], using the empirically modified adiabatic surfaces for the A and B states described earlier[96]. Schmidt and Olsen recently found, using a two-dimensional study with accurate electron correlation methods, that the empirical modification to those surfaces was at least qualitatively reasonable.[134] As in McBane *et al*.[96], the total energy was reduced by 0.1 eV in order to compensate for unphysical distribution of the CO zero point energy into product rotation. To model photodissociation at 214.5 nm from the ground state of OCS whose zero point energy is 0.245 eV, initial conditions were therefore selected to have total energies within 0.01 eV of 5.925 eV. Composite properties arising from trajectories on both A/X and B states were computed as described in Section V.A of McBane *et al*.[96], using a cross section ratio σ_A/σ_B=2.0 for 214.5 nm.[135]

Non-adiabatic coupling between the A and X surfaces was modeled with the trajectory surface hopping method of Tully,[136, 137] using only the γ component of the nonadiabatic coupling vector. Total energy was conserved at hops by distributing the change in potential energy "democratically" among the three Jacobi momenta, because this approach was found to be preferable for computation of angular distributions.[133]

When the rotational distribution is compared to those at longer wavelengths, a consistent trend appears: with decreasing photolysis wavelength the two channels merge together, the high *j* component increases in intensity, and the rotational distribution moves to higher *j*. Our rotational distribution shows a higher contribution from the $2^1A'$ channel than Sato *et al*. found at 217 nm.[116] The higher *j* product channel (from pure $2^1A'$ state) at 217 nm is still relatively low in intensity compared to the lower *j* channel (from a mixed contribution of both $2^1A'$ and $1^1A''$ states). In the present work at

214 nm the higher *j* component shows comparable intensity to lower *j* components. Dissociation at 217 nm yields a rotational distribution that peaks at *j*=58 and *j*=65, while this work shows peaks at *j*=60 and 70. Trajectory calculations suggest that both of these differences are due to the shape of excited state potential energy surface. The rotationally excited products are the result of simultaneous bond breaking and bending. The molecule starts on the excited state surface in a nearly linear configuration, with γ of just a few degrees, while the A and B states have minima near γ=48° and 38° respectively. During the dissociation the bending potential applies a torque that increases γ (and its time derivative *j)* until the minimum is reached; after that, the potential serves to slow the rotation. The differences in dissociation wavelength result in different starting points for the trajectories on the excited state surface, which eventually result in different deceleration forces on the OCS bending. As the wavelength of excitation decreases, excited state molecules start in regions with higher bending forces and the deceleration effect becomes less pronounced, resulting in products with more rotational excitation. The non-adiabatic crossing from the $2^1A'$ (A state) to the $1^1A'$ (X state) takes place just after the bending of OCS reaches the "deceleration region", so that molecules making that transition retain the high rotational angular momentum they acquired in the initial stages of the dissociation.

The left panels in Figure 5.8 show "phase space plots", *j(t)* vs. *γ(t)*, for 15 randomly selected trajectories beginning on the A state at 230 and 214 nm. The first hop from A to X is marked with a dot; segments of each trajectory on the X state are plotted in red. The surface hops fall into "early" and "late" groups because of the coordinate dependence of the nonadiabatic coupling.[111] At both wavelengths, trajectories that make early hops and remain on the X state are decelerated less than

those that complete most of the trajectory on the A state. The early-hop groups therefore finish with higher *j* on average. At 230 nm, the early-hop trajectories are clearly segregated from the others that hop late or not at all, while at 214 nm the separation is not as clear because the A-state-only trajectories are not as strongly affected by the angular decelerating force. The right panels give the rotational distributions from the complete trajectory sets, separated into sets that do make an early hop and those that do not. The merging of the pure-A component and the non-adiabatic A-X components of the rotational distribution with decreasing wavelength is clear. Some trajectories make an early hop to X but hop quickly back to A; those still feel the decelerating force and are the source of the “tail” that extends to lower *j* in the early-hop rotational distribution.

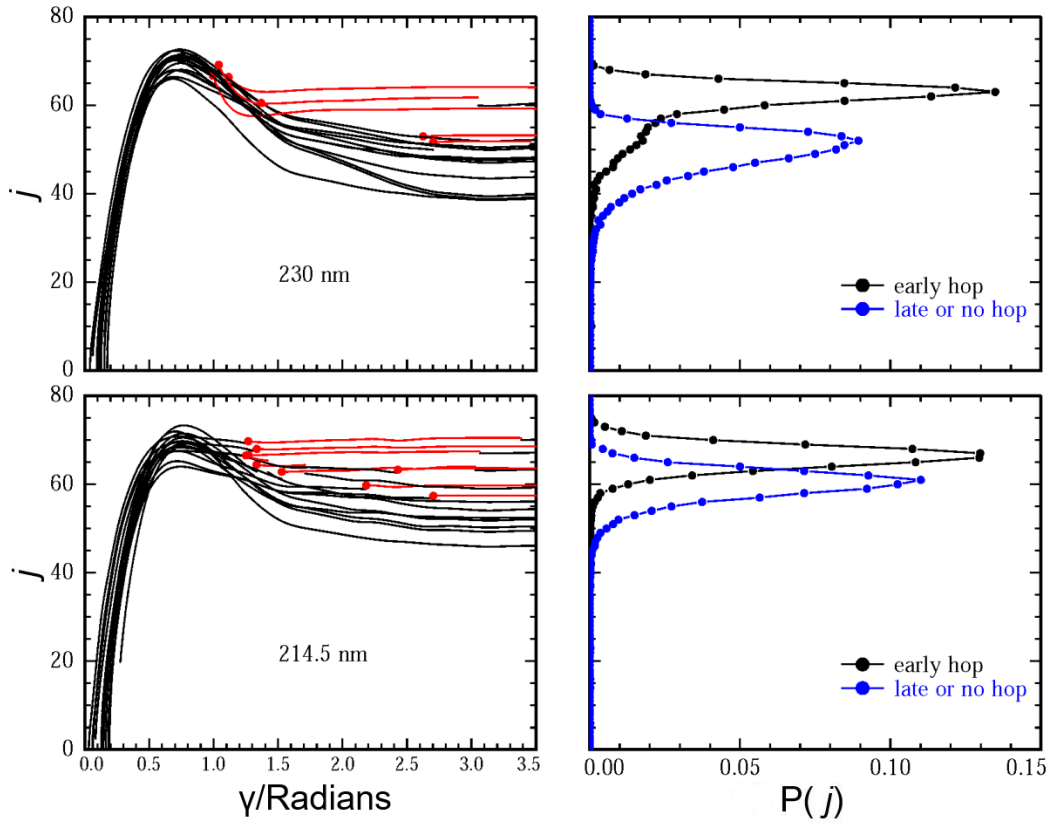

Figure 5.8: Computational chemistry calculation results. Left panels: Individual trajectories begun on the A state and propagated with the possibility of surface hopping to X, plotted in (*γ,j*) coordinates. Portions of each trajectory on the A state are in black and on the X state are in red, with the first hop from A to X indicated with a red dot. Right panels: rotational distributions from the entire trajectory set (50,000 trajectories at each wavelength), divided into two groups that did or did not hop from A to X while *γ*<1.7. Figure reproduced from Wei *et al*. JCP, 145, 024310 (2016).[65]

Vector Correlations and Contributions of $2^1A'$ and $1^1A''$ States

We collected a series of CO images to determine the *j*-dependent relative contribution from the $2^1A'$ and $1^1A''$ states. Figure 5.9 shows three CO images acquired using R-branch transitions that display distinct anisotropy. On the leftmost image, the outer ring corresponds to *j*=57, v=0 and shows weak four-fold symmetry, with extra

intensity at the 90 degree image angle. In contrast, the image from *j*=71, v=0 shows more pronounced four-fold symmetry, with very low signal intensities at 90 degrees. The image from *j*=62, v=0 shows intermediate anisotropy. Image anisotropies result from linear laser polarization and fragment vector correlations. The linear polarization provides laboratory frame alignment with the transition dipole moment and preferential detection of rotational angular momentum vectors. Changes in the image anisotropies from low *j* to high *j* CO images quantitatively reveal changes in vector correlation.

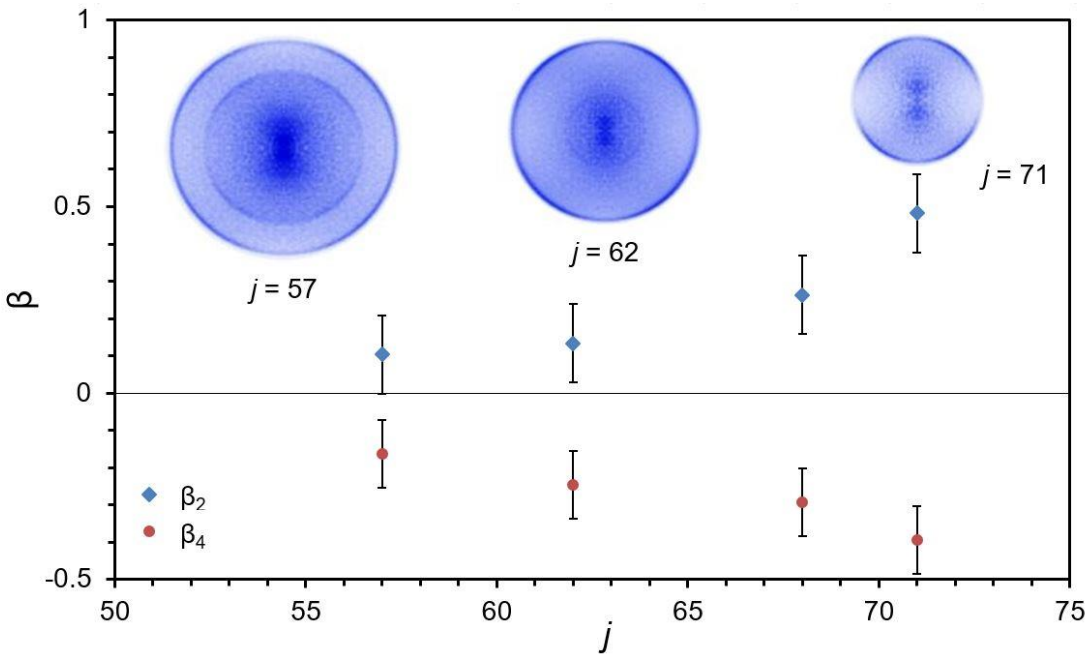

Figure 5.9: R branch CO (v=0) images from different rotational states. The insets show the corresponding image anisotropy parameters. From left to right images are taken at 214.291 nm, 214.18 nm, and 214.027 nm. Figure reproduced from Wei *et al*. JCP, 145, 024310 (2016).[65]

Angular distributions were extracted from each image by integrating the intensity over a narrow radial range (5-8 pixels) around the outer edge of each crushed image. Image anisotropy parameters β_k^{FG} are extracted from the measured images and the results are also shown in Figure 5.9.

j dependent bipolar moments can be calculated from these image anisotropy parameters.[43, 82, 83] We have applied the 2+1 REMPI Equations to conduct direct inversion and extract full sets of bipolar moments from S and R branch image pairs at *j*=58, 62 and 71 (v=0) to study the *j*-dependence of the vector correlations. The results are given in Table 5.2.

Table 5.2: Bipolar moments obtained from CO images. Table reproduced from Wei *et al*. JCP, 145, 024310 (2016).[65]

j	58	62	72
$\beta_0^2(02)$	0.03±0.13	-0.33±0.13	-0.49±0.13
$\beta_0^2(20)$	0.14±0.07	0.26±0.07	0.32±0.07

The alignment (**μ-*j***) bipolar moment $\beta_0^2(02)$ results, shown in Figure 5.10 along with the calculated prediction, are particularly important. For the dynamics of OCS photodissociation, the transition dipole moment for $2^1A'$ (A) state is in the OCS plane but not alone the C-S bond, while the one for $1^1A''$ (B) state is perpendicular to the plane. It is difficult to distinguish the $\beta_0^2(20)$ moment values between the $2^1A'$ (A) state and the $1^1A''$ (B) state. The **μ-*j*** correlation can serve as a clearer indicator of the two states. The $\beta_0^2(02)$ bipolar moment gives limiting values ranging from -0.5 if the

fragments are from 2^1A′ state OCS, to 1 if the fragments are from 1^1A″ state OCS. We find values close to the negative limiting case of $\beta_0^2(02)$ at high *j* which is consistent with pure 2^1A' state (**μ** perpendicular to **j**). At low *j* $\beta_0^2(02)$ is close to 0, reflecting a mixture of the 2^1A′ and 1^1A″ channels. A value of $\beta_0^2(02)$ near 0 indicates that the 2^1A' state contribution is greater than 50% since an equal contribution of the 2^1A' and 1^1A" states should yield a value of 0.25 for $\beta_0^2(02)$. The calculations predict the trend in $\beta_0^2(02)$ values accurately, but give too large an A″ contribution at lower *j*. The error could come either from inaccuracy in the computed transition moments or in the rotational distributions predicted for the A and B states. Both problems may be present but the second is likely to be the main cause of the discrepancy. The potential energy surfaces used were empirically modified to give good rotational distributions at 235 nm, and we may expect errors in their predictions that grow as the dissociation wavelength moves farther from that "anchor" point.

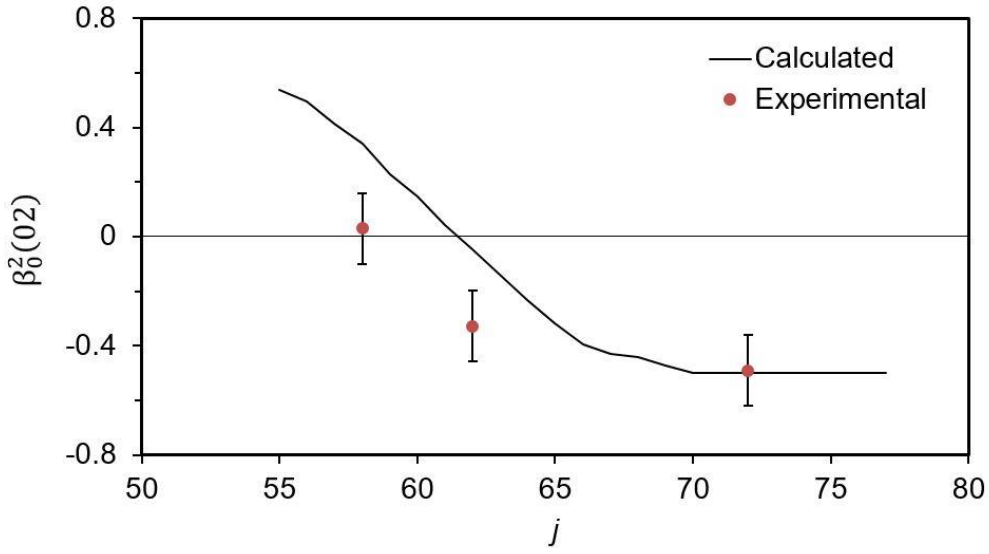

Figure 5.10: The $\beta_0^2(02)$ bipolar moment for different rotational states. The experimental values are represented by the filled circles at *j*=58, 62, and 72. The calculation is represented by the black line. Figure reproduced from Wei *et al*. JCP, 145, 024310 (2016).[65]

j-dependent image anisotropy parameters were also derived from a crushed S($^1D_2$) image. Due to orbital alignment of the S atom, the $\beta^{VV}{}_2$ parameter is not a direct indicator of the **μ**-**v** correlation.[121, 122, 129, 132] However, the $\beta^{VV}{}_2$ values derived from the S($^1D_2$) image show a general trend from near 0 at low *j* to near 1 at high *j* which is consistent with our derived $\beta_0^2(20)$ values from the CO images.

The inner ring of the CO image on the left in Figure 5.9 corresponds to v=1, *j*=60 CO products. This inner ring shows more significant four-fold symmetry than the outer ring (lower *j*). Anisotropic inner rings are observed in several other CO S branch and R branch images. The vector correlations of vibrationally excited CO photofragment will be an interesting future project.

Although the measured bipolar moments can be affected by depolarization due to initial parent rotation, no attempt was made to correct the values to account for depolarization. We anticipate that following supersonic expansion, the OCS parent has low rotational temperature.

CHAPTER VI

CONCLUSIONS AND FUTURE WORK*

In this dissertation, a new method for analyzing sliced or reconstructed non-sliced velocity map ion images detected with 2+1 REMPI, as an extension to the previously published 1+1 REMPI Equations by Grubb *et al*.[82, 83], was presented. These equations can be used to extract vector correlations arising from photodissociation reactions from the anisotropy of experimental ion images. We have shown that the 2+1 REMPI Equations can either be used to numerically solve for bipolar moments in some special systems using direct inversion or to generate simulated angular distributions by forward convolution. The forward convolution simulation can either be used to fit the experimental results manually, or with Monte Carlo sampling. This method utilizes images from three laser polarization geometries (VV, VH, HV) or two VV single geometry from two different REMPI branches (S/O and R/P). Experimental 2+1 REMPI images from OCS and NO_2 photodissociation analyzed with our method resulted in bipolar moments consistent with previous experiments and theoretical calculations. We also demonstrated that the 2+1 Equations can be applied in Q-branch 2+1 REMPI with specific detection sensitivity factors s_k. Lastly, we simulated a hypothetical case with no spatial anisotropy and with ***v-j*** correlations. In this case, we demonstrated that although in certain conditions it is acceptable to apply the 1+1 REMPI Equations to images detected with 2+1 REMPI, such application cannot be universally applied.

---

* Part of this chapter is reprinted from “W. Wei, C. J. Wallace, G. C. McBane and S. W. North, The Journal of Chemical Physics 145 (2), 024310 (2016) ”, with the permission of AIP Publishing.

Simulated data was also used to evaluate the sensitivity of the forward convolution simulations on the bipolar moments. We find that the analysis is sensitive to subset of bipolar moments: some bipolar moments $\beta_0^2(20)$, $\beta_0^0(22)$ and $\beta_0^2(64)$ are more sensitive than the others. The $\beta_0^2(02)$ moment is much less sensitive to experimental measurements. The distributions of all of the bipolar moment values become narrower when simultaneous fits to more experimental angular distributions are performed, as the system's degrees of freedom decreased. Thus the approach of using linear combinations of limiting cases to constrain the fitting was a more stable method for the forward convolution simulations.

Velocity map ion imaging experiments are utilized to study OCS photodissociation in the 214 nm region. Product distributions were measured by probing both CO and S($^1D_2$) fragments. One color laser photodissociation and 2+1 REMPI probing the E-X transition were conducted to obtain a rotational distribution of CO products for both v=0 and v=1. Two color S($^1D_2$) images show a rovibrational product distribution consistent with the one from the CO REMPI. The rotational distributions for both v=0 and v=1 CO show two components that are shifted toward higher *j* compared to longer dissociation wavelengths and nearly coalesced. The v=1 CO rotational distribution generally has the same shape, but is shifted to lower *j* by 2-3 quanta.

Dr. George McBane conducted classical trajectory calculations including surface hopping, which reproduce the measured CO rotational distributions and their dependence on wavelength well, though the v=1 population is underestimated. The calculations indicate that the highest *j* peak in the rotational distribution arises from molecules that begin on the 2^1A' state but make non-adiabatic transitions to the 1^1A' (X) ground state and consequently avoid the rotational deceleration caused by the inner

wall of the bending potential of A-state OCS. The medium-high *j* peak arises from dissociation on the 2^1A' state. The lower *j* peak arises from incoherent excitation to 2^1A' or the 1^1A" states followed by direct photodissociation on those surfaces, as found in previous work.

As an application of the newly developed method, vector correlation information in the form of bipolar moments was extracted from signal images using a new procedure suitable for 2+1 REMPI measurements in a single polarization geometry on multiple spectral branches. The resulting moments, in particular the rotational alignment of product CO, are consistent with the scalar property measurements and computational results, which indicate a substantial contribution of 1^1A″ absorption to the lower-*j* part of the rotational distribution.

There are some possible improvements for the application of the new method discussed in this work. The current method of forward convolution simulation involves linear combinations of limiting cases generating bipolar moments. It has been discussed in Chapter III and Chapter IV that $\beta_0^0(44)$ moment generated from limiting cases will not span over the full range of physically meaningful values. The reason for the incompleteness of these five limiting cases is unknown. It is worth investigating whether there are any extra limiting cases which represent the two photon transition process of the 2+1 REMPI detection.

Another issue with the forward convolution simulation approach is that currently it is conducted by either manual adjustment of parameters or with Monte Carlo sampling of the parameters. The Monte Carlo sampling presented here does not include any type of optimization. When sampling for simultaneous fitting of multiple images, it takes a considerable amount to time to obtain a single acceptable fit. Since the parameter

space is large, significant computing time is wasted on parameter combinations far from the optimized ones. Possible improvements can include optimization: each iteration of Monte Carlo sampling only sample some parameters (not all) at a time. The computer then evaluates the fitting after each search, then accepts or rejects the fit based on whether the chi square residual is reduced from the last iteration, instead of a pre-determined chi square residual. Certain established algorithms, like the Nelder–Mead method (Amoeba method) or evolutionary algorithm can be utilized to improve efficiency and avoid overfitting or local minima.

Another potential aspect of improvement is to increase the sensitivity of the image anisotropies to **μ**-***j*** and **v**-***j*** correlations. The anisotropy of an image is the combined result of **μ**-**v**, **μ**-***j*** and **v**-***j*** correlations. In certain cases (like OCS), one is more interested in the **μ**-***j*** correlations instead of resolving all of the vector correlations. In such cases, it is better to be able to reduce the effects of **μ**-**v** correlations and make the experimental observation more sensitive to **μ**-***j*** correlations. Such methods have been developed when using Doppler profile to study vector correlations, like magic angle detection, or adding two perpendicularly and one parallelly detected Doppler profiles together to eliminate the contribution from **μ**-**v** correlations,[34, 64] or adding two R/P branch and one Q branch profile of the same detection geometry to experimentally eliminate influence of v-j correlations in certain conditions.

One issue with the current OCS photodissociation is the vibrational branching ratio of CO fragments. This work reported a v=1 branching ratio of 21% which is significantly higher than previous results. It will be interesting to review the previous observations of vibrationally excited CO at different wavelengths. Does the vibrational excitation product channel open over a narrow range of wavelengths, or is it a gradual

transition? Previously, Rijs *et al*.[117] has reported trace amount of v=1 CO fragments although a branching ratio is not determined. Similar results have been repeated in the North group. Further investigation is needed to determine the vibrational branching ratio at 230 nm.

The origin of vibrationally excited CO fragments is still not clear. The calculations from Dr. McBane indicate that the v=1 CO products go through dynamics similar to v=0 products, i.e. both 2^1A' (A) or the 1^1A" (B) states are involved in formation of low *j* products, while high *j* products arise from molecules from the 2^1A' (A) or the 1^1A' (X) state. As mentioned in Chapter V, the computational rotational distribution for vibrationally excited CO does not match quantitatively well with experimental results. However, an adjusted computational rotational distribution with no 1^1A" (B) state involvement can fit the experimental results much better. This fit is also supported by preliminary experimental measurements of vector correlations of v=1 CO fragments from the North group.[138] Further experimental and theoretical investigation is still needed.

REFERENCES

1. A. S. Bracker, Ph.D. Thesis, University of California, Berkeley, CA, 1997.
2. M. N. R. Ashfold and J. E. Baggott, *Molecular Photodissociation Dynamics*. (Royal Society of Chemistry, Letchworth, UK, 1987).
3. M. N. R. Ashfold, N. H. Nahler, A. J. Orr-Ewing, O. P. J. Vieuxmaire, R. L. Toomes, T. N. Kitsopoulos, I. A. Garcia, D. A. Chestakov, S.-M. Wu and D. H. Parker, Phys. Chem. Chem. Phys. **8** (1), 26 (2006).
4. T. Baer and W. L. Hase, *Unimolecular Reaction Dynamics: Theory and Experiments*. (Oxford University Press, Oxford, UK, 1996).
5. M. N. R. Ashfold, I. R. Lambert, D. H. Mordaunt, G. P. Morley and C. M. Western, J. Phys. Chem. **96** (7), 2938 (1992).
6. L. J. Butler and D. M. Neumark, J. Phys. Chem. **100** (31), 12801 (1996).
7. Y. T. LEE, Science **236** (4803), 793 (1987).
8. A. H. Zewail, Science **242** (4886), 1645 (1988).
9. R. N. Zare and P. J. Dagdigian, Science **185** (4153), 739 (1974).
10. J. L. Kinsey, Annu. Rev. Phys. Chem. **28** (1), 349 (1977).
11. a. M N R Ashfold and J. D. Howe, Annu. Rev. Phys. Chem. **45** (1), 57 (1994).
12. G. A. Vanasse and D. J. Baker, *Spectrometric Techniques*. (Academic Press, Cambridge, MA, 1977).
13. G. E. Busch, R. T. Mahoney, R. I. Morse and K. R. Wilson, J. Chem. Phys. **51** (1), 449 (1969).
14. R. W. Diesen, J. C. Wahr and S. E. Adler, J. Chem. Phys. **50** (8), 3635 (1969).
15. S.W.North, private communication, 2013

16. R. Schmiedl, H. Dugan, W. Meier and K. H. Welge, Zeitschrift für Physik A Atoms and Nuclei **304** (2), 137 (1982).

17. W. C. Wiley and I. H. McLaren, Rev. Sci. Instrum. **26** (12), 1150 (1955).

18. J. J. Czyzewski, T. E. Madey and J. T. Yates, Phys. Rev. Lett. **32** (14), 777 (1974).

19. D. W. Chandler and P. L. Houston, J. Chem. Phys. **87** (2), 1445 (1987).

20. D. J. De Rosier and A. Klug, Nature **217** (5124), 130 (1968).

21. L. A. Shepp and B. F. Logan, IEEE Trans. Nucl. Sci. **21** (3), 21 (1974).

22. K. R. Castleman, *Digital Image Processing*. (Prentice-Hall, Upper Saddle River, NJ, 1979).

23. E. W. Hansen and P.-L. Law, J. Opt. Soc. Am. A **2** (4), 510 (1985).

24. L. Montgomery Smith, D. R. Keefer and S. I. Sudharsanan, J. Quant. Spectrosc. Radiat. Transfer **39** (5), 367 (1988).

25. R. N. Strickland and D. W. Chandler, Appl. Opt. **30** (14), 1811 (1991).

26. G. M. Roberts, J. L. Nixon, J. Lecointre, E. Wrede and J. R. R. Verlet, Rev. Sci. Instrum. **80** (5), 053104 (2009).

27. J. O. F. Thompson, C. Amarasinghe, C. D. Foley and A. G. Suits, J. Chem. Phys. **147** (1), 013913 (2017).

28. A. T. J. B. Eppink and D. H. Parker, Rev. Sci. Instrum. **68** (9), 3477 (1997).

29. B.-Y. Chang, R. C. Hoetzlein, J. A. Mueller, J. D. Geiser and P. L. Houston, Rev. Sci. Instrum. **69** (4), 1665 (1998).

30. R. N. Zare, *Angular Momentum : Understanding Spatial Aspects in Chemistry and Physics*. (Wiley, New York, 1991).

31. R. N. Zare and D. R. Herschbach, Proc. IEEE **51**, 173 (1963).

32. A. T. J. B. Eppink and D. H. Parker, J. Chem. Phys. **109** (12), 4758 (1998).

33. J. Solomon, J. Chem. Phys. **47** (3), 889 (1967).

34. R. N. Dixon, J. Chem. Phys. **85** (4), 1866 (1986).

35. T. P. Rakitzis and R. N. Zare, J. Chem. Phys. **110** (7), 3341 (1999).

36. T. P. Rakitzis and A. J. Alexander, J. Chem. Phys. **132** (22), 224310 (2010).

37. G. E. Hall and P. L. Houston, Annu. Rev. Phys. Chem. **40** (1), 375 (1989).

38. A. J. Orr-Ewing and R. N. Zare, Annu. Rev. Phys. Chem. **45** (1), 315 (1994).

39. R. J. Gordon and G. E. Hall, Adv. Chem. Phys. **96**, 1 (1996).

40. G. E. Hall, N. Sivakumar, D. Chawla, P. L. Houston and I. Burak, J. Chem. Phys. **88** (6), 3682 (1988).

41. K. H. Gericke, S. Klee, F. J. Comes and R. N. Dixon, J. Chem. Phys. **85** (8), 4463 (1986).

42. M. P. Grubb, M. L. Warter, K. M. Johnson and S. W. North, J. Phys. Chem. A **115** (15), 3218 (2011).

43. M. P. Grubb, M. L. Warter and S. W. North, Phys. Chem. Chem. Phys. **14** (19), 6733 (2012).

44. S. W. North and G. E. Hall, J. Chem. Phys. **104** (5), 1864 (1996).

45. S. J. Klippenstein and J. I. Cline, J. Chem. Phys. **103**, 5451 (1995).

46. C. Jonah, J. Chem. Phys. **55** (4), 1915 (1971).

47. S. c. Yang and R. Bersohn, J. Chem. Phys. **61** (11), 4400 (1974).

48. H. Kim, K. S. Dooley, S. W. North, G. E. Hall and P. L. Houston, J. Chem. Phys. **125** (13), 133316 (2006).

49. E. Wrede, E. R. Wouters, M. Beckert, R. N. Dixon and M. N. R. Ashfold, J. Chem. Phys. **116** (14), 6064 (2002).

50. H.-P. Loock, J. Cao and C. X. W. Qian, Chem. Phys. Lett. **206** (5), 422 (1993).

51. A. V. Demyanenko, V. Dribinski, H. Reisler, H. Meyer and C. X. W. Qian, J. Chem. Phys. **111** (16), 7383 (1999).

52. A. V. Demyanenko, A. B. Potter, V. Dribinski and H. Reisler, J. Chem. Phys. **117** (6), 2568 (2002).

53. M. Dubs, U. Bruhlmann and J. R. Huber, J. Chem. Phys. **84**, 3106 (1986).

54. G. E. Hall, N. Sivakumar, P. L. Houston and I. Burak, Phys. Rev. Lett. **56**, 1671 (1986).

55. S. W. North, J. Mueller and G. E. Hall, Chem. Phys. Lett. **276**, 103 (1997).

56. R. Uberna and J. I. Cline, J. Chem. Phys. **102**, 4705 (1995).

57. R. O. Loo, C. E. Strauss, H. P. Haerri, G. E. Hall, P. L. Houston, I. Burak and J. W. Hepburn, J. Chem. Soc., Faraday Trans. **85**, 1185 (1989).

58. S. K. Lee, D. Townsend, O. S. Vasyutinskii and A. G. Suits, Phys. Chem. Chem. Phys. **7**, 1650 (2005).

59. A. S. Bracker, E. R. Wouters, A. G. Suits and O. S. Vasyutinskii, J. Chem. Phys. **110**, 6749 (1999).

60. T. P. Rakitzis, Chem. Phys. Lett. **342** (1–2), 121 (2001).

61. L. D. A. Siebbeles, M. Glassmaujean, O. S. Vasyutinskii, J. A. Beswick and O. Roncero, J. Chem. Phys. **100**, 3610 (1994).

62. M. L. Costen, S. W. North and G. E. Hall, J. Chem. Phys. **111**, 6735 (1999).

63. M. L. Costen and G. E. Hall, Phys. Chem. Chem. Phys. **9** (2), 272 (2007).

64. M. P. Docker, Chem. Phys. **135** (3), 405 (1989).

65. W. Wei, C. J. Wallace, G. C. McBane and S. W. North, J. Chem. Phys. **145** (2), 024310 (2016).

66. O. Tokal, Ph.D. Thesis, Cornell University, Cornell, NY, 2011.

67. M. A. Hines, H. A. Michelsen and R. N. Zare, J. Chem. Phys. **93**, 8557 (1990).

68. M. A. Hines, Ph.D. Thesis, Stanford University, Stanford, CA, 1992.

69. G. Black and L. E. Jusinski, J. Chem. Phys. **82**, 789 (1985).

70. J. Steadman and T. Baer, J. Chem. Phys. **89**, 5507 (1988).

71. Y. Pak and R. C. Woods, J. Chem. Phys. **107** (13), 5094 (1997).

72. J. H. Moore, C. C. Davis, M. A. Coplan and S. C. Greer, *Building Scientific Apparatus*. (Cambridge University Press, Cambridge, UK, 2009).

73. D. Townsend, M. P. Minitti and A. G. Suits, Rev. Sci. Instrum. **74**, 2530 (2003).

74. H. Kim, Ph.D. Thesis, Texas A&M University, College Station, TX, 2006.

75. M. P. Grubb, Ph. D. Thesis, Texas A&M University, College Station, TX, 2012.

76. M. P. Grubb, private communication. (2014)

77. R. G. Bray and R. M. Hochstrasser, Mol. Phys. **31** (4), 1199 (1976).

78. P. W. Atkins, J. De Paula and V. Walters, *Physical Chemistry*. (Macmillan Higher Education, London, UK, 2006).

79. National Institutes of Health, (https://imagej.nih.gov/ij/, 2017).

80. A. V. Komissarov, M. P. Minitti, A. G. Suits and G. E. Hall, J. Chem. Phys. **124**, 014303 (2006).

81. R. N. Zare, Ph.D. Thesis, Harvard University, Cambridge, MA, 1964.

82. M. P. Grubb, M. L. Warter, C. D. Freeman, N. A. West, K. M. Usakoski, K. M. Johnson, J. A. Bartz and S. W. North, J. Chem. Phys. **135** (9), 094201 (2011).

83. M. P. Grubb, M. L. Warter, C. D. Freeman, N. A. West, K. M. Usakoski, K. M. Johnson, J. A. Bartz and S. W. North, J. Chem. Phys. **136** (21), 219901 (2012).

84. M. Thompson, (http://www.genplot.com/, 2017).

85. M. G. Gonzalez, J. D. Rodriguez, L. Rubio-Lago and L. Bañares Phys. Chem. Chem. Phys. **16** (47), 26330 (2014).

86. S. Marggi Poullain, M. G. Gonzalez, P. C. Samartzis, T. N. Kitsopoulos, L. Rubio-Lago and L. Bañares, Phys. Chem. Chem. Phys. **17** (44), 29958 (2015).

87. J. D. Rodriguez, M. G. Gonzalez, L. Rubio-Lago, L. Banares, P. C. Samartzis and T. N. Kitsopoulos, J. Phys. Chem. A **117** (34), 8175 (2013).

88. Y. Mo, H. Katayanagi and T. Suzuki, J. Chem. Phys. **110** (4), 2029 (1999).

89. Y. Mo and T. Suzuki, J. Chem. Phys. **109** (11), 4691 (1998).

90. T. P. Rakitzis, G. E. Hall, M. L. Costen and R. N. Zare, J. Chem. Phys. **111** (19), 8751 (1999).

91. W. Denzer, S. J. Horrocks, P. J. Pearson and G. A. D. Ritchie, Phys. Chem. Chem. Phys. **8** (16), 1954 (2006).

92. G. E. Hall and M. Wu, J. Phys. Chem. **97** (42), 10911 (1993).

93. G. E. Hall, private communication, 2017.

94. W. Wei, C. J. Wallace, M. P. Grubb and S. W. North, J. Chem. Phys. **147** (1), 013947 (2017).

95. A. J. van den Brom, T. P. Rakitzis, J. van Heyst, T. N. Kitsopoulos, S. R. Jezowski and M. H. M. Janssen, J. Chem. Phys. **117** (9), 4255 (2002).

96. G. C. McBane, J. A. Schmidt, M. S. Johnson and R. Schinke, J. Chem. Phys. **138** (9), 094314 (2013).

97. Y. Sato, Y. Matsumi, M. Kawasaki, K. Tsukiyama and R. Bersohn, J. Phys. Chem. **99**, 16307 (1995).

98. The ranges of error for reported bipolar moments are estimated by varying each of the individual bipolar moment value until the corresponding simulation noticeably deviated from the set of experimental angular distributions.

99. The raw VH geometry image data of Suzuki and coworkers exhibited strong up-down asymmetry, and the angular distribution of the lower half of image show particularly strong anisotropy beyond second order Legendre polynomial, which is not physically reasonable. We re-symmetrized this image by discarding the lower half of image prior to four-fold symmetrization.

100. A. G. Suits, R. L. Miller, L. S. Bontuyan and P. L. Houston, J. Chem. Soc., Faraday Trans. **89** (10), 1443 (1993).

101. P. J. Crutzen, Geophys. Res. Lett. **3** (2), 73 (1976).

102. J. Notholt, Z. Kuang, C. P. Rinsland, G. C. Toon, M. Rex, N. Jones, T. Albrecht, H. Deckelmann, J. Krieg, C. Weinzierl, H. Bingemer, R. Weller and O. Schrems, Science **300** (5617), 307 (2003).

103. M. Chin and D. D. Davis, J. Geophys. Res. Atmos. **100** (D5), 8993 (1995).

104. M. O. Andreae and P. J. Crutzen, Science **276**, 1052 (1997).

105. G. Krysztofiak, Y. V. Té, V. Catoire, G. Berthet, G. C. Toon, F. Jégou, P. Jeseck and C. Robert, Atmosphere-Ocean **53** (1), 89 (2015).

106. S. Hattori, S. O. Danielache, M. S. Johnson, J. A. Schmidt, H. G. Kjaergaard, S. Toyoda, Y. Ueno and N. Yoshida, Atmospheric Chemistry and Physics **11** (19), 10293 (2011).

107. L. T. Molina, J. J. Lamb and M. J. Molina, Geophys. Res. Lett. **8** (9), 1008 (1981).

108. C. Y. Robert Wu, F. Z. Chen and D. L. Judge, J. Quant. Spectrosc. Radiat. Transfer **61** (2), 265 (1999).

109. S. O. Danielache, S. Nanbu, C. Eskebjerg, M. S. Johnson and N. Yoshida, J. Chem. Phys. **131** (2), 024307 (2009).

110. K. Sunanda, B. N. Rajasekhar, P. Saraswathy and B. N. Jagatap, J. Quant. Spectrosc. Radiat. Transfer **113**, 58 (2012).

111. J. A. Schmidt, M. S. Johnson, G. C. McBane and R. Schinke, J. Chem. Phys. **137** (5), 054313 (2012).

112. X. Bai, H. Liang, Z. Zhou, Z. Hua, B. Jiang, D. Zhao and Y. Chen, J. Chem. Phys. **147** (1), 013930 (2017).

113. S. P. Sander, J. Abbatt, J. R. Barker, J. B. Burkholder, R. R. Friedl, D. M. Golden, R. E. Huie, C. E. Kolb, M. J. Kurylo, G. K. Moortgat, V. L. Orkin and P. H. Wine, JPL Publication 10-6, **Evaluation Number 17,**, 684 (2011).

114. G. Nan, I. Burak and P. L. Houston, Chem. Phys. Lett. **209**, 383 (1993).

115. N. Sivakumar, G. E. Hall, P. L. Houston, J. W. Hepburn and I. Burak, J. Chem. Phys. **88**, 3692 (1988).

116. Y. Sato, Y. Matsumi, M. Kawasaki, K. Tsukiyama and R. Bersohn, J. Phys. Chem. **99** (44), 16307 (1995).

117. A. M. Rijs, E. H. G. Backus, C. A. d. Lange, M. H. M. Janssen, N. P. C. Westwood, K. Wang and V. McKoy, J. Chem. Phys. **116** (7), 2776 (2002).

118. S. K. Lee, R. Silva, S. Thamanna, O. S. Vasyutinskii and A. G. Suits, J. Chem. Phys. **125** (14), 144318 (2006).

119. T. Suzuki, H. Katayanagi, S. Nanbu and M. Aoyagi, J. Chem. Phys. **109**, 5778 (1998).

120. M. H. Kim, W. Li, S. K. Lee and A. G. Suits, Can. J. Chem. **82**, 880 (2004).

121. Y. Mo, H. Katayanagi, M. C. Heaven and T. Suzuki, Phys. Rev. Lett. **77**, 830 (1996).

122. T. P. Rakitzis, P. C. Samartzis and T. N. Kitsopoulos, Phys. Rev. Lett. **87**, 123001 (2001).

123. A. J. van den Brom, T. P. Rakitzis and M. H. M. Janssen, J. Chem. Phys. **121**, 11645 (2004).

124. J. Baker, J. L. Lemaire, S. Couris, A. Vient, D. Malmasson and F. A. Rostas, Chem. Phys. **178**, 569 (1993).

125. E. K. Plyler, L. R. Blaine and W. S. Connor, J. Opt. Soc. Am. **45**, 102 (1955).

126. G. Lucchese, R. R. Lucchese and S. W. North, J. Chem. Educ. **87**, 345 (2010).

127. A. Sugita, M. Mashino, M. Kawasaki, Y. Matsumi, R. Bersohn, G. Trott-Kriegeskorte and K.-H. Gericke, J. Chem. Phys. **112**, 7095 (2000).

128. H. Katayanagi and T. Suzuki, Chem. Phys. Lett. **360**, 104 (2002).

129. L. M. Lipciuc, T. P. Rakitzis, L. W. Meerts, G. C. Groenenboom and M. H. M. Janssen, Phys. Chem. Chem. Phys. **13**, 8549 (2011).

130. C. J. Wallace and C. E. Gunthardt, private communication. (2017)

131. M. Eidelsberg, J. Y. Roncin, A. Le Floch, F. Launay, C. Letzelter and J. Rostas, J. Mol. Spectrosc. **121**, 309 (1987).

132. M. Brouard, A. V. Green, F. Quadrini and C. Vallance, J. Chem. Phys. **127**, 084304 (2007).

133. G. C. McBane and R. Schinke, J. Chem. Phys. **136**, 044314 (2012).

134. J. A. Schmidt and J. M. H. Olsen, J. Chem. Phys. **141**, 184310 (2014).

135. J. A. Schmidt, private communication (2015)

136. J. C. Tully, J. Chem. Phys. **93**, 1061 (1990).

137. R. Schinke and G. C. McBane, J. Chem. Phys. **132**, 044305 (2010).

138. C. J. Wallace and C. E. Gunthardt, private communication. (2017)